UNIVERSITÀ DEGLI STUDI
DI MODENA E REGGIO EMILIA

Dottorato di ricerca in Physics and Nanosciences

Ciclo XXXV

H_2 interaction with copper modified CeO_2 ultrathin films

Candidate: Avinash Vikatakavi

Relatore (Tutor): Dr Paola Luches

Correlatore (Co-Tutor): Dr. Stefania Benedetti

Secondo Correlatore (Co-Tutor): Prof. Sergio D'Addato

Coordinatore del Corso di Dottorato: Prof. Marco Affronte

Index

Abstract

Introduction

Acknowledgements

Chapter 1 State of the art 1

1.1 PEMFCs 2

1.2 Electrocatalysts 3

1.2.1 Metal oxide-based materials 4

1.3 Ceria and ceria-based materials 7

1.3.1 Doping effect on oxygen vacancy formation and reduction properties 9

1.3.2 Ceria as support material for metals (Cu, Ag and Au) 13

1.3.3 Interaction between ceria-based materials and H_2 18

1.4 Bibliography 24

Chapter 2 Experimental apparatus and investigation techniques 30

2.1 SESAMo laboratory 30

2.1.1 Sample growth and treatments 32

2.2 X-ray Photoelectron spectroscopy 32

2.3 Scanning tunneling microscopy 36

2.4 NEXAFS 38

2.4.1 X-ray absorption spectroscopy 38

2.4.2 NFFA APE-HE experimental beamline facility, Trieste 40

2.4.3 Reaction cell 41

2.5 Bibliography 46

Chapter 3 Surface modifications induced by H_2 in Cu-modified CeO_2 48

3.1 Sample preparation and reduction treatments 48

3.2 XPS Ce 3d spectra data analysis 49

3.3 O 1s XPS spectra data analysis 51

3.4 Surface morphology 55

3.5 Theoretical calculations 56

3.5.1 Reduction during thermal steps in UHV 57

3.5.2 Reduction during thermal steps in H_2 57

3.5.3 Discussion 57

3.6 Bibliography 61

Chapter 4 Dopant stability and modifications in Cu:CeO_2 at increasing dopant concentration 62

4.1 Films with different doping concentration 62

4.1.1 Cu doping stability 63

4.1.2 Evolution of Ce^{3+} concentration 67

4.1.3 OH surface adsorption 69

4.1.4 Surface morphology 71

4.2 Buffer layer sample 72

4.2.1 Cu doping stability 72

4.2.2 Evolution of Ce^{3+} concentration 73

4.2.3 OH surface adsorption 74

4.2.4 Surface morphology 76

4.3 Dilution of Cu deposited on CeO_2 film 77

4.4 Bibliography 83

Chapter 5 Cu nanoparticles on CeO_2: effect of hydrogen on the stability 84

5.1 Cu NPs on CeO_2 and UHV cycle 85

5.2 H_2 cycle 89

5.3 Quantitative analysis 92

5.3.1 Evolution of Ce^{3+} on the surface 92

5.3.2 OH adsorption on the surface 93

5.4 Bibliography 95

Chapter 6 Ambient pressure NEXAFS on Cu:CeO_2/ MgO 96

6.1 XPS study of Cu:CeO_2/ MgO films 96

6.1.1 Evolution of Ce^{3+} ion concentration 96

6.1.2 Modifications to the O 1s spectra 99

6.1.3 Cu dopant stability 99

6.2 Ambient pressure NEXAFS study on Cu:CeO_2/ MgO films 101

6.2.1 Ce^{3+} ion concentration evolution 102

6.2.2 Evolution of Cu oxidation states 107

6.2.3 Ambient pressure NEXAFS of 6% Fe:CeO_2 111

6.3 Gas chromatography 112

6.4 Bibliography 114

Conclusions 115

Appendix A 117

Appendix B 119

ABSTRACT

Proton exchange membrane fuel cells (PEMFCs) have been attractive for applications in transportation, stationary and portable devices owing to their high-power density, high efficiency, ease of operation and low/zero emissions. Despite their salient features, PEMFCs large commercialization is impeded due to the utilization of expensive and scarce platinum based electrocatalysts. Many non-noble materials are explored so far to replace Pt or Pt-based and obtain similar or better catalytic activity. Among them Cerium oxide (CeO_2), a reducible oxide has been considered as the promising candidate as electrode material for PEM fuel cells because of their redox properties and as well as the ability to dissociate H_2 molecules in the absence of noble metals. In addition, modification of CeO_2 with aliovalent cationic species, has been identified as a promising method to reduce activation barrier for H_2 adsorption dissociation on the surface the CeO_2.

Herein, we investigate the modifications induced in the Cu-modified CeO_2 epitaxial ultrathin film (model system) properties during the interaction with H_2. Cu-modified CeO_2 ultrathin films are grown by reactive molecular beam epitaxy source in O_2 partial pressure ($1*10^{-7}$ mbar). We have doped CeO_2 with 6%, 27% of Cu atoms nominally and studied their chemical and morphological properties during thermal reduction cycles in UHV ($1*10^{-9}$ mbar) and H_2 ($1*10^{-7}$ mbar) using in-situ x-ray photoelectron spectroscopy (XPS) and Scanning tunneling microscopy (STM) respectively. XPS spectra of the Cu-modified films is acquired after each thermal cycle in both reducing atmospheres (UHV and H_2) after cooling down the sample to RT. XPS spectra provided the quantitative information on the reducibility of Ce ions (Ce^{4+} to Ce^{3+}), O-vacancy, OH-group formation on the surface of these films during the interaction with H_2. Density functional calculations (DFT) in collaboration with Rita Magri and group have been performed to gain deeper insights on the reducibility and the H_2 dissociation on Cu-modified surfaces. Both experimental and DFT calculations helped us to deduce the role of the Cu atoms on the H_2 dissociation mechanism of the Cu-modified CeO2 ultrathin films. Also, Cu NPs supported on CeO_2 ultrathin films are studied under same conditions. Along with the reducibility of ceria, the stability of Cu NPs on these surfaces are investigated using STM at RT.

The experimental results indicate that the Cu atoms as dopant and NPs supported on the surface of CeO_2 tend increase the reducibility of Ce atoms as the electrons released during the O-vacancy formation and H_2 dissociation mechanism are acquired mostly by Ce ions. The increase in the weight of the OH group during thermal treatments in H_2 can be ascribed to the lower H_2 dissociation barrier for the Cu-modified surfaces than pure ceria. But the DFT calculations showed that the energy barrier for H_2 dissociation on the Cu-modified CeO_{2-x} is 0.8 eV, which is only slightly lower than the pure CeO_2 (111) stable surface. However,

Cu atoms are also reduced from +2 to +1 the along with Ce atoms during the dissociative adsorption of H_2 process on the surface, which are very reactive. These Cu^{+1} further decreases the H_2 dissociation barrier significantly to about 0.33 eV. Our experimental results coupled with DFT calculations suggest that the Cu atoms play a vital role in the decrease of the H_2 barrier for ceria films. STM characterization of these films are performed at RT, the surface morphology of the films has not been altered significantly after the H_2 thermal reduction cycles. We performed in-operando NEXAFS studies on the Cu doped films at APE-HE beamline, Trieste in collaboration with Dr. Piero Torelli, to study the evolution of the oxidation state of the Ce and Cu during thermal treatments in H_2. We have investigated the evolution of the Ce and Cu oxidation state during the thermal treatments in H_2 at ambient pressure. We observed a trend in the evolution of Ce and Cu atoms, and it confirmed the influence of the reduction of Cu atoms (from +2 to +1) on the reduction of Ce as well as H_2 dissociation on the surface. The results are further supported by the gas chromatography measurements.

We strongly believe that our experimental results supported by the DFT calculations provides a deeper comprehension on the H_2 dissociation mechanism on the Cu-modified ceria. Even though the studied system is a model system (which is investigated under UHV conditions), the result obtained are quite interesting and are in agreement with the theoretical calculations. So, this study can serve as a model system to prepare the real catalysts for the PEMFCs.

Introduction

A major part of the current energy demand is met by energy generated from fossil fuel-based sources, reaching up to almost 80%. The massive utilization of fossil fuels has caused severe environmental problems. Over recent decades, a great effort has been dedicated to exploit sustainable and green renewable energy sources to decrease the reliance on fossil fuels. Among the different renewable energy sources, hydrogen (H_2) is considered among the most promising ones. Hydrogen can be used as a fuel in electrochemical devices such as fuel cells to produce electricity. Fuel cells directly convert the chemical energy into electric energy without any combustion. Fuel cells therefore represent an attractive and practical solution to produce green energy from hydrogen. Proton exchange membrane fuel cells (PEMFCs) are considered as promising power sources because of their characteristic features such as low operational temperature, zero or low emission of CO_2, ease of operation and low noise, unlike batteries.

Despite their attractive properties, which make them ideal for practical power sources in portable and stationary applications [1], PEMFCs large scale commercialization is hindered by the use of expensive platinum as the catalyst for both anode and cathode [2,3]. There has been a significant surge in finding a suitable catalyst material with good electrochemical properties, mechanical and thermal stability, and affordable to replace Pt as catalyst for the anode. A variety of strategies have been implemented to realize materials with desired functionalities and low platinum loading for the applications in PEMFCs [4].

Among many materials explored for fuel cell applications, metal-oxide systems have offered superior functionalities over others thanks to the tunable physical, chemical and electronic properties. A wide range of properties such as the presence of hydroxyl groups on the surface, good electrochemical and thermal stability in harsh conditions (acidic, oxidative) have made them particularly attractive candidates for fuel cell applications [5]. However, the low electronic conductivity has been a major drawback for their applications as electrocatalysts. Many novel synthesis approaches have allowed to prepare metal-oxide systems with well controlled size, shape and morphology, and optimized electrochemical properties. Doping the metal-oxide with suitable cationic species can significantly alter the electronic properties [6,7] and increase electronic conductivity. In addition, the defect sites created by the dopant increase the density of active sites for the adsorption and desorption of the reactant species on the surface of the catalyst. Also, specific support materials, such as CNTs [8,9], have been used to enhance the electronic conductivity of the oxides. Many oxide systems are studied for both hydrogen oxidation reaction (HOR) and oxygen reduction reaction (ORR) in fuel cells, especially, TiO_2 [10], CuO_x [11], Fe_3O_4 [12], CeO_2 [13,14], MnO_x [15] etc., but CeO_2 (cerium oxide/ceria) has been in limelight due to its peculiar redox properties. Moreover, the ability of CeO_2 to dissociate H_2 without noble metals has prompted many investigations. Pt-CeO_2

[16,17] has been one of the best examples of an oxide-based system which has showed better catalytic activity with lower platinum loading as compared to traditional Pt-based catalysts.

Metal supported cerium oxide thin film systems such as CeO_2/Cu [18] and CeO_2/Pt [19,20] are intensively investigated by many research groups and studied in their properties for applications as catalysts for water gas shift reaction, fuel cells etc. CeO_2, being a reducible oxide with high oxygen storage capacity, has been used as a catalyst in many heterogenous catalysis applications. Along with the high oxygen storage capacity, the ability of cerium oxide to split hydrogen molecules in the absence of noble metals is very interesting. It is indeed found that cerium doped with aliovalent cationic species decreases the activation barrier for H_2 dissociation on the CeO_2 surface. Many research studies showed that the substitutional doping of CeO_2 with metals like Ag [19] and Cu [20] decreases the oxygen vacancy formation energy and thus increases the reducibility of the material. However, also the dopants typically change their oxidation state during redox processes. Recently, Ag-modified CeO_2 [19] ultrathin films have exhibited higher H_2 dissociation efficiency, compared to pristine CeO_2. But the concentration of reduced Ce ions was lower than on pristine CeO_2 in the same conditions, as most of the electrons were acquired by the Ag atoms during the oxygen vacancy formation and H_2 dissociative adsorption processes. Therefore, a deep understanding on the evolution of the Ce and dopant ions oxidation states during the interaction with H_2 are crucial to design a better catalyst.

In this work, I investigated the interaction between Cu-modified CeO_2 and hydrogen. The films were grown in the form of well-controlled model systems by molecular beam epitaxy on single crystal substrates, Pt(111) and MgO(001), and investigated in chemical and electronic properties and surface morphology during thermal treatments in UHV and in H_2. In-situ X-ray photoelectron spectroscopy was employed to study the evolution of the Ce^{3+} concentration, oxygen vacancy formation and H_2 dissociation processes on the surface during thermal treatments. Scanning tunneling microscopy was used for morphological studies of the surface. Along with CeO_2 modified with different Cu dopant concentration, Cu NPs supported on CeO_2/Pt (111) were also investigated for reactivity towards the H_2 dissociation process. A brief discussion on the interaction between Cu-modified CeO_2 ultrathin films grown on MgO (001) and H_2 is presented and compared with the case of the same films supported on Pt (111). Finally, a deep discussion of the near-edge X-ray absorption fine structure (NEXAFS) studies carried out at APE-HE beamline, ELETTRA (Trieste) on Cu-and Fe-modified CeO_2/MgO are reported. This study focused mainly on the understanding of the correlation between the evolution of the Ce and dopant (Cu and Fe) oxidation states during thermal treatments at ambient pressure in H_2.

This thesis is divided into six chapters as follows:

Chapter 1. Overview of the state of the art of the PEMFCs and brief discussion of the applications of cerium oxide-based materials in fuel cells.

Chapter 2. Experimental details of the growth methods employed, and general description of the characterization techniques applied.

Chapter 3. Detailed discussion of a 6% Cu-doped CeO_2/Pt (111) film and of its reactivity towards H_2 dissociation.

Chapter 4. Comparison of a 6% and a 27% Cu-doped CeO_2/ Pt (111) films in terms of interaction with H_2 and stability of the dopant.

Chapter 5. Detailed description of Cu NPs/CeO_2 system, interaction with H_2 and effect of the temperature on the stability of the nanoparticles.

Chapter 6. Discussion of NEXAFS spectroscopic studies performed on the Cu-and Fe-modified CeO_2 films on MgO. Evolution of Ce^{3+}, Cu^{1+} and Cu^{2+} concentration during thermal treatments at ambient pressure in H_2.

Bibliography:

1. Wilberforce, T., Alaswad, A., Palumbo, A., Dassisti, M., & Olabi, A. G. (2016). Advances in stationary and portable fuel cell applications. *International journal of hydrogen energy*, *41*(37), 16509-16522.
2. H. Tian, L. Zeng, Y. Huang, Z. Ma, G. Meng, L. Peng, C. Chen, X. Cui, J. Shi, In Situ Electrochemical Mn(III)/Mn(IV) Generation of Mn(II)O Electrocatalysts for HighPerformance Oxygen Reduction, Nano-Micro Lett. 12 (2020).
3. Sharma, P., & Pandey, O. P. (2022). Proton exchange membrane fuel cells: fundamentals, advanced technologies, and practical applications. In *PEM Fuel Cells* (pp. 1-24). Elsevier.
4. Brouzgou, A., Song, S. Q., & Tsiakaras, P. (2012). Low and non-platinum electrocatalysts for PEMFCs: Current status, challenges and prospects. *Applied Catalysis B: Environmental*, *127*, 371-388.
5. Zhang, Z., Liu, J., Gu, J., Su, L., & Cheng, L. (2014). An overview of metal oxide materials as electrocatalysts and supports for polymer electrolyte fuel cells. *Energy & Environmental Science*, *7*(8), 2535-2558.
6. Various synthesis methods of aliovalent-doped ceria and their electrical properties for intermediate temperature solid oxide electrolytes
7. Sandhya, K., Chitra Priya, N. S., Rajendran, D. N., & Thappily, P. (2020). Structural and electrical properties of cerium oxides doped by Sb3+ and Bi3+ cations. *Journal of Electronic Materials*, *49*(8), 4936-4944.
8. Riaz, S., Aman, Y., Nasir, M., Hayat, A., & Nawaz, M. H. (2022). Electrical conductivity of metal oxide–carbon composites. In *Metal Oxide-Carbon Hybrid Materials* (pp. 61-74). Elsevier.
9. Andersen, N. I., Serov, A., & Atanassov, P. (2015). Metal oxides/CNT nano-composite catalysts for oxygen reduction/oxygen evolution in alkaline media. *Applied Catalysis B: Environmental*, *163*, 623-627.
10. Gustavsson, M., Ekström, H., Hanarp, P., Eurenius, L., Lindbergh, G., Olsson, E., & Kasemo, B. (2007). Thin film Pt/TiO2 catalysts for the polymer electrolyte fuel cell. *Journal of Power Sources*, *163*(2), 671-678.
11. Wang, X., & Rodriguez, J. A. (2006). *H2 PRODUCTION AND FUEL CELLS* (No. BNL-76860-2006-BC). Brookhaven National Lab.(BNL), Upton, NY (United States).
12. He, X., Long, X., Wang, P., Wu, H., Han, P., Tang, Y., ... & Zhang, Y. (2021). Interconnected 3D Fe3O4/rGO as highly durable electrocatalyst for oxygen reduction reaction. *Journal of Alloys and Compounds*, *855*, 157422.
13. Miller, H. A., Bellini, M., Dekel, D. R., & Vizza, F. (2022). Recent developments in Pd-CeO2 nano-composite electrocatalysts for anodic reactions in anion exchange membrane fuel cells. *Electrochemistry Communications*, *135*, 107219.
14. Pagliaro, M. V., Bellini, M., Bartoli, F., Filippi, J., Marchionni, A., Castello, C., ... & Vizza, F. (2022). Probing the effect of metal-CeO2 interactions in carbon supported electrocatalysts on alkaline hydrogen oxidation and evolution reactions. *Inorganica Chimica Acta*, *543*, 121161.
15. Cruz-Reyes, I., Trujillo-Navarrete, B., García-Tapia, K., Salazar-Gastélum, M. I., Paraguay-Delgado, F., & Félix-Navarro, R. M. (2020). Pd/MnO2 as a bifunctional electrocatalyst for potential application in alkaline fuel cells. *Fuel*, *279*, 118470.
16. Xu, F., Wang, D., Sa, B., Yu, Y., & Mu, S. (2017). One-pot synthesis of Pt/CeO2/C catalyst for improving the ORR activity and durability of PEMFC. *International Journal of Hydrogen Energy*, *42*(18), 13011-13019.

17. Mahata, A., Nair, A. S., & Pathak, B. (2019). Recent advancements in Pt-nanostructure-based electrocatalysts for the oxygen reduction reaction. *Catalysis Science & Technology*, *9*(18), 4835-4863.
18. Yan, H., Yang, C., Shao, W. P., Cai, L. H., Wang, W. W., Jin, Z., & Jia, C. J. (2019). Construction of stabilized bulk-nano interfaces for highly promoted inverse CeO2/Cu catalyst. *Nature communications*, *10*(1), 1-10.
19. Benedetti, S., Righi, G., Luches, P., D'Addato, S., Magri, R., & Selloni, A. (2020). Surface reactivity of Ag-modified ceria to hydrogen: a combined experimental and theoretical investigation. *ACS applied materials & interfaces*, *12*(24), 27682-27690.
20. Vikatakavi, A., Benedetti, S., Righi, G., Magri, R., D'Addato, S., Luches, P., & Selloni, A. (2022). Interaction of Hydrogen with Cu-Modified Cerium Oxide Surfaces. *The Journal of Physical Chemistry C*, *126*(44), 18652-18660.

Acknowledgements

First and foremost, I am extremely grateful to my supervisors, Dr. Paola Luches, Dr. Stefania Benedetti and Prof. Sergio D'Addato for their invaluable and continuous support, advice and encouragement during my PhD. I would like to express my sincere thanks to my supervisors for their kind support during the difficult pandemic period and checking on me regularly. I would also like to extend my sincere thanks to Dr. Paola Luches, Prof. Sergio Valeri and Prof. Sergio D'Addato for helping me with funding opportunities over the last 3 years. I am deeply grateful to Dr. Stefania Benedetti for her patience and treasured support which was helpful in designing my experiments and data analysis. I would like to express my special thanks to Prof. Sergio D'Addato for his continuous support in both professional and personal life starting from my master degree period to today and I hope to continue this cherished relationship. I also extend my thanks to CNR Istituto Nanoscienze, Modena and University of Modena and Reggio Emilia for allowing me to have the opportunity to pursue a PhD and equipping me with best tools of the trade to facilitate the same.

I am thankful to Dr. Giulia Righi, Prof. Rita Magri, Prof. Annabella Seloni for their great theoretical calculations which was pivotal in completion my PhD thesis. Also, I must share my thanks to Dr. Piero Torelli, Ms. Silvia Mauri and Mr. Mario Rivera in helping me to perform NEXAFS experiments and embellishing the underlying knowledge for me. I am thankful also to the SESAMo group, Modena for sharing their valuable time during my PhD.

I am deeply grateful to my parents, Usha K.R and Venu.V for their unconditional love and support in every part of my life. My brother, Balaji. V has been my biggest ally, the backbone to all my accomplishments and I can't thank him enough for his selfless support. I also want to acknowledge my sister Sowjanya. V for her love. She has been kind enough to keep tabs on me each and every day. I will also like thank my sister-in-law, Kiranmayee. V for her kindness and support. Moreover, I want to share my unconditional love and affection with my niece Hasini K.R, and nephews Shreyas. V and Pavan Kumar K.R.

I am really thankful to my friends Martin Truniger, Elisa Holderied and their respective families for their kindness and love they poured on me. I can never forget their financial support that helped me to achieve my goals. I am highly privileged to have great friends around me who have been my support system during my hard times in Italy, thank you Jeffrey Raymond and Dr. Dhawal Choudhary for being such an amazing support. I am also willing to share my special gratitude to my friends Antje, Vanessa.

Thank you

Avinash Vikatakavi

Ah! There is a woman who sacrificed a lot for me to achieve my goals and I am indebted to her for continuous affection and love! It is none other than my mother.

Thank you, Usha Vikatakavi.

I dedicate my PhD thesis to my mother!!

Chapter 1

State of the art

This thesis contains a study of the interaction between Cu-modified CeO_2 surfaces and H_2 , using a model system, namely ultrathin films well-controlled in stoichiometry and morphology, investigated mostly by surface science-based methods in ultra-high vacuum conditions. The reason behind the study is to provide a deeper insight into the metal modified CeO_2 system and on its interaction with H_2. Noble metal modified CeO_2 systems are considered to be a promising anode material for proton exchange membrane fuel cells. Therefore, I will initiate the chapter by describing briefly about fuel cells and electrocatalysts employed for the HOR and ORR reactions and then I will give a literature survey on the effect of doping on reducibility of ceria and on the dissociation of H_2 on these surfaces.

The emerging energy crisis arising due to the depletion of fossil fuels reserves and the increase of the energy needs of the planet have prompted many research activities to find suitable and alternative energy sources to fossil fuels. Especially, renewable energy sources such as hydroelectric power, wind, solar etc. are exploited to produce the clean energy to suffice the energy needs. To achieve a safe and sustainable future, we need to find new and alternative methods to the existing energy generation sources and also modify the existing energy generation and storage technologies. Energy conversion or storage devices such as lithium-ion batteries (LIB), fuel cells (FCs) and supercapacitors (SCs) are promising solutions to reduce the fossil fuels for energy and also to mitigate the environmental pollution. Fuel cells are important energy conversion devices due to their high efficiency, ease of operation, zero emission of CO_2 and, most importantly, the availability of reactants makes them more reliable. The main areas of FCs application are in transportation, stationary and portable power devices [1]. Fuel cells convert the chemical energy of a fuel into electrical power through electrochemical reactions and emit only heat and water as the waste products. Even though their working function is similar to batteries, FCs continue to work as long as the fuels and oxidants are supplied [2]. There are several types of fuel cells available, and they are classified according to the electrolyte and fuel used [3]:

1. Proton Exchange (Polymer Electrolyte) Membrane Fuel Cell (PEMFC)
2. Direct Methanol Fuel Cell (DMFC)
3. Alkaline Fuel Cell (AFC)
4. Molten Carbonate Fuel Cell (MCFC)
5. Phosphoric Acid Fuel Cell (PAFC)
6. Solid Oxide Fuel Cell (SOFC)

Among different forms of fuel cells, polymer electrolyte fuel cells (PEMFC) have been attractive because of their properties such as low-operating temperature, lower ecological impact, and high energy density. Due to their noteworthy features, PEMFCs are considered as next generation power sources for transportation and portable applications [4].

1.1 PEMFCs

Polymer electrolyte membrane fuel cells convert chemical energy of fuel (Hydrogen) to electrical energy through a direct electrochemical reaction at the anode without any combustion. A schematic representation of membrane electrode assembly (MEA) is shown in the figure 1. As shown in the figure, the main component of a PEM fuel cell is the MEA, where a polymer electrolyte (Nafion) is sandwiched between anode and cathode [4], the anode and cathode electrodes comprise of catalyst layer (CL) and a gas diffusion layer (GDL). Polymer electrolyte membrane must conduct protons (hydrogen ions) and resist the flow of the fuel (hydrogen) and oxidant (oxygen) to the other side of the cell and also act as electric insulation [6].

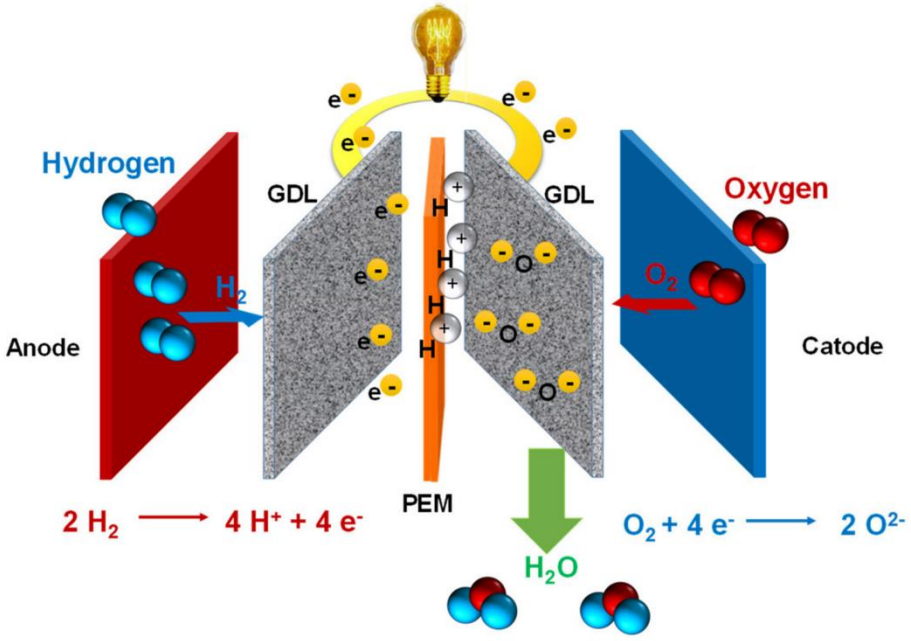

Figure 1: Schematic diagram of a single PEMFC showing anode, cathode, gas diffusion layer (GDL), membrane and electrochemical reactions at anode and cathode [5].

Fuel is delivered to the anode side and oxidant (oxygen from air) is delivered to the cathode through flow field channels. At the anode, hydrogen is dissociated or split into its constituents H^+ and e^-, via the hydrogen oxidation reaction (HOR). Protons travel through the polymer electrolyte membrane to the cathode and electrons travel via an external circuit to the cathode, creating an electrical current. Oxygen reduction

reaction (ORR) takes place at the cathode. Protons and electrons recombine at the cathode together with oxygen and form water as the by-product, which is allowed to flow out of the cell.

The basic electrochemical reactions taking place at anode and cathode simultaneously are given by the following equations:

$$\text{Anode: } H_2 \longrightarrow 2H^+ + 2e^- \quad (1.1)$$

$$\text{Cathode: } \tfrac{1}{2} O_2 + 2e^- + 2H^+ \longrightarrow H_2O \quad (1.2)$$

However, the catalysts employed for HOR and ORR are Pt and Pt-based materials, which are quite expensive and less abundant. Along with the cost of the catalyst, the membrane, and of other components such as flow field design also play a vital role in the overall performance of a fuel cell [7]. Detailed descriptions of the PEM fuel cell and its parts can be found elsewhere [7]. Even though PEM based fuel cells have already found commercial applications such as in automobiles, logistics, portable and stationary power sources [8], the cost and durability are two major limiting factors affecting the widespread commercialization. The two limiting factors are closely related to the Pt and Pt-based electrocatalysts used for both cathode and anode. According to the United States of Energy (DOE) analysis [9], nearly half of the PEMFC cost for large-scale production arises from the use of platinum as the catalyst. For this reason, there is a great need to reduce the usage of precious metals, in particular Pt, as catalysts. Intensive research is focused on designing new catalysts for both HOR and ORR at anode and cathode respectively with low Pt-loading [8]. Many groups have focused on designing Pt-alloy catalysts such as PtCo, PtRu, [10, 11] or non-precious based catalysts such as transition metal oxides [12], nitrides [13], transition metal chalcogenides [14], conductive polymers [15] etc.

1.2 Electrocatalysts

Pt and Pt-based electrocatalysts have been used for both HOR and ORR reactions due to their high catalytic activity, excellent work function and high exchange current density. Usually, nanometer sized Pt particles (NP) are loaded and uniformly spread on the carbon support. But their performance is affected by its low stability as the Pt NPs suffer from dissolution, agglomeration and sintering [16]. Furthermore, Pt catalysts suffer from CO poisoning. Non-precious metal based electrocatalysts with similar or better activity have been in search to replace expensive and scarce Pt- and Pt-based electrocatalysts for both ORR and HOR. Another class of materials that are explored as electrocatalysts and as well as catalyst supports is non-noble metal oxides [17]. Researchers have put a lot of efforts on designing non-noble metal catalysts for ORR cathodic reactions. A lot of progress has been made to increase the performance and durability of the non-noble catalysts [18]. Due to their low-cost and abundancy, transition metal oxides have been widely studied

as they are suitable replacements for precious Pt-based ORR electrocatalysts. Along with the catalyst material, the support material plays an important role in the long-term performance of the PEMFCs. If the interaction between for example metal nanoparticles and the support (usually carbon black) is weak, the metal NPs are released and the performance drops. So, finding the suitable support materials which are stable under the electrochemical reactions in acidic or alkaline conditions is necessary. Carbon nitride has been used as support for noble metal nanocatalysts instead of carbon black to enhance the performance of the cell (durability and corrosion resistance) [19].

1.2.1 Metal oxide-based materials

Non-noble metal oxides have found applications in different fields because they are cheaper, abundant, and environmentally friendly. Their characteristics such as higher corrosion resistance, strong interaction with catalysts or supports and abundant hydroxyl groups on the surface makes them potential candidates for applications in PEMFCs. Hydroxyl groups play an important role in many catalytic reactions by acting as active sites for adsorption of reactants on the surface. Because of their superlative advantages, metal oxides have been employed in PEMFCs as catalysts, co-catalyst and as support both in acidic and alkaline media [17]. Some parameters that need to be met by the metal oxide materials to be employed in PEMFCs [17]:

- High stability: The chosen materials should be compatible with acidic or alkaline media depending on the type of fuel cell and they should not dissolve during operation.
- Resistance to corrosion: They should be stable under electrochemical conditions during the operation.
- Electronic and proton conductivity: Metal oxide should possess enough electrical conductivity. In case of an insulating oxide, doping with metal atoms can increase the conductivity. Metal oxides with good proton conductivity significantly enhance the electrocatalysis of HOR and ORR processes.
- High specific surface area and pertinent porosity: Metal oxides with good or appropriate porosity help in fine dispersion and better utilization of nanoparticles. They also provide a good help in the transfer of liquid fuels and reduce water flooding in the electrodes.
- Compatible with electrode: Bond between metal oxides and noble metal nanoparticles should be good enough to provide a good adhesion and stability

Metal oxides that successfully accomplish the above selection criteria are for example titanium oxides (TiO_x), cobalt oxides (CO_x), copper oxides (CuO_x), manganese oxides (MnO_x),and cerium oxide (CeO_2).

Titanium oxides (TiO_x) have been considered as potential supports for PEMFCs due to their good stability in fuel cell operating conditions, availability, low-cost, non-toxicity and controllable in size and structure.

The strong interaction between titanium oxides and metal nanoparticles is a great advantage for their application in PEMFCs, as this interaction could reduce the agglomeration of metal nanoparticles [20]. Gustavsson et al. reported that the 3 nm TiO_2 film of deposited by thermal evaporation method between Pt and Nafion membrane showed an increased ORR activity where oxygen reduction current density at 0.85 RHE reached to $22*10^{-5}$ A cm^{-2} which is higher than Pt/Nafion was $5.9*10^{-5}$ A cm^{-2} [21]. The increased activity is due to the good dispersion of Pt on TiO_2 and a good proton conductivity through the thin TiO_2 is also observed. Pt/TiO_2 has also showed a better thermal stability and better electrochemical activity than Pt/C [22]. However, in spite of the fact that TiO_2 showed some catalytic activity as support or catalyst, its low electronic conductivity and specific area are limiting its application in fuel cells. Modifying composition and morphology of these oxides can reduce the above-mentioned problems. The electronic conductivity of TiO_2 can be increased by generating oxygen vacancies. These sub-stoichiometric titanium oxides (Magnéli phase) exhibit a single crystal conductivity of 1500 S cm^{-1} which is as higher as graphite [23]. The band gap can be lowered due to the presence of oxygen vacancies and titanium interstitials determining an increase in electronic conductivity. Pt nanocatalysts deposited on Ti_4O_7 support [24] by the impregnation-reduction method employing $Pt(NO)_2(NH_3)_2$ solution as a precursor for Pt have been investigated with Pt loadings less than 10 wt% and the diameter of Pt particles was ranging from 10-20 nm. It was found that Pt/Ti_4O_7 exhibited specific activities similar to Pt/C catalysts for both HOR and ORR. Zhang et al studied Ru@Pt core-shell supported on Ti_4O_7 [25] prepared through pyrolysis followed by microwave irradiation. reported that these catalysts exhibited a higher CO-tolerance compared to PtRu/C alloy catalysts. Electronic conductivity of TiO_2 can be enhanced by doping TiO_2 with metals such as Nb [26], or by Mo-doping prepared using single-step hydrothermal process to support Pt nanocatalysts was for ORR [27]. It was found that electron donation from TiO_2 to Pt takes place due to the strong metal-support interaction (SMSI). One more method to improve the conductivity of TiO_2 and the surface area is by combining carbon- or carbon-based nanostructures with TiO_2. Selvarani et al. investigated Pt-TiO_2/C prepared using sol-gel method with Pt:Ti atomic ratio 2:1 and they found high methanol tolerance of these catalysts while exhibiting high catalytic activity towards ORR [28]. Pt-TiO_2/ C cathode catalyst exhibited a higher power density of 180 mW/Cm^2 which is higher than Pt catalyst supported on carbon which is 80 mW/Cm^2. Because of their good conductivity, large specific surface area and good stability CNTs are also used with TiO_2 as composite support for fuel cells. Au nanoparticles with size around 3nm grown on TiO_2 nanotubes supports have also shown great catalytic activity and is found to be effective catalyst for oxygen reduction [29].

Cobalt oxides are alternative to expensive Pt-based catalysts electrode materials in fuel cells specifically as ORR electrocatalysts. Owing to their high surface to volume ratio, high theoretical power density, stable chemical states, and low cost, Co_3O_4 nanostructures have found applications in energy related devices such

as fuel cells [30], lithium-ion batteries [31] and supercapacitors [32]. Co_3O_4 has a spinel structure in which Co^{2+} and Co^{3+} ions occupy tetrahedral and octahedral voids and are promising materials for ORR applications due to the presence of the redox couple where electron transfer takes place. However, these materials are more stable in alkaline than in acidic media. Nevertheless, the catalytic activity is affected by the poor electrical conductivity and low ion conductivity. These limitations hinder the applications of these oxide-based materials in electrocatalysis. To mitigate the above-mentioned issues, conductive materials like carbon-based ones are used as supports to enhance the conductivity and thus the catalytic activity [33]. Liang.Y, et al. proposed Co_3O_4 nanoparticles grown on nitrogen-doped graphene (N-rmGO) as a good candidate for ORR and OER reactions [34]. Co_3O_4/N-rmGO was synthesized in a solution by general two step method explained in [34]. TEM results revealed Co_3O_4 particles size of 4-8 nm. They found that the activity of these materials in alkaline solution is similar to that of Pt but observed a higher stability. Nanocactus-shaped Co_3O_4 nanoparticles supported on carbon nanotubes (Co_3O_4/CNTs) in a chemical method have exhibited superior catalytic activity towards ORR and OER reactions in fuel cells and are more stable compared to Pt based materials [35]. TEM results showed various nano sized Co_3O_4 nanocactus with a single unit of length around 25nm and 5nm thick. The strong interaction between Co_3O_4 and CNTs, more abundant active sites, and good electron conductivity makes these nanomaterials as an effective alternative to the expensive noble metal-based catalysts in fuel cells [35].

Non- precious ***copper oxides (CuO_x)*** are also explored as electrocatalysts for ORR reactions. Due to their surface area, different oxidation states and chemical stability, CuO_x are studied for their applications in ORR but due to relatively lower conductivity and catalytic activity, they have limited applications [36]. One of the viable solutions to enhance the electrocatalytic activity is to mix CuO_x with carbonaceous materials such as graphene, carbon nanotubes etc. [36,37]. The electrical conductivity of CuO_x and thus the ORR activity of CuO_x is enhanced by using nitrogen doped carbon (CN) as support material. This is achieved by encapsulating $NdCuO_x$ bimetallic nanoparticles into CN [37] (i.e., $NdCuO_x$@CN). These catalysts also showed a better stability and methanol tolerance. Guo's group studied the homogenously dispersed Cu_2O nanoparticles on reduced graphene for methanol and CO-tolerance [38]. They observed remarkable ORR activity and stability in this catalyst (Cu_2O nanoparticles of around 4nm) making them a suitable cathode material for fuel cells.

Manganese (Mn) oxides have also been explored by many research groups for ORR reactions [39]. It is considered that the crystalline structure and the oxidation state of Mn plays a vital role in the ORR activity [40,41]. Catalytic activity of the Mn oxides is higher in the presence of Mn^{3+} ions which are more active than Mn^{4+} [42]. Mn-based oxides have shown better activity than Pt/C [43]. Mn based nanostructures are grown on carbon supports show an increased electron conductivity and ORR activity. Hazarika et al. have

shown that ORR activity of the Mn_2O_3 nanoparticles grown on carbon support is much better than the individual Mn-based oxide and also of Pt/C and Pd/C in alkaline media [44]. Mn_2O_3/C were prepared in a chemical solution method and the homogenous distribution of 6-8nm in spherical morphology were observed on the surface. However, due to its low electrical conductivity and weak electrochemical stability, its use as ORR electrocatalyst declined.

1.3 Ceria and ceria-based materials

Cerium oxide (CeO_2) also referred as ceria is a technologically prominent material due to its ability to store, release and transport oxygen. It has been used in diverse applications usually as a support material for its redox properties, predominantly in catalysis [45], solid oxide fuel cells [46], biomedicine [47] and water gas shift reactions [48]. Another interesting feature of ceria is that it can easily switch between Ce^{4+} and Ce^{3+} oxidation states depending on the surrounding atmosphere (oxidizing/reducing) reaction:

$$CeO_2 \longleftrightarrow CeO_{2-x} + \left(\frac{x}{2}\right) O_2 \quad (0 \leq x \leq 0.5) \tag{1.3}$$

Typically, in catalysis ceria acts as an active support by supplying lattice oxygen atoms whenever needed. Along with oxygen, surface hydroxyls species present on ceria surfaces are also involved in all important reactions such as water-gas shift and CO-oxidation reactions. Cerium oxide has a fluorite structure, as shown in figure 2, which illustrates the structure of a stoichiometric ceria (CeO_2), where red balls represent four coordinated oxygen and blue balls represent eight coordinated cerium [49]. The structure of ceria thin films depends on the growth methods, material substrate, deposition parameters.

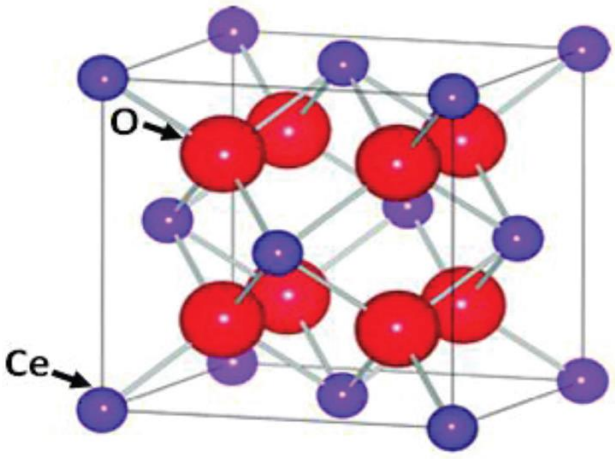

Figure 2: CeO_2 fluorite structure taken from [50].

In ceria, intrinsic defects are present due to growth conditions or induced from the redox reactions between ceria and the surrounding atmosphere. Defects can be also introduced as dopants or impurities to modify the characteristics of the oxide.

Cerium is the most reactive element in the lanthanide series with partially occupied f orbital and CeO_2 is the most stable cerium oxide. CeO_2 (111) is less reactive face in the fluorite structure. One monolayer of CeO_2 (111) consists of two layers of oxygen with a layer of cerium atoms in between (O-Ce-O) with thickness equal to 3.12 Å. Ce atoms in CeO_2 have a formal 4+ oxidation state, while in Ce_2O_3 , stable only under reducing conditions, , Ce atoms have a 3+ oxidation state. Ce^{4+} is the most stable among them as its electronic structure [Xe] $4f^0$ is more stable than Ce^{3+} with electronic structure [Xe] $4f^1$. Usually, CeO_2 is referred as cerium oxide due to its higher stability than Ce_2O_3, whereas Ce_2O_3 is the reduced oxide. As shown in Figure 2, in CeO_2, four Ce atoms surround the oxygen atom in the center of a tetrahedron. In the oxide, cerium provides two extra electrons to the p-band of each oxygen atom. During the oxygen vacancy formation, these two extra electrons from oxygen are left behind. The excess charge (two electrons) left by an oxygen vacancy occupies the lowest possible empty state, which is the 4f state of Ce. The condensation of these electrons into localized f-bands of Ce atom reduces two Ce ions from 4+ state to 3+ state. The oxygen formation process is schematically represented in figure 3.

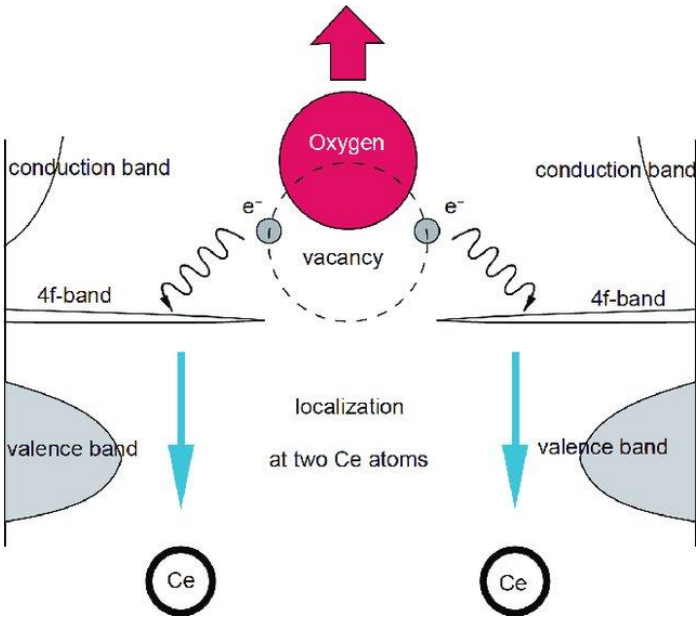

Figure 3: Schematic representation of oxygen vacancy formation process in cerium oxide, taken from [51].

As shown in the figure 3, stoichiometric CeO_2 consists of only +4 state ions and empty 4f levels. Reduced ceria results from oxygen vacancy formation from the lattice. The excess charge (2 electrons) left by an oxygen vacancy occupy the lowest possible empty state, which is the 4f state of Ce. This process reduces

two neighbor Ce ions from +4 state to +3 state. The reduction of ceria and doped ceria was studied by several groups [49,52] and are discussed in detail in the next sections. On the contrary in the oxygen rich atmosphere, the cerium atoms tend to oxidize to the 4+ state, as the electrons are transferred from Ce sites to oxygen.

Ceria plays an important role in the heterogenous catalysis as a catalyst and also as a support. Due to its high oxygen storage capacity, it serves as an active support for noble metals in catalysis as it enhances the activity, mechanical and thermal stability of the catalysts. Along with pristine CeO_2, ceria doped with different elements [53,54] has also shown promising results. In general, the investigated properties are influenced by the dopant concentration and type, however the overall crystal structure is generally not significantly affected [55].

1.3.1 Doping effect on oxygen vacancy formation and reduction properties

Ceria catalytic properties can be significantly altered by doping it with cationic species with different electronic properties. Numerous theoretical and experimental works on doped CeO_2 can be found in the literature. Usually, a dopant atom induces a structural distortion in the crystal lattice structure. This typically induces a reduction in the oxygen vacancy formation energy [56]. The vacancy formation energy is also dependent on the valence of the dopant. As the valance of the dopant is different from +4 state of CeO_2, it induces a modification in the electronic structure of the material and thus a decrease in the oxygen vacancy formation [57]. Also, the preparation methods have an impact on the investigated properties [58,59]. Generally, the cation doped metal-oxides are reported to show a higher catalytic activity [54]. Usually, the dopant cations occupy the ceria substitutional cites. In the case of trivalent rare earth cations (RE^{3+}), the substitution of the Ce ion in the fluorite structure causes the alteration to the local chemistry. The alteration arises due to the different size and charge of the dopant that introduce charged defects such as oxygen vacancies in the host material. Andreeva et al. have investigated the catalytic properties of gold catalyst on different Re-doped ceria. The catalyst supports were prepared using two methods (co-precipitation and mechanochemical activation) and the gold nanoparticles of 2-3 nm size were observed. They reported that the Yb- and Sm-doped ceria as gold catalyst support showed higher catalytic activity than La-, Gd-, Y-doped ceria [48]. This behavior was observed due to the altered redox (Ce^{3+}/Ce^{4+}) reaction. The effect of ionic radius of the dopant atom on the reducibility of ceria was investigated by doping (10% mol) epitaxial thin ceria films with RE atoms such as La, Sm, Gd and Yb with different ionic radius [55] prepared using solid-state reaction methods. In situ XPS measurements using synchrotron radiation on these films were performed to understand the role of dopant atoms on the Ce^{3+} formation. The results revealed that the decrease in the ionic radius of the dopant atoms increases the reduction of ceria due to lattice

relaxation. So, the Yb^{3+} with smaller ionic radius (0.985 Å) showed higher reduction than the pristine CeO_2 in UHV conditions.

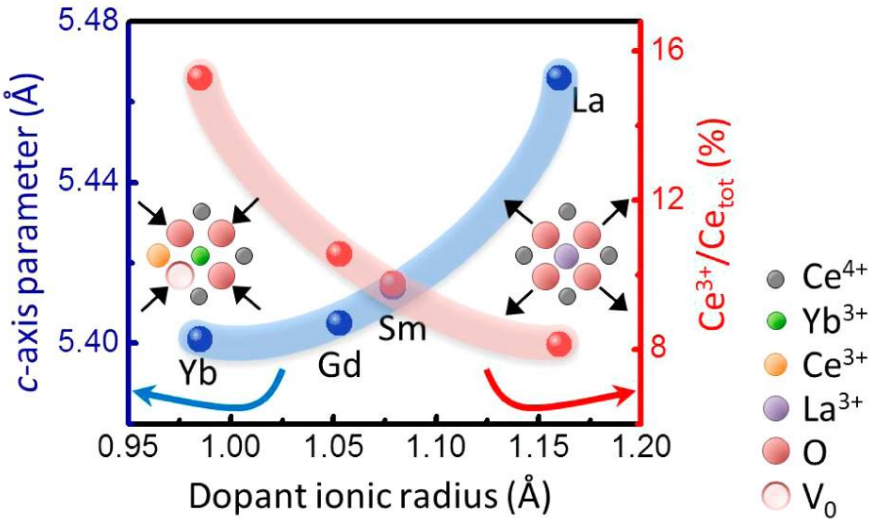

Figure 4: Relation between the ionic radius of the RE cation dopants vs Ce^{3+} concentration and c-axis parameter taken from ref [55].

Relation between dopant ionic radius and Ce^{3+} concentration for other RE cations is shown in figure 4. However, the conductivity was found to increase linearly with the dopant ionic radius up to 500°C. Furthermore, Sm- and Gd-doped ceria systems were studied both experimentally and by first principles with density functional theory (DFT). Samples were prepared using hydrothermal synthesis route. The study showed that the reducibility of Sm-Gd doubly doped ceria is lower than the single dopant (Sm^{3+}/Gd^{3+}) and pure ceria [60]. Sm-Gd doubly doped ceria showed also a higher ionic conductivity (4.012×10^{-2} S cm^{-1}) than other single doped samples.

The effect of dopant on the oxygen vacancy energy formation in CeO_2 (111) is also quite important as it affects the reducibility of the cerium and thus the catalytic properties. Zhenpeng Hu and Horia Metiu studied the effect of dopants on the oxygen vacancy formation energy [56]. They focused on understanding if the dopant atoms affect only locally, or if they also have long-range effects on the properties of ceria. It was reported that low-valance dopants (La and Y) have both short- and long-range effect. The oxygen vacancy formation energy is reduced from 3.00 eV for undoped ceria to 1.35 eV near to the dopant when CeO_2 is doped with La and to 1.63 eV when the vacancy is far away from the dopant. Oxygen vacancy formation energy was observed to be the same for several dopants such as Pt, Ru, Nb, Ta, Zr, Mo and W in CeO_2 (111) and affected only at short-range. It was speculated that the similar energy observed for oxygen vacancy formation is due to the tetravalent nature of the chosen dopants, which is the same as Ce ions in the host material. However, the effect of these dopants on the oxygen vacancy formation is only short

ranged. The linear relation between the oxygen vacancy formation energy and the Bader valence of the dopant atoms i.e., the number of electrons lost by the dopant is shown in the figure 5.

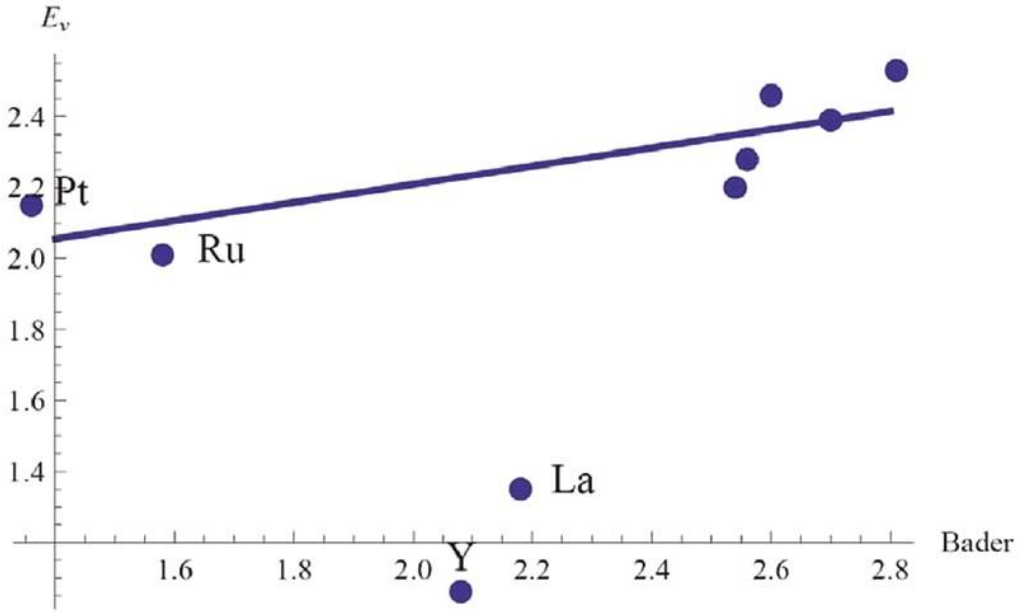

Figure 5: The relation (dependency) between the oxygen formation energy and the Bader valance of the dopant, taken from [56].

The energy for the oxygen vacancy formation shown in figure 5 is related to the oxygen in the surface layer closer to the dopant. The energy of oxygen vacancy formation is lower as explained before near to the dopant atom than far away from it, due to the chemical bond between the dopant and the oxygen atoms (local effect). The effect of Zr dopant on the reduction properties [61] and of Pd doping on the oxygen vacancy formation energy of CeO_2 [62] are studied using DFT. The energy to create an oxygen vacancy in Pd-doped system was observed to be as low as 0.59 eV (2.99 eV for undoped ceria) due to electronic effects, whereas in Zr-doped ceria, the structural distortion of the bonding between Ce-O and Zr-O plays a major role in the vacancy formation. Near the Zr dopant atom, the oxygen vacancy formation is facilitated with a reduction in the formation energy by 0.6 eV per vacancy. Subsequently, the two electrons formed due to oxygen vacancy reduce two Ce ions from 4+ to 3+ state. DFT+U calculations were also performed on divalent cations (Pd and Ni) as dopants in CeO_2(111), to investigate the effect on oxygen vacancy formation energy [57]. Due to their 2+ oxidation state, which is lower than the host Ce, oxygen vacancies are spontaneously formed to compensate the dopant oxidation state. On the Pd-doped CeO_2(111) surface, the energy for active oxygen formation is +1.32 eV and 1.45 eV for Ni doped CeO_2(111), which are much lower than on pristine ceria.

Ag- and Cu-modified CeO_2(111) epitaxial films grown on Pt (111) were investigated in UHV environment to understand the effect of the dopant atoms on the reducibility of the ceria films and are compared to DFT calculations [49]. Films were prepared using PVD method, where e-beam evaporator and effusion cell were employed to deposit Ce and Ag/Cu respectively. The initial concentration of cations in the oxide were found to be 12-13 at.%. Reduction cycles was performed in UHV conditions and oxidation in O_2 background pressure (figure 6).

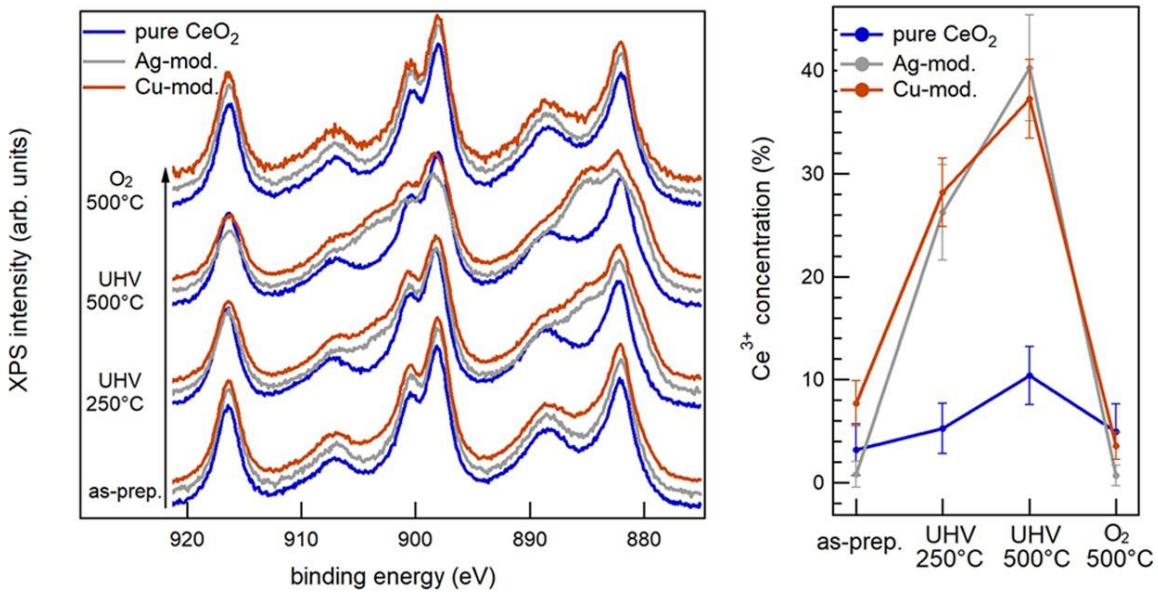

Figure 6: Ce 3d spectra of pure, Ag-and Cu-modified CeO_2 as grown and at different treatments, and evolution of Ce^{3+} ion concentration at different treatment steps taken from ref [52].

As shown in figure 6, the Ce 3d spectra of modified ceria show higher reducibility than the pristine ceria at different annealing temperatures in UHV. Notably, the modified films already exhibit a slightly reduced nature at RT. The evolution of the Ce^{3+} ion concentration is much higher in Ag-modified and Cu-modified CeO_2 films than pristine CeO_2. The higher reducibility of the modified films observed is due to the lower activation energy for oxygen vacancy formation compared to pristine ceria. It was found that the modified ceria forms a spontaneous vacancy near to the surface cation due to the negative formation energy which is -1.40 for Cu and -1.36 eV for Ag. Calculations have shown that when an active oxygen vacancy is formed, one Ag atom is reduced from 2+ to 1+ along with the reduction of one Ce atom from Ce^{4+} to Ce^{3+}. Also, Cu showed a similar trend which is in line with the experimental results. Dopant atom oxidation state has a significant role in the reducibility of ceria. DFT studies on Cu doped CeO_2 (111) showed that the Cu atoms cause lattice distortion, contrary to Ag [63]. It was found that the electrons left from oxygen vacancy formation are transferred mainly to Ag atoms.

The electronic properties of Fe-doped CeO_2 nanoparticles with different doping concentrations ranging from 1 to 11% were investigated by X-ray absorption and X-ray emission spectroscopy [83]. Precipitation method was employed to prepare Fe-doped CeO_2 NPs using $Fe(NO_3)_3.6H_2O$ and $Ce(NO_3)_3 \cdot 6H_2O$ as precursors. A decrease in the bandgap and variation in the oxidation states of Ce and Fe upon doping was reported. But the effect of doping level on the on the magnetism was studied and it was observed that below 5% doping favors ferromagnetism and above 5% favors antiferromagnetism. Oxygen vacancies were formed at faster rate in the lower doped samples than higher doped samples which were attributed to the different behavior in the magnetism explained before. The effect of Fe doping on the optical and structural properties were investigated by Duangdao. C et al [84]. Fe-doped CeO_2 thin films were prepared by spin-coating method employing sol-gel precursors on F-doped tin oxide glass with dopant concentrations varying from 2 to 10% followed by annealing at 500°C for 15 hours. A red shift in the absorption edge was noticed due to the lower of bandgap from 3.48 eV to 3.20 eV due to Fe doping. They also reported the formation of a solid solution of Fe dopant with Ce-O lattice. The formation of the solid solution and decrease in the optical bandgap are attributed to the presence of Fe^{3+} valence state ions. Nanocrystallites of $Ce_{1-x}M_xO_{2-\delta}$ (where M corresponds to Fe, Zr, Ti and Pr) 5-12 nm prepared hydrothermal synthesis route was studied [85] for the oxygen storage capacity (OSC). Nanocrystallites with Fe (15%) showed higher oxygen capacity compared to Zr (25%) where Fe^{3+} (15%) were substituted in the CeO_2. Also, it was claimed that the CeO_2 and $Ce_{1-x}M_xO_{2-\delta}$ nanocrystallites prepared by this method showed higher OSC than others reported in the literature.

1.3.2 Ceria as support material for metals (Cu, Ag and Au)

The interaction between metal nanoparticles and ceria is a very interesting topic and is also relevant for applications in catalysis. Along with the intrinsic properties of the metal nanoparticles, the preparation method plays a huge role in the final properties of the metal/oxide systems. The enhanced properties of the metal nanoparticle / oxide systems are due to their strong interaction. These systems are also complex in nature so there is a great deal of research running on these systems. Noble metal nanoparticles (Cu, Ag and Au) are particularly used for catalytic purposes and attention is given to the redox properties of the oxide and the stability of the metal nanoparticles on the CeO2 surface.

Ye et al. [64] studied the Cu loading on CeO_2, with different ratio of copper and CeO_2 amount (wt.%). The samples were prepared using wet-impregnation method and an enhancement in the catalytic activity of the system was observed. The exhibited activity is related to the better conductive paths for electrons provided by the Cu atoms and also to well-connected reaction sites on the surface. The properties of Cu adsorbed on CeO_2 (111) surface were investigated using first principles calculations [65,66] and they showed the existence of Cu^{1+} on the surface of the ceria. Campbell et al. studied the interaction between vapor deposited

Cu nanoparticles and ceria [67]. Average particle diameter of 1.8 to 2.6 nm with different coverages. Due to the nature of Cu nanoparticles interaction and binding strength between Cu and ceria, Cu forms clusters at the step edges at the deposition temperature of 300 K as shown in the figure 7.

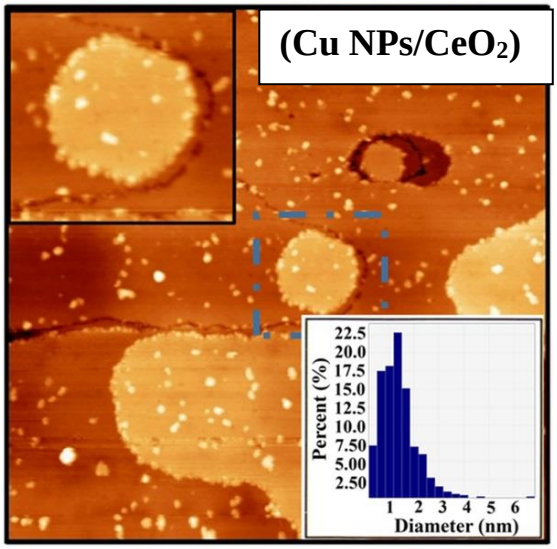

Figure 7: STM image of Cu (0.05 ML) deposited on CeO_2 film of 2 nm thickness, the inset shows the Cu particles at the step edge on the CeO_2 island, taken from ref [68].

As the amount of Cu atoms deposited increases, the particle size increases. DFT calculations performed on the Cu nanoparticles on CeO_2 (111) showed that the adsorption of Cu atoms on the non-defective sites forms Cu^+ species, due to the charge transfer between the support and the oxide [66]. The charge transfer is mostly occurring at the interface between metal and oxide.

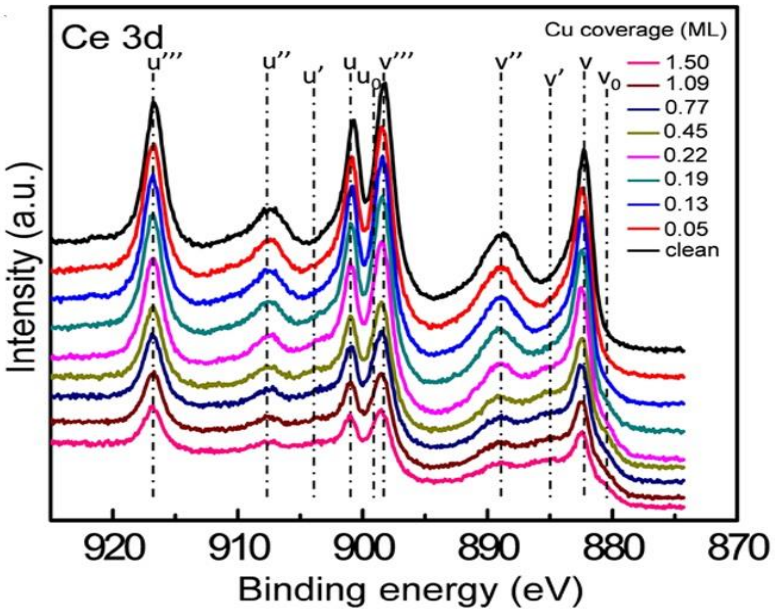

Figure 8: Ce 3d XPS spectra taken after the deposition of various amount of Cu atoms at 300 K taken from reference [68].

A shift in the Ce 3d spectra to higher binding energies is observed after the deposition of Cu atoms onto the surface of ceria [68]. Also, the contribution of Ce^{3+} ions start to appear due to the reduction mechanism due to charge transfer from Cu to the support ceria. The effect of Cu deposition on ceria is shown in figure 8. It is clearly visible from the figure that the Cu atoms lead to the reduction of Ce ions on the surface of the film (presence of $u_0 + v_0$ and $u^1 + v^1$) and also the shift in the Ce 3d spectra is clearly evident.

In a joint experimental and theoretical study on Ag nanoparticles deposited on CeO_2 films (both stoichiometric and reduced), Luches et al. [69] observed a reduction in ceria after the vapor deposition of Ag on the surface, due to the direct electron transfer from Ag to Ce. The reverse oxygen spillover from support to the Ag NP is less favorable compared to the direct electron transfer from the Ag NP to ceria support. They investigated the evolution of Ce^{3+} ion concentration for 0.07 Å, 0.2 Å Ag deposited on CeO_2 (111) and also 0.2 Å Ag on reduced ceria for different annealing treatments in UHV. The reduction of the samples was similar within the same annealing temperature range, indicating the non-dependency of the thermal treatments on the Ag nanoparticles. STM images of the 0.07 Å and 0.2 Å Ag deposited on 3 ML CeO_2 (111) are shown in figure 9, taken from reference [69].

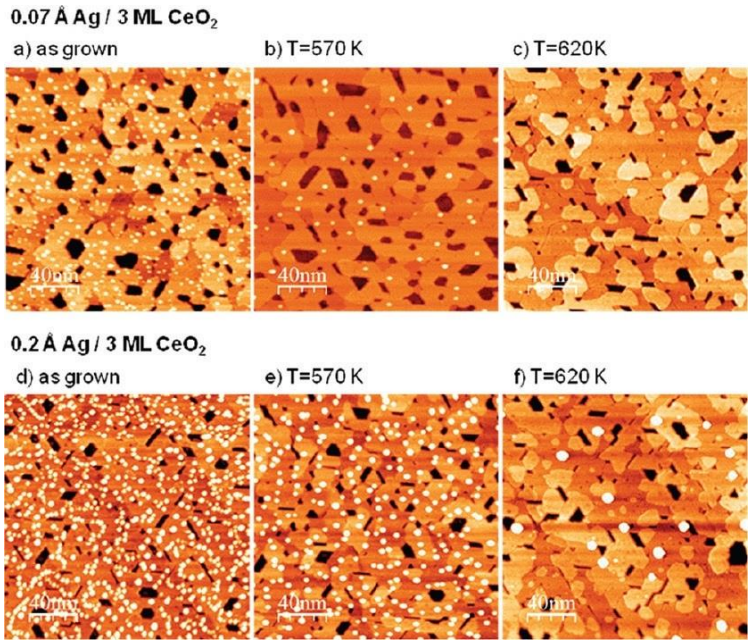

Figure 9: STM image of 0.07 Å Ag deposited on 3 ML CeO_2 (111) (a), the reduction of the same at 570 K (b) and 670 K (c). 0.2 Å Ag on 3ML CeO_2 (d), reduction treatment of the same at 570 K (e) and 670 K (f). Taken from reference 69.

The stability of Ag NPs on the surface of CeO_2 at different annealing temperatures was also investigated [69]. The notable effect observed was that the nanoparticles tend to coalesce after 570 K and form bigger clusters. Particularly in 0.07 Å Ag sample the density is significantly affected after annealing at 570 K, all the nanoparticles disappeared at 620 K. A similar trend was also observed in 0.2 Å Ag sample.

Au atoms/clusters supported on ceria represents an interesting metal-oxide catalytic system. Vapour deposited (1 ML) of Au nanoparticles on CeO_2/Si (111) at RT was investigated by Megginson et al [70] found that the adsorption of Au atoms on CeO_2 (111) surface is much stronger at defect site (O-defect) than non-defective site. At the adsorption site (O-defect site), the electron is transferred to Au atom from one of the Ce^{3+} ions making Au negatively charged. However, the adsorption of a Au atom on the non-defective surface, creates a positively charged Au as the Ce^{4+} ion accepts the electron from the Au adatom. The reduction of ceria by the metal nanoparticle deposition is observed also for the Au case. The deposition of Au nanoparticles (1 ML) on CeO_2 induces a partial reduction of Ce^{4+} from 91.2 % to 88.6 %. Au $4f_{7/2}$ peak was also observed to be shifted by 0.6 eV towards higher binding energy than the metallic gold. The XPS spectra of Ce 3d and Au $4f_{7/2}$ are shown in figure 10.

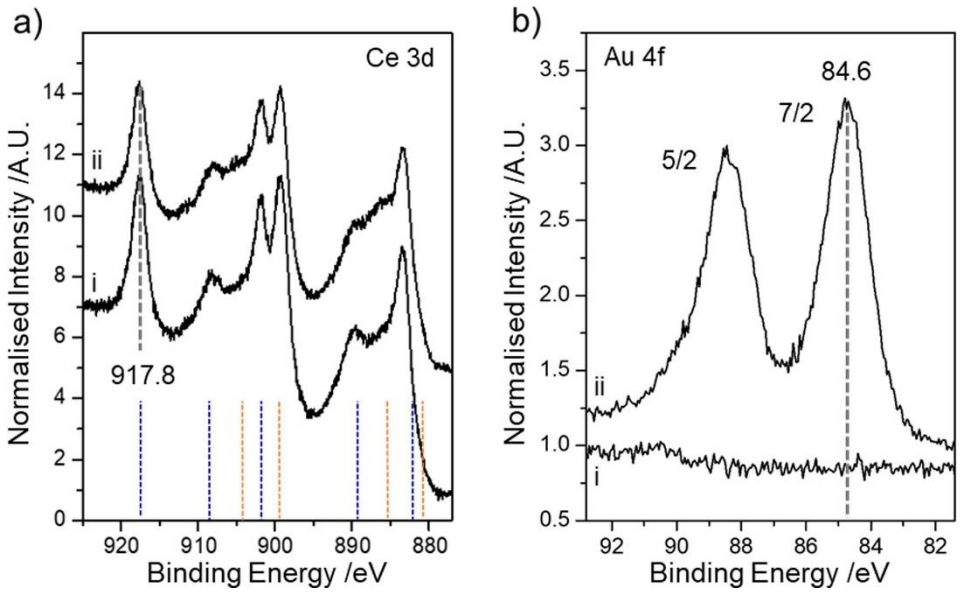

Figure 10: XPS spectra of (a) Ce 3d and (b) Au $4f_{7/2}$ regions on CeO_2/ Si (111) surface; (i) before Au deposition and (ii) after Au deposition [70].

In figure 10, there is a clear indication of the reduction of CeO_2 after the deposition of Au and a shift in the binding energy of Au $4f_{7/2}$ to 84.6 eV from 84 eV of metallic gold is also visible. They further deposited 1.6 ML Cu via vapor deposition onto the already prepared Au/CeO_2/Si (111) at 300 K. The deposition of copper further reduces the ceria from 88.6 to 83.2 % (Figure 11 (a)). Some Cu is found to be deposited onto

the gold NPs but the majority forms pure Cu NPs on the ceria film. Cu/Au/CeO_2/Si (111) was annealed at increasing temperature up to 540 K. The reduction of ceria was found to be increasing with the annealing temperature and the ratio of Ce^{4+}/Ce^{3+} ratio reaches up to 1:3 at the highest annealing temperature (Figure 11 (b)).

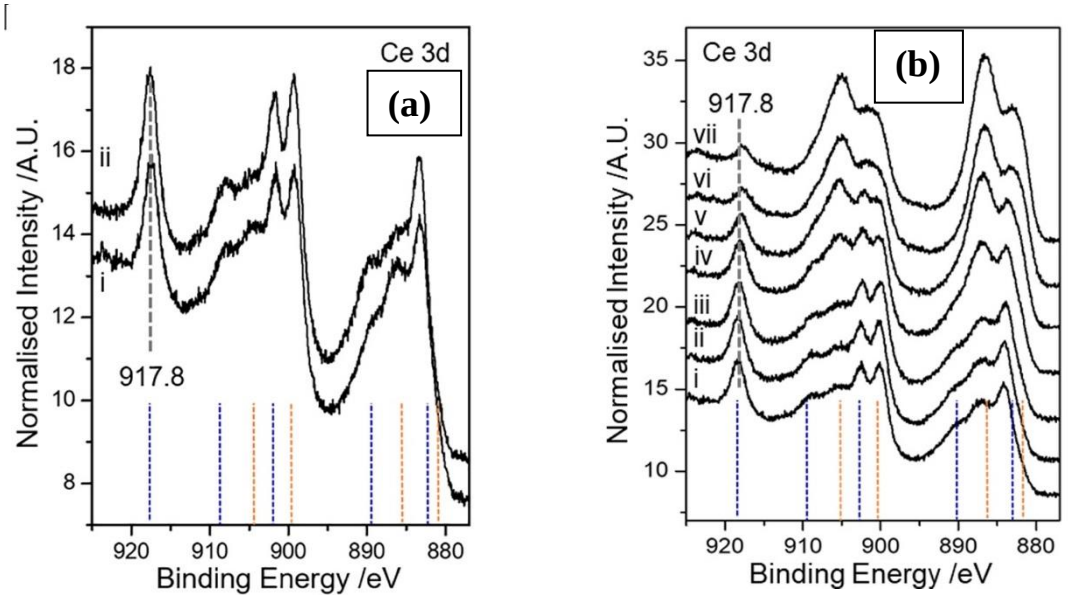

Figure 11: XPS spectra of (a) Ce 3d region; (i) before deposition and (ii) after 1.6 ML Cu deposition on 1 ML Au deposited on CeO_2 /Si (111) at 300 K , (b) annealing treatments of the same (i) as prepared, (ii) 325 K, (iii) 375 K, (iv) 425 K, (v) 475 K, (vi)510 K and (vii) 540 K. Blue dotted lines correspond to Ce^{4+} and orange ones correspond to Ce^{3+} [70].

This work also provides information on the thermal stability of the Au and Cu particles on the CeO_2 surface as well as on the particle size, alloying information and the electronic interaction between the ceria support and the metal particles that could help in the design of catalysts based on Cu/Ag/CeO_2 system for applications such as hydrogenation reactions. Single atom copper catalysts prepared by high-temperature synthesis on ceria [81] has found to be active in low-temperature CO oxidation proceeds via trapped Cu single-atoms trapped at the step defect. The charge transfer mechanism between support and Cu allows the catalyst to be active and the strong Cu-O interactions provide a great stability for this system. Aggregation of Cu and formation of CuO phase in the higher Cu loading (6 and 10 wt%) was observed at calcination temperatures up to 800° C and 2 wt% loading did not show this behaviour. The preparation method had a great impact on the stability of these catalysts.

Maria Lykaki et al investigated the effect of the ceria morphology on the redox properties and CO oxidation on Fe_2O_3/CeO_2 mixed oxides [82]. Samples of bare ceria were prepared by hydrothermal method described elsewhere and Fe-Ce mixed oxides were prepared by wet impregnation method. The redox properties were

assessed in H_2-TPR experiments, the rod-shaped ceria structures were highly reduced compared to cubes and polyhedral morphologies due to high availability of weakly bound oxygen species. The same trend was observed in the case of CO conversion which evidences the effect of the shape of the support material on the properties of a catalyst.

1.3.3 Interaction between ceria-based materials and H_2

The surprising ability of ceria to dissociate hydrogen on its surface has opened new paths to use this interesting material in catalysis processes involving this gas. The ability of ceria to break hydrogen in the absence of noble metals is an economical advantage. It is usually considered that the H_2 dissociation mechanism on the ceria surface follows a heterolytic pathway forming a hydride and hydroxyl pair, followed by the transfer of the H atoms bound to Ce towards surface O atoms, forming only hydroxyl groups on the surface. During this process, two cerium atoms are reduced from Ce^{4+} to Ce^{3+} state as the electrons in the dissociation process are transferred to cerium atoms. To break H-H bond on the (111) surface requires around 0.7 eV more energy than for the molecular adsorption on the surface [71]. Several research works have investigated the interaction of bulk or polycrystalline ceria with H_2 [72,73]. Recently, many groups have also investigated the interaction between well-defined structured CeO_2 such as nanostructured ceria films and H_2 under controllable environment (UHV) which has provided greater insights into the induced modifications in the properties of the ceria at atomic level [74,75]. The interaction between H_2 and CeO_2 in a temperature programmed reduction has been studied to obtain information on the reducibility of the ceria [76].

The H_2 dissociation mechanism on pure and non-noble metal doped CeO_2(111) has been investigated due to potential applications in many fields such as fuel cells etc. Furthermore, the chemical state of the dopant atoms plays an important role in the reducibility as well as on H_2 activation on the CeO_2 surfaces. In one of the combined experimental and theoretical studies Matolin et al., investigated the reactivity of isolated Pt^{2+} species and the H_2 dissociation mechanism on these sites [77]. They prepared 5%, 15% and 18% Pt-CeO_2 films via thermal vapor deposition on Cu (111).

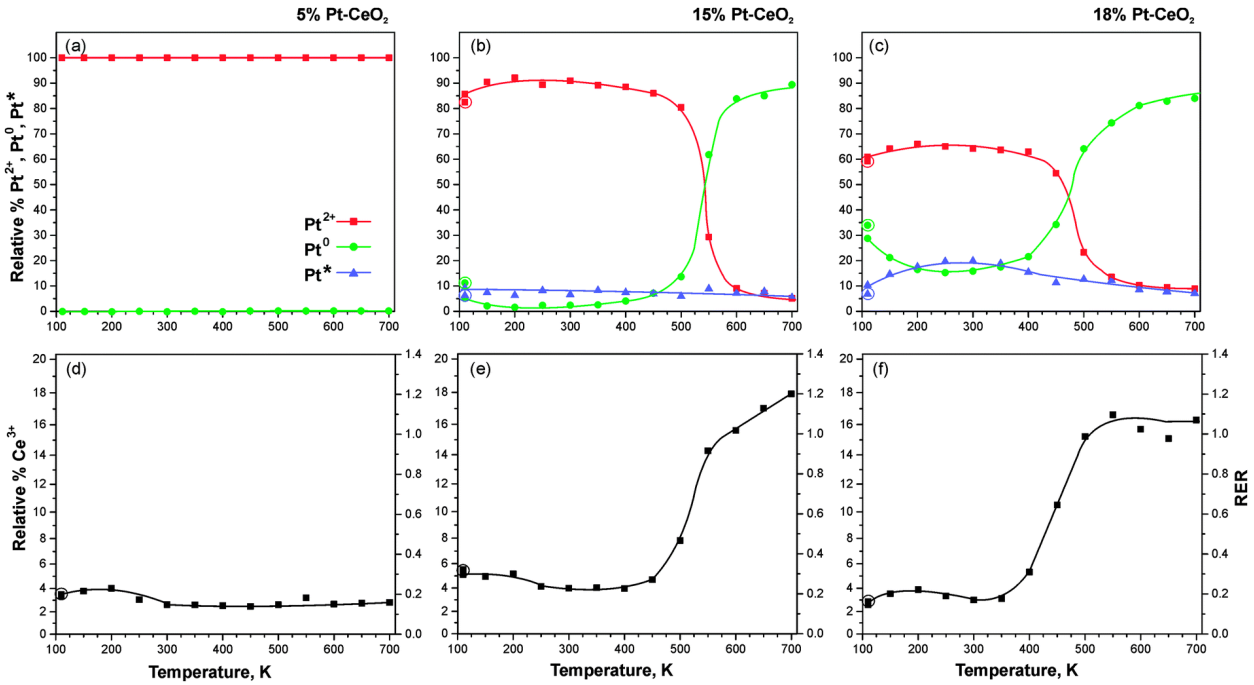

Figure 12: Relative concentration of Pt ions (Pt^{2+}, Pt^0, Pt*) per deposited Pt content (a–c) and Ce^{3+} concentration evolution for 5% Pt–CeO_2 (a and d), 15% Pt–CeO_2 (b and e), and 18% Pt–CeO_2 (c and f) films vs annealing temperature under exposure to 50 L H_2. Taken from [77].

As shown in Figure 12 they demonstrated that atomically isolated Pt^{2+} species in Pt-CeO_2 fuel cell catalysts are inactive towards the H_2 activation process. A small amount of metallic Pt species on the surface is required to keep the activity of Pt^{2+} species. They also found that the barrier for H_2 activation in the presence of Pt^{2+} sites increase to 1.2 eV from 1.0 eV for pure CeO_2. The 5% Pt-CeO_2 sample showed no activity due to higher activation energy for H_2. Whereas 15% and 18% Pt-CeO_2 films showed a coupled reduction mechanism of both Pt^{2+} and Ce^{4+} during the interaction with H_2 at higher temperatures. DFT calculations performed by the same group showed the dependency of the Pt^{2+} species on the oxygen vacancies, Ce^{3+} species, and the concentration of the Pt^{2+} on the surface. As these parameters affect the reduction of Pt^{2+} to Pt^0, these calculations provide a way to understand Pt-based catalysts mechanism for the H_2 activation process. So, the investigation of both Ce and dopant atom reduction during the treatments in H_2 is necessary to understand the underlying mechanism.

Single atom catalysts (SACs) have been attracting researchers as they exhibit high catalytic activity, selectivity, stability. Also, they provide the way to utilize nearly 100% of the noble metal catalytic atoms. Giulia Righi et al. [78] used DFT calculations to investigate the H_2 dissociation mechanism on Ag single atom catalyst adsorbed on pure CeO_2 (111), on Ag-substituted reduced CeO_2 surface and also on partially hydrogenated surfaces.

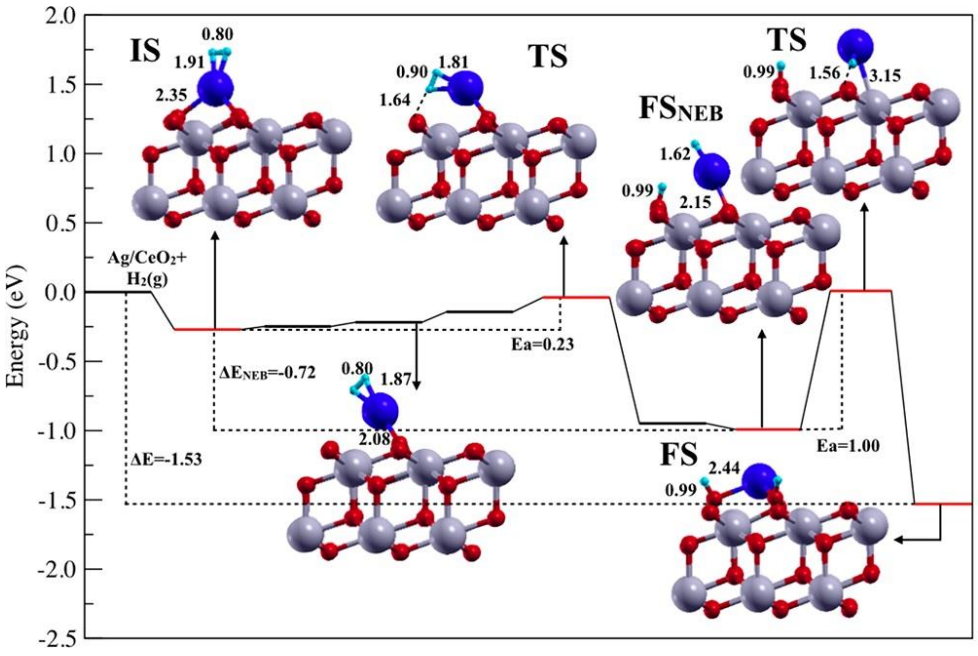

Figure 13: The minimum energy pathway for H_2 dissociation on Ag/CeO_2 (111) obtained by CI-NED calculations taken from ref [78]. The hydrogen, oxygen, cerium and silver atoms are represented in light blue, red, gray and blue balls.

Computational studies on H_2 dissociation mechanism on Ag/CeO_2 were performed using climbing image nudged method (CI-NEB) and the mechanism is shown in figure 13. In the initial state (IS), the H_2 molecule is physically adsorbed and in the final state (FS_{NEB}) the hydrogen molecule is dissociated on the surface. The dissociation of H_2 is considered to take place on the Ag adatom. In the initial state (IS), the bond length of H_2 is 0.8 Å and the Ag-H distance is 1.91 Å. At the transition state (TS), the bond length of hydrogen molecule increases from 0.8 to 0.9 Å. One of the H atoms forms a bond with O atoms with a bond length of 1.64 Å and the other H atom is bonded to an Ag atom. They found that the FS_{NEB} is an intermediate state due to the higher transfer energy (1.0 eV) required for H atom transfer from Ag to surface oxygen. In the final state one H atom is bonded to Ag with a bond length of 1.62 Å, while the other H-atom bonded to surface oxygen O_S with bond length of 0.99 Å and the Ag adatom is bonded to only the oxygen on the surface with bond length of 2.15 Å. The H atom which is adsorbed on the surface oxygen transfers its electron to a surface Ce atom and reduces it to 3+ while the other H-atom reduces the Ag atom from Ag^{1+} to Ag^0. It was found that H_2 activation energy is lowered by 0.6 eV than pure CeO_2 Also, the dissociative adsorption energy of H_2 was found to be lower in Ag/CeO_2 than dopant-free ceria [78].

S. Benedetti et al. investigated the surface reactivity of Ag-modified ceria oxide films to hydrogen [79]. The reduction mechanism of the Ag-modified cerium oxide films during thermal annealing treatments in both UHV and in the H_2 atmosphere was also investigated. DFT calculations were also performed to assist

the experimental investigation. Both in UHV and in H_2atmospheres, Ag:CeO_2 films showed a lower concentration of Ce^{3+} concentration compared to pristine CeO_2 (figure 14 (a)), even though more oxygen vacancies were formed after H_2 exposure. .The electrons created by oxygen vacancies and adsorbed H atoms are acquired mostly by Ag atoms so, the observed concentration of Ce^{3+} is lower compared to pure ceria. At lower annealing temperatures in H_2, a higher number of O-H species (figure 14 (b)) were found on the surface of Ag:CeO_2 films than pristine CeO_2 due to reduced H_2 dissociation barrier. But at higher annealing temperatures, O-H weight on Ag:CeO_2 films were lower than pristine CeO_2 because of high amount water formation on the surface of Ag:CeO_2. Both DFT and experimental results confirmed that Ag dopant atoms reduce the activation barrier for adsorbed H on the surface. So, a lower O-H was identified on the surface of Ag:CeO_2 at higher temperatures than pristine CeO_2 (figure 14 (b)).

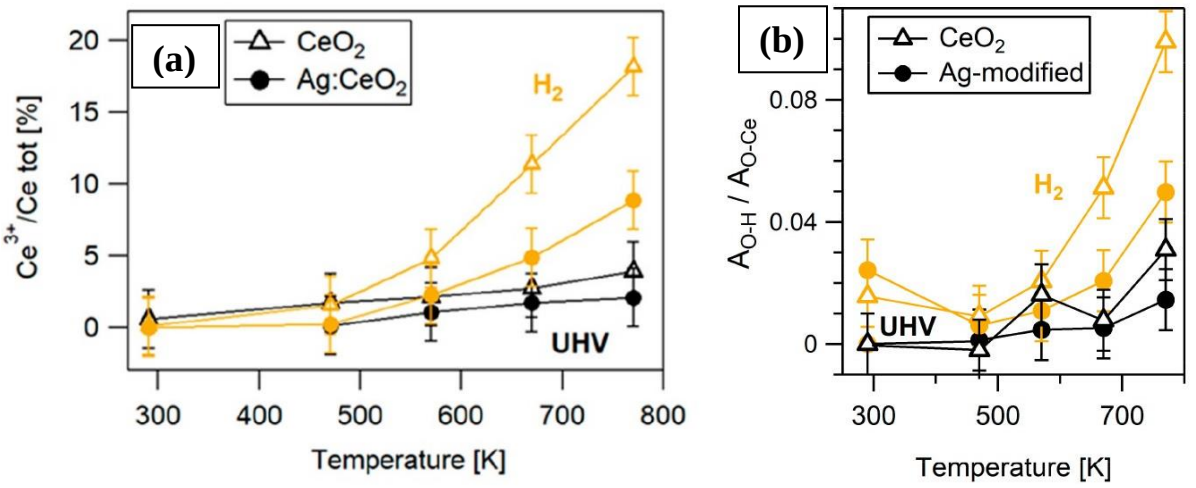

Figure 14: Ce^{3+} evolution as a function of temperature in both UHV and H_2 for pure and Ag-modified CeO_2 (a), and ratio between O-H and O-Ce after thermal steps (b) [79].

It was found that the electrons created by oxygen vacancies and adsorbed H atoms are acquired mostly by Ag atoms with a reduction of Ag from 2+ to 1+. So, the number of the electrons acquired by ceria and the reduction in Ce is lower compared to pure ceria. Also, the water formation on the surface of Ag-modified CeO_2 is observed to be more effective than on pure ceria. This is confirmed by the lower weight of OH-component (Figure 14 (b)) and high concentration of oxygen vacancies created during hydrogen thermal treatments. The water formation on Ag-modified ceria is due to the decrease in the activation barrier for surface diffusion of H atoms on the surface.

The oxidation state of the dopant atoms and the host material has a great influence on the final properties of the CeO_2 based systems. So, the investigation on the evolution process of the oxidation states of the dopant and the Ce atoms during experiments in different atmospheres is vital to synthesize a suitable

catalytic material based on CeO_2 for the real applications. Among the characterization methods soft x-ray absorption spectroscopy employing synchrotron radiation is an advanced technique which provides the electronic and chemical properties of the material in UHV and ambient pressure conditions with a great detail.

The chemical properties of $Ce_{1-x}Cu_xO_2$ and CuO_x/CeO_2 nano systems were studies using X-ray absorption spectroscopy by Wang et al. [80]. They found that the introduction of the Cu dopant atoms introduces a large strain in the oxide and supports the formation of O vacancies leading to the reduced stoichiometry. The reduction properties of the above-mentioned systems in H_2 were studied using in situ time resolved XAFS using synchrotron source. It was revealed that Cu atoms substituted the host Ce atoms in CeO_2 from EXAFS data. Cu-K edge XANES absorption spectra were taken for CuO_x/CeO_2, and $Ce_{1-x}Cu_xO_2$ and are compared to standard references of metallic and oxidized Cu in figure 15.

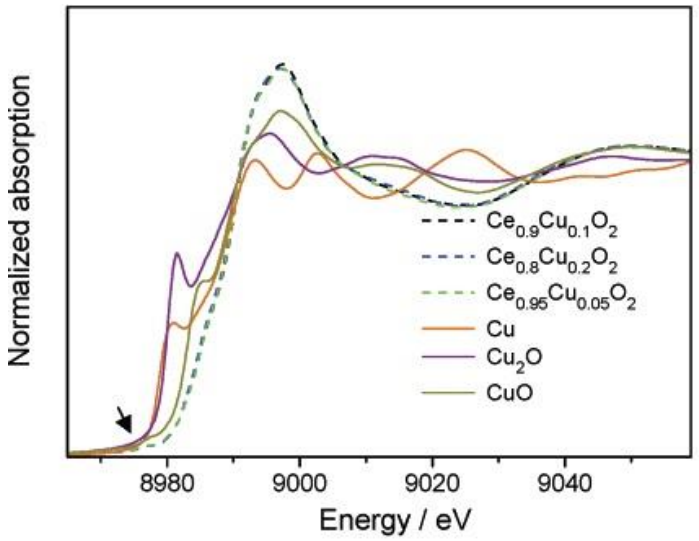

Figure 15: XANES spectra (Cu K-edge) for CuO, Cu_2O, Cu and $Ce_{1-x}Cu_xO_2$ (for different x values 0.05, 0.1, 0.2) taken from reference [80].

These spectra provide a great deal of information on the local symmetry and oxidation state of Cu. The arrow at 8897 eV corresponds to a dipole forbidden electronic transition (1s to 3d) for Cu^{2+} species. From figure 15, the charge of Cu in the doped samples is evidently more positive than in CuO. In-situ time resolved XANES spectra of Cu K-edge for $Ce_{1-x}Cu_xO_2$ were also collected during reduction in H_2 (5% H_2/He) and re-oxidation in O_2 (5% O_2/He) and are presented in figure 16.

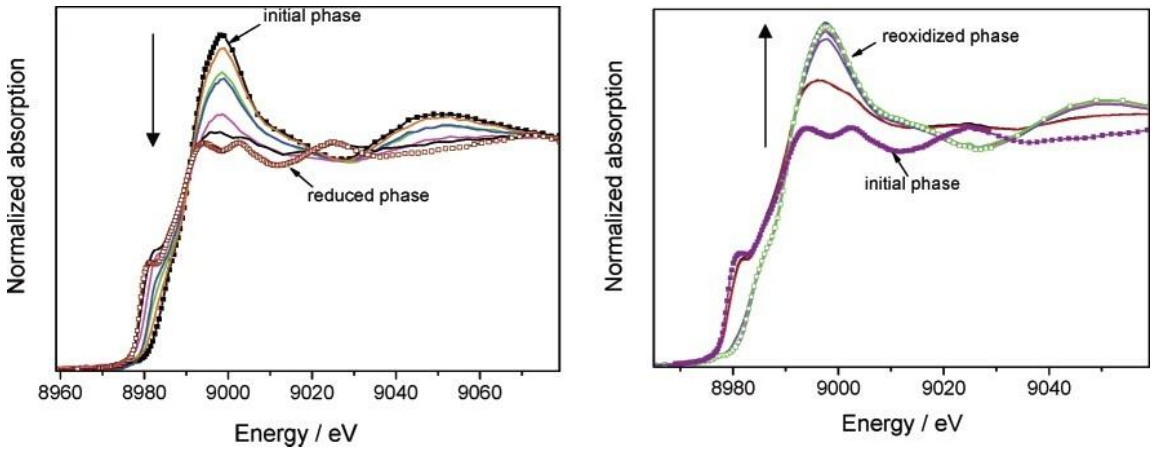

Figure 16: Time resolved XANES spectra of Cu K-edge during reduction and oxidation process as a function of time at 300°C of $Ce_{0.8}Cu_{0.2}O_2$, taken from [80].

They observed an induction time during the reduction process in H_2 and it was gradually decreased as the temperature raised. Also, a dependence on the reduction of Cu on the reaction temperature was noted. From16, the reduction and reoxidation mechanism of Cu is shown to be possible in the oxide. During re-oxidation process, the amount of CuO or Cu_2O phases formation was negligible. Moreover, the reduction of the Cu embedded in ceria was found to be hard when compared to the pure copper oxides. These findings provide important information on the effect of Cu on cerium oxide and also show the novel properties exhibited by the Cu doped ceria.

1.4 Bibliography:

1. Sui, S., Wang, X., Zhou, X., Su, Y., Riffat, S., & Liu, C. J. (2017). A comprehensive review of Pt electrocatalysts for the oxygen reduction reaction: Nanostructure, activity, mechanism and carbon support in PEM fuel cells. *Journal of Materials Chemistry A*, *5*(5), 1808-1825
2. Shao, M., Chang, Q., Dodelet, J. P., & Chenitz, R. (2016). Recent advances in electrocatalysts for oxygen reduction reaction. *Chemical Reviews*, *116*(6), 3594-3657.
3. Hardman, S., Chandan, A., & Steinberger-Wilckens, R. (2015). Fuel cell added value for early market applications. *Journal of Power Sources*, *287*, 297-306.
4. Wang, Y., Diaz, D. F. R., Chen, K. S., Wang, Z., & Adroher, X. C. (2020). Materials, technological status, and fundamentals of PEM fuel cells–a review. *Materials Today*, *32*, 178-203.
5. Tellez-Cruz, M. M., Escorihuela, J., Solorza-Feria, O., & Compañ, V. (2021). Proton exchange membrane fuel cells (Pemfcs): Advances and challenges. *Polymers*, *13*(18), 3064.
6. Peighambardoust, S. J., Rowshanzamir, S., & Amjadi, M. (2010). Review of the proton exchange membranes for fuel cell applications. *International Journal of Hydrogen Energy*, *35*(17), 9349-9384.
7. Song, C., & Zhang, J. (2008). PEM fuel cell electrocatalysts and catalyst layers. *Fundamentals and applications. Springer, New York*, *89*.
8. Ganesan, A., Narayanasamy, M., Shunmugavel, K., & Chinnappa, I. J. (2016). Ultra low loading of anode catalyst for direct methanol fuel cells with ZrO2/pyrolysed (PANI-melamine) as catalyst support. *International Journal of Hydrogen Energy*, *41*(21), 8963-8977.
9. James, B. D., Spisak, A. B., & Colella, W. G. (2012). Manufacturing cost analysis of stationary fuel cell systems. *Strategic Analysis Inc. Arlington, VA*.
10. Venkataraman, R., Kunz, H. R., & Fenton, J. M. (2003). Development of new CO tolerant ternary anode catalysts for proton exchange membrane fuel cells. *Journal of the Electrochemical Society*, *150*(3), A278.
11. He, C., Kunz, H. R., & Fenton, J. M. (2003). Electro-oxidation of hydrogen with carbon monoxide on Pt/Ru-based ternary catalysts. *Journal of the Electrochemical Society*, *150*(8), A1017.
12. Liu, Y., Ishihara, A., Mitsushima, S., Kamiya, N., & Ota, K. I. (2007). Transition metal oxides as DMFC cathodes without platinum. *Journal of The Electrochemical Society*, *154*(7), B664.
13. Zhong, H., Zhang, H., Liang, Y., Zhang, J., Wang, M., & Wang, X. (2007). A novel non-noble electrocatalyst for oxygen reduction in proton exchange membrane fuel cells. *Journal of Power Sources*, *164*(2), 572-577.
14. Feng, Y., & Alonso-Vante, N. (2008). Nonprecious metal catalysts for the molecular oxygen-reduction reaction. *Physica Status Solidi (b)*, *245*(9), 1792-1806.
15. Millán, W. M., Thompson, T. T., Arriaga, L. G., & Smit, M. A. (2009). Characterization of composite materials of electroconductive polymer and cobalt as electrocatalysts for the oxygen reduction reaction. *International Journal of Hydrogen Energy*, *34*(2), 694-702.
16. Goswami, C., Hazarika, K. K., & Bharali, P. (2018). Transition metal oxide nanocatalysts for oxygen reduction reaction. *Materials Science for Energy Technologies*, *1*(2), 117-128.

17. Zhang, Z., Liu, J., Gu, J., Su, L., & Cheng, L. (2014). An overview of metal oxide materials as electrocatalysts and supports for polymer electrolyte fuel cells. *Energy & Environmental Science*, *7*(8), 2535-2558.
18. Hao, Z., Ma, Y., Chen, Y., Fu, P., & Wang, P. (2022). Non-Noble Metal Catalysts in Cathodic Oxygen Reduction Reaction of Proton Exchange Membrane Fuel Cells: Recent Advances. *Nanomaterials*, *12*(19), 3331.
19. Di Noto, V., Negro, E., Polizzi, S., Agresti, F., & Giffin, G. A. (2012). Synthesis–Structure–Morphology Interplay of Bimetallic "Core–Shell" Carbon Nitride Nano-electrocatalysts. *ChemSusChem*, *5*(12), 2451-2459.
20. Tauster, S. J., Fung, S. C., & Garten, R. L. (1978). Strong metal-support interactions. Group 8 noble metals supported on titanium dioxide. *Journal of the American Chemical Society*, *100*(1), 170-175.
21. Gustavsson, M., Ekström, H., Hanarp, P., Eurenius, L., Lindbergh, G., Olsson, E., & Kasemo, B. (2007). Thin film Pt/TiO2 catalysts for the polymer electrolyte fuel cell. *Journal of Power Sources*, *163*(2), 671-678.
22. Rajalakshmi, N., Lakshmi, N., & Dhathathreyan, K. S. (2008). Nano titanium oxide catalyst support for proton exchange membrane fuel cells. *International Journal of Hydrogen Energy*, *33*(24), 7521-7526.
23. Smith, J. R., Walsh, F. C., & Clarke, R. L. (1998). Electrodes based on Magnéli phase titanium oxides: the properties and applications of Ebonex® materials. *Journal of Applied Electrochemistry*, *28*(10), 1021-1033.
24. Ioroi, T., Senoh, H., Yamazaki, S. I., Siroma, Z., Fujiwara, N., & Yasuda, K. (2008). Stability of corrosion-resistant Magnéli-phase Ti4O7-supported PEMFC catalysts at high potentials. *Journal of the Electrochemical Society*, *155*(4), B321.
25. Zhang, L., Kim, J., Zhang, J., Nan, F., Gauquelin, N., Botton, G. A., ... & Knights, S. (2013). Ti4O7 supported Ru@ Pt core–shell catalyst for CO-tolerance in PEM fuel cell hydrogen oxidation reaction. *Applied Energy*, *103*, 507-513.
26. Chen, G., Bare, S. R., & Mallouk, T. E. (2002). Development of supported bifunctional electrocatalysts for unitized regenerative fuel cells. *Journal of the Electrochemical Society*, *149*(8), A1092.
27. Ho, V. T. T., Pan, C. J., Rick, J., Su, W. N., & Hwang, B. J. (2011). Nanostructured Ti0. 7Mo0. 3O2 support enhances electron transfer to Pt: high-performance catalyst for oxygen reduction reaction. *Journal of the American Chemical Society*, *133*(30), 11716-11724.
28. Selvarani, G., Maheswari, S., Sridhar, P., Pitchumani, S., & Shukla, A. K. (2009). Carbon-supported Pt–TiO2 as a methanol-tolerant oxygen-reduction catalyst for DMFCs. *Journal of the Electrochemical Society*, *156*(11), B1354.
29. Macak, J. M., Schmidt-Stein, F., & Schmuki, P. (2007). Efficient oxygen reduction on layers of ordered TiO_2 nanotubes loaded with Au nanoparticles. *Electrochemistry Communications*, *9*(7), 1783-1787.
30. Xu, J., Gao, P., & Zhao, T. S. (2012). Non-precious Co3O4 nano-rod electrocatalyst for oxygen reduction reaction in anion-exchange membrane fuel cells. *Energy & Environmental Science*, *5*(1), 5333-5339.
31. Wang, D., Yu, Y., He, H., Wang, J., Zhou, W., & Abruna, H. D. (2015). Template-free synthesis of hollow-structured Co3O4 nanoparticles as high-performance anodes for lithium-ion batteries. *ACS Nano*, *9*(2), 1775-1781.

32. Li, G. C., Hua, X. N., Liu, P. F., Xie, Y. X., & Han, L. (2015). Porous Co3O4 microflowers prepared by thermolysis of metal-organic framework for supercapacitor. *Materials Chemistry and Physics*, *168*, 127-131.
33. Xie, G., Chen, B., Jiang, Z., Niu, X., Cheng, S., Zhen, Z., ... & Jiang, Z. J. (2016). High catalytic activity of Co 3 O 4 nanoparticles encapsulated in a graphene supported carbon matrix for oxygen reduction reaction. *RSC Advances*, *6*(55), 50349-50357.
34. Liang, Y., Li, Y., Wang, H., Zhou, J., Wang, J., Regier, T., & Dai, H. (2011). Co3O4 nanocrystals on graphene as a synergistic catalyst for oxygen reduction reaction. *Nature Materials*, *10*(10), 780-786.
35. Ahmed, M. S., Choi, B., & Kim, Y. B. (2018). Development of highly active bifunctional electrocatalyst using Co3O4 on carbon nanotubes for oxygen reduction and oxygen evolution. *Scientific reports*, *8*(1), 1-10.
36. Zhou, R., Zheng, Y., Hulicova-Jurcakova, D., & Qiao, S. Z. (2013). Enhanced electrochemical catalytic activity by copper oxide grown on nitrogen-doped reduced graphene oxide. *Journal of Materials Chemistry A*, *1*(42), 13179-13185.
37. Song, J., Wang, W., Wang, F., Kang, Y., Liu, S., & Lei, Z. (2017). Encapsulated NdCuOx bimetallic nanoparticles with nitrogen doped carbon as an efficient electrocatalyst for oxygen reduction reaction. *Electrochimica Acta*, *258*, 1404-1412.
38. Yan, X. Y., Tong, X. L., Zhang, Y. F., Han, X. D., Wang, Y. Y., Jin, G. Q., ... & Guo, X. Y. (2012). Cuprous oxide nanoparticles dispersed on reduced graphene oxide as an efficient electrocatalyst for oxygen reduction reaction. *Chemical Communications*, *48*(13), 1892-1894.
39. Roche, I., Chaînet, E., Chatenet, M., & Vondrák, J. (2007). Carbon-supported manganese oxide nanoparticles as electrocatalysts for the oxygen reduction reaction (ORR) in alkaline medium: physical characterizations and ORR mechanism. *The Journal of Physical Chemistry C*, *111*(3), 1434-1443.
40. Dong, C., Liu, Z. W., Liu, J. Y., Wang, W. C., Cui, L., Luo, R. C., ... & Yang, J. (2017). Modest Oxygen-Defective Amorphous Manganese-Based Nanoparticle Mullite with Superior Overall Electrocatalytic Performance for Oxygen Reduction Reaction. *Small*, *13*(16), 1603903.
41. Cao, Y. L., Yang, H. X., Ai, X. P., & Xiao, L. F. (2003). The mechanism of oxygen reduction on MnO2-catalyzed air cathode in alkaline solution. *Journal of Electroanalytical Chemistry*, *557*, 127-134.
42. Stoerzinger, K. A., Risch, M., Han, B., & Shao-Horn, Y. (2015). Recent insights into manganese oxides in catalyzing oxygen reduction kinetics. *ACS Catalysis*, *5*(10), 6021-6031.
43. Dong, C., Liu, Z. W., Liu, J. Y., Wang, W. C., Cui, L., Luo, R. C., ... & Yang, J. (2017). Modest Oxygen-Defective Amorphous Manganese-Based Nanoparticle Mullite with Superior Overall Electrocatalytic Performance for Oxygen Reduction Reaction. *Small*, *13*(16), 1603903.
44. Hazarika, K. K., Goswami, C., Saikia, H., Borah, B. J., & Bharali, P. (2018). Cubic Mn2O3 nanoparticles on carbon as bifunctional electrocatalyst for oxygen reduction and oxygen evolution reactions. *Molecular Catalysis*, *451*, 153-160.
45. Trovarelli, A., De Leitenburg, C., Boaro, M., & Dolcetti, G. (1999). The utilization of ceria in industrial catalysis. *Catalysis Today*, *50*(2), 353-367.

46. Shao, Z., & Haile, S. M. (2004). A high-performance cathode for the next generation of solid-oxide fuel cells. *Nature*, *431*(7005), 170-173.
47. Karakoti, A. S., Singh, S., Kumar, A., Malinska, M., Kuchibhatla, S. V., Wozniak, K., ... & Seal, S. (2009). PEGylated nanoceria as radical scavenger with tunable redox chemistry. *Journal of the American Chemical Society*, *131*(40), 14144-14145.
48. Andreeva, D., Ivanov, I., Ilieva, L., Abrashev, M. V., Zanella, R., Sobczak, J. W., ... & Petrov, K. (2009). Gold catalysts supported on ceria doped by rare earth metals for water gas shift reaction: Influence of the preparation method. *Applied Catalysis A: General*, *357*(2), 159-169.
49. Gasperi, G., Brugnoli, L., Pedone, A., Menziani, M. C., Valeri, S., & Luches, P. (2019). Reducibility of Ag- and Cu-Modified Ultrathin Epitaxial Cerium Oxide Films. *The Journal of Physical Chemistry C*, *123*(22), 13702-13711.
50. Malavasi, L., Fisher, C. A., & Islam, M. S. (2010). Oxide-ion and proton conducting electrolyte materials for clean energy applications: structural and mechanistic features. *Chemical Society Reviews*, *39*(11), 4370-4387.
51. Skorodumova, N. V., Simak, S. I., Lundqvist, B. I., Abrikosov, I. A., & Johansson, B. (2002). Quantum origin of the oxygen storage capability of ceria. *Physical Review Letters*, *89*(16), 166601.
52. Luches, P., Pagliuca, F., & Valeri, S. (2014). Structural and morphological modifications of thermally reduced cerium oxide ultrathin epitaxial films on Pt (111). *Physical Chemistry Chemical Physics*, *16*(35), 18848-18857.
53. Mogensen, M., Sammes, N. M., & Tompsett, G. A. (2000). Physical, chemical and electrochemical properties of pure and doped ceria. *Solid State Ionics*, *129*(1-4), 63-94.
54. McFarland, E. W., & Metiu, H. (2013). Catalysis by doped oxides. *Chemical Reviews*, *113*(6), 4391-4427.
55. Yang, N., Orgiani, P., Di Bartolomeo, E., Foglietti, V., Torelli, P., Ievlev, A. V., ... & Aruta, C. (2017). Effects of dopant ionic radius on cerium reduction in epitaxial cerium oxide thin films. *The Journal of Physical Chemistry C*, *121*(16), 8841-8849.
56. Hu, Z., & Metiu, H. (2011). Effect of dopants on the energy of oxygen-vacancy formation at the surface of ceria: Local or global?. *The Journal of Physical Chemistry C*, *115*(36), 17898-17909.
57. Nolan, M. (2011). Enhanced oxygen vacancy formation in ceria (111) and (110) surfaces doped with divalent cations. *Journal of Materials Chemistry*, *21*(25), 9160-9168.
58. Fifere, N., Airinei, A., Dobromir, M., Sacarescu, L., & Dunca, S. I. (2021). Revealing the effect of synthesis conditions on the structural, optical, and antibacterial properties of cerium oxide nanoparticles. *Nanomaterials*, *11*(10), 2596.
59. Danilova, I. G., Slavinskaya, E. M., Zaikovskii, V. I., Ivanova, A. S., Boronin, A. I., Gulyaev, R. V., & Amosov, Y. I. (2010, February). Effect of preparation procedure on the properties of CeO2. In *Kinetics and Catalysis* (Vol. 51, No. 1, pp. 143-148). SP MAIK Nauka/Interperiodica.

60. Shirbhate, S., Yadav, A. K., Barman, S. R., & Acharya, S. (2021). Dopant Induced-Modulation in Reducing Ability of Cerium in Doped Ceria System and Its Effect on Oxy-Ion Conductivity: Core Study by XPS and XANES Probes. *ECS Journal of Solid State Science and Technology*, *10*(10), 101010.
61. Yang, Z., Woo, T. K., & Hermansson, K. (2006). Effects of Zr doping on stoichiometric and reduced ceria: A first-principles study. *The Journal of Chemical Physics*, *124*(22), 224704.
62. Yang, Z., Luo, G., Lu, Z., & Hermansson, K. (2007). Oxygen vacancy formation energy in Pd-doped ceria: A DFT+ U study. *The Journal of Chemical Physics*, *127*(7), 074704.
63. Righi, G., Benedetti, S., & Magri, R. (2022). Investigation of the structural and electronic differences between silver and copper doped ceria using the density functional theory. *Journal of Physics: Condensed Matter*, *34*(20), 204010.
64. Ye, X. F., Wang, S. R., Hu, Q., Chen, J. Y., Wen, T. L., & Wen, Z. Y. (2009). Improvement of Cu–CeO2 anodes for SOFCs running on ethanol fuels. *Solid State Ionics*, *180*(2-3), 276-281.
65. Yang, Z., He, B., Lu, Z., & Hermansson, K. (2010). Physisorbed, chemisorbed, and oxidized CO on highly active Cu− CeO2 (111). *The Journal of Physical Chemistry C*, *114*(10), 4486-4494.
66. Branda, M. M., Hernández, N. C., Sanz, J. F., & Illas, F. (2010). Density functional theory study of the interaction of Cu, Ag, and Au atoms with the regular CeO2 (111) surface. *The Journal of Physical Chemistry C*, *114*(4), 1934-1941.
67. James, T. E., Hemmingson, S. L., & Campbell, C. T. (2015). Energy of supported metal catalysts: from single atoms to large metal nanoparticles. *Acs Catalysis*, *5*(10), 5673-5678.
68. Li, G., Hu, S., Xu, Q., & Zhu, J. (2019). Interaction between Cu Nanoparticles and CeO2 (111) Film Surfaces. *The Journal of Physical Chemistry C*, *123*(38), 23563-23571.
69. Luches, P., Pagliuca, F., Valeri, S., Illas, F., Preda, G., & Pacchioni, G. (2012). Nature of Ag islands and nanoparticles on the CeO2 (111) surface. *The Journal of Physical Chemistry C*, *116*(1), 1122-1132.
70. Megginson, R., Grillo, F., Francis, S. M., Paes, V. Z. C., Trombini, H., Grande, P. L., ... & Baddeley, C. J. (2022). Thermal behaviour of Cu and Au nanoparticles grown on CeO2 thin films. *Applied Surface Science*, *575*, 151656.
71. García-Melchor, M., & Lopez, N. (2014). Homolytic products from heterolytic paths in H2 dissociation on metal oxides: the example of CeO2. *The Journal of Physical Chemistry C*, *118*(20), 10921-10926.
72. T., Bonura, G., Chiodo, V., Freni, S., Couzinié, J. P., Bourgon, J., ... & Cassir, M. (2013). Surface-dependent oxidation of H2 on CeO2 surfaces. *Journal of Catalysis*, *297*, 193-201.
73. Perrichon, V., Laachir, A., Bergeret, G., Fréty, R., Tournayan, L., & Touret, O. (1994). Reduction of cerias with different textures by hydrogen and their reoxidation by oxygen. *Journal of the Chemical Society, Faraday Transactions*, *90*(5), 773-781.
74. Xu, J., & Overbury, S. H. (2004). H2 reduction of CeO2 (111) surfaces via boundary Rh□ O mediation. *Journal of Catalysis*, *222*(1), 167-173.
75. Kammert, J., Moon, J., & Wu, Z. (2020). A review of the interactions between ceria and H2 and the applications to selective hydrogenation of alkynes. *Chinese Journal of Catalysis*, *41*(6), 901-914

76. Aneggi, E., Boaro, M., de Leitenburg, C., Dolcetti, G., & Trovarelli, A. (2006). Insights into the redox properties of ceria-based oxides and their implications in catalysis. *Journal of Alloys and Compounds*, *408*, 1096-1102.
77. Lykhach, Y., Figueroba, A., Camellone, M. F., Neitzel, A., Skála, T., Negreiros, F. R., ... & Libuda, J. (2016). Reactivity of atomically dispersed Pt 2+ species towards H 2: model Pt–CeO 2 fuel cell catalyst. *Physical Chemistry Chemical Physics*, *18*(11), 7672-7679.
78. Righi, G., Magri, R., & Selloni, A. (2019). H2 dissociation on noble metal single atom catalysts adsorbed on and doped into CeO2 (111). *The Journal of Physical Chemistry C*, *123*(15), 9875-9883.
79. Benedetti, S., Righi, G., Luches, P., D'Addato, S., Magri, R., & Selloni, A. (2020). Surface reactivity of Ag-modified ceria to hydrogen: a combined experimental and theoretical investigation. *ACS Applied Materials & Interfaces*, *12*(24), 27682-27690.
80. Wang, X., Rodriguez, J. A., Hanson, J. C., Gamarra, D., Martínez-Arias, A., & Fernández-García, M. (2005). Unusual Physical and Chemical Properties of Cu in Ce1-x Cu x O2 Oxides. *The Journal of Physical Chemistry B*, *109*(42), 19595-19603.
81. García-Vargas, C. E., Collinge, G., Yun, D., Lee, M. S., Muravev, V., Su, Y. Q., ... & Wang, Y. (2022). Activation of Lattice and Adatom Oxygen by Highly Stable Ceria-Supported Cu Single Atoms. *ACS Catalysis*, *12*(21), 13649-13662.
82. Lykaki, M., Stefa, S., Carabineiro, S. A., Pandis, P. K., Stathopoulos, V. N., & Konsolakis, M. (2019). Facet-dependent reactivity of Fe2O3/CeO2 nanocomposites: effect of ceria morphology on CO oxidation. *Catalysts*, *9*(4), 371.
83. Wang, W. C., Chen, S. Y., Glans, P. A., Guo, J., Chen, R. J., Fong, K. W., ... & Dong, C. L. (2013). Towards understanding the electronic structure of Fe-doped CeO 2 nanoparticles with X-ray spectroscopy. *Physical Chemistry Chemical Physics*, *15*(35), 14701-14707.
84. Channei, D., Nakaruk, A., Phanichphant, S., Koshy, P., & Sorrell, C. C. (2016). Effect of iron doping on the structural and optical properties of CeO2 films. *Journal of Sol-Gel Science and Technology*, *79*(1), 51-58.
85. Singh, P., & Hegde, M. S. (2008). Controlled synthesis of nanocrystalline CeO2 and Ce1− xMxO2− δ (M= Zr, Y, Ti, Pr and Fe) solid solutions by the hydrothermal method: structure and oxygen storage capacity. *Journal of Solid State Chemistry*, *181*(12), 3248-3256.

Chapter 2

Experimental apparatus and investigation techniques

The main purpose of the present thesis is to perform a systematic study on the interaction between Cu-modified CeO_2 ultrathin films with H_2 during thermal annealing treatments. The ultrathin films (Cu-doped CeO_2 and Cu NPs/CeO_2) studied in this thesis are used as a model system to understand the interaction with H_2 at atomic scale. These model systems have characteristic features such as well-controlled morphology, chemical and structural properties, so they help us to understand the influence of individual variables such as thickness or dopant concentration on the modifications induced on the system, unlike complex real systems.

The main part of the results presented in the next chapters have been obtained at the SESAMo (Ragno-1) laboratory led by Dr Paola Luches, a joint laboratory of the University of Modena and Reggio Emilia, and the Nanoscience Institute of the National Research Council, in Modena. In this chapter, I will introduce the sample preparation and characterization methods employed in the SESAMo laboratory together with their theoretical description. Then, I will describe the NFFA APE-HE beamline experimental apparatus at Elettra synchrotron radiation facility, Trieste, where we performed NEXAFS experiments in collaboration with the group led by Dr. Piero Torelli. I will also briefly describe the theoretical aspects behind this kind of absorption spectroscopy that we exploited to study our samples.

2.1 SESAMo Laboratory

All the samples that I have described in the next chapters were prepared at the SESAMo laboratory. In figure1, the sketch and the real experimental set-up in the Ragno-1 of the SESAMo laboratory are shown. It basically consists of three ultra-high vacuum chambers connected to each other with transfer drivers that help us to perform the in-situ characterization of the samples after growth with background pressure in low 10^{-10} mbar. The first chamber is the growth chamber which is equipped with MBE evaporation sources for the reactive growth of ultrathin films and nanostructures. The second chamber is customized for the substrate preparation and sample characterization techniques such as X-ray photoelectron spectroscopy (XPS), Auger electron spectroscopy (AES) and low-energy electron diffraction (LEED). Finally, the third chamber hosts the RT scanning tunnelling microscope (STM), where the surface morphology characterization was done.

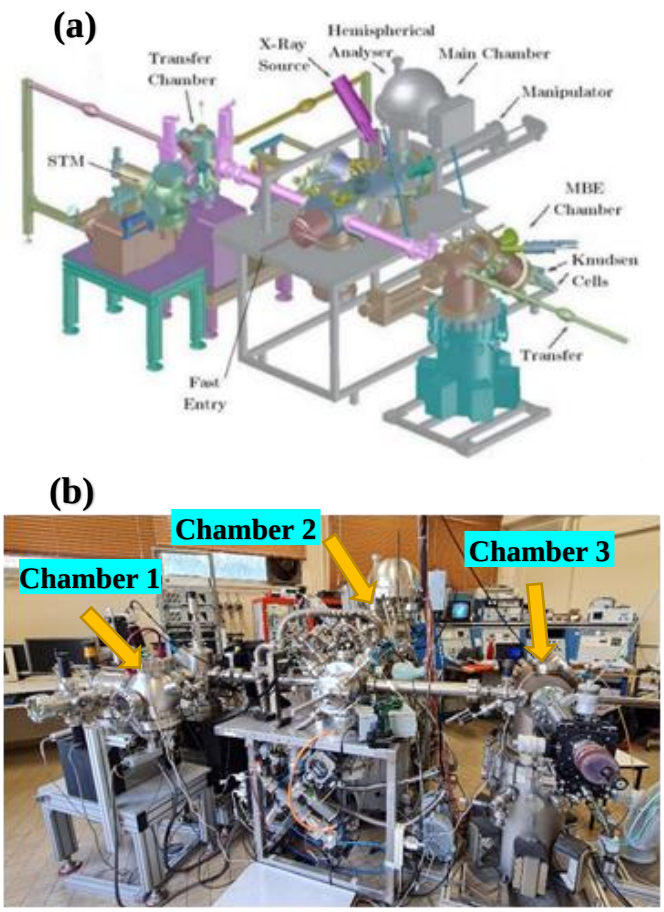

The substrates can be introduced into the chamber 2, which is also referred as main chamber, without affecting the vacuum inside with the help of a load-lock system. This chamber is pumped by an ion pump and a system of interconnected turbo molecular and a scroll pump. Manipulator movements of this chamber, which are driven by stepping motors, are operated with the help of a computer for precise movements in all 3 (x, y, and z) directions and two rotation angles. The allowed rotations are around the manipulator axis (θ) and around the normal to the sample surface (ϕ). The manipulator can be heated up to 1200 K for the temperature treatment process of the samples in UHV and gas (H_2 and O_2) environment.

Figure 1: (a) Sketch [1] and photo (b) of the experimental apparatus in the Ragno-1 (SESAMo) laboratory, Modena.

Two gas lines are connected to the chamber 2 for the flow of O_2 and H_2 gases. Leak valves help to regulate with high precision the pressure of the gases entering the chamber. The gas lines are flushed, i.e., filled, pumped with a scroll pump and re-filled, before performing the experiments.

Chamber 3 shown in the figure is the growth chamber, it consists of five Knudsen cells for evaporation of metals plus one e-beam evaporator. Each cell is equipped with a shutter which can be mechanically operated to start and stop the material deposition. The effusion cells consist of a crucible usually made of pyrolytic boron nitride or refractory metal, which contains the material to be evaporated, and a heating source. Either ohmic heating or electron beam heating methods are typically used to evaporate the source material. In ohmic heating method, the heat is generated form the filament wound around the crucible, whereas in electron beam heating, the electrons generated by thermionic emission are accelerated by a potential of a few kV toward the metallic crucible, inducing heating in the material [2]. The e-beam evaporation source was used for the evaporation of cerium atoms due to the higher evaporation temperature required, while an

effusion cell was used for Cu metal evaporation. The chamber also hosts a water-cooled quartz microbalance, used to evaluate the evaporation rate. An ion pump keeps the chamber in a pressure of $5x10^{-10}$ mbar. An Omicron scanning tunneling microscope (STM) in chamber 3 was employed to study the surface morphology of the samples at RT. The instrument is operated in constant current mode, applying a bias to the sample with respect to a grounded tungsten tip. The typical pressure in the chamber 3 is p=5 x 10^{-10} mbar and it is kept by means of an ion pump.

2.1.1 Sample growth and treatments

For the growth of ultrathin-films of Cu-modified CeO_2, a Pt (111) single crystal was employed as substrate. Before the deposition of the ultrathin films, the substrate was prepared in the main chamber by repeated cycles of Ar^+ sputtering (1 keV, 1 μA) and annealing (1040 K) in UHV to remove the contaminants on the surface below the sensitivity level of XPS. After the cleaning procedure, the substrate is transferred to the growth chamber and is placed in the deposition position in front of the evaporation cells with the help of a manipulator with five degrees of freedom. Samples were prepared by keeping the substrate at RT, co-deposition method was employed for the Cu-doped CeO_2 in O_2 partial pressure (1 x 10^{-7} mbar) but Cu NPs/ CeO_2 films were prepared by sequential deposition, where the CeO_2 film was prepared and oxidized first and then Cu NPs were deposited on top of it.

After the preparation, the samples are transferred to the main chamber for the oxidation and further thermal annealing treatments. The oxidation process is performed by annealing the samples at 770 K for 45 minutes in O_2 partial pressure (1 x 10^{-7} mbar). Thermal annealing of the samples was performed at 4 different temperatures (470, 570, 670 and 770 K) in-situ for 15 minutes each in both UHV and in H_2. After each thermal step, X-ray photoelectron spectroscopy (XPS) was used to investigate the chemical properties of the samples. Samples were transferred to chamber 3 for the characterization of the surface morphology of the samples before and after reduction cycles using STM at RT.

2.2 X-ray Photoelectron spectroscopy

XPS has been the main characterization technique used in this work to extract the elemental composition and chemical state of the elements in the samples. A twin anode (Mg-Al) X-ray source and a concentric hemispherical electron analyzer with seven channel electron multipliers are used.

XPS is a surface sensitive electron spectroscopic technique developed by Kai Siebahn and his co-workers around mid-1960s [3].

The following procedure is exploited in XPS:

- X-rays of characteristic photon energy are produced by bombardment with high energy electrons of Mg/Al coated anode material.
- Mg K_α (1253.6 eV) and Al K_α (1486.6 eV) are used as emission lines due to their sufficient energy and narrow energy width which helps to easily access the core-levels.
- The sample surface is irradiated with a beam of monoenergetic x-rays.
- Due to the interaction with the X-ray photons, the core electrons gain energy, they are emitted from the core levels and reach the vacuum with a specific kinetic energy E_k (figure 2) given by:

$$\mathbf{E_k = h\nu - E_B - \Phi_0} \quad (2.1)$$

where hν is the photon energy, E_B is the binding energy of the core electrons measured with respect to Fermi level and Φ_0 is the analyzer work function.

- A typical XPS spectrum gives the number of ejected photoelectrons by the material per energy interval vs their kinetic or binding energy.

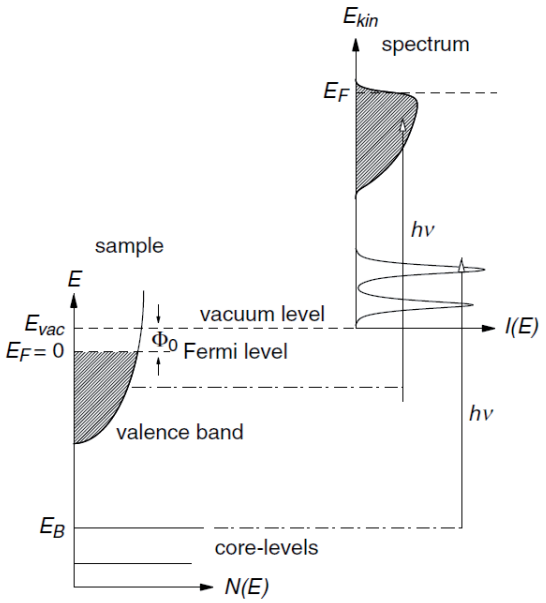

Figure 2: A schematic representation of XPS process in a single particle assumption. Electrons with a binding energy E_B from the core level can be excited to the vacuum level E_{vac} by photons with energy greater than $E_B + \Phi_0$. [4].

Core electrons with binding energy E_B can be excited above vacuum level by photons with energy $h\nu > E_B + \Phi_0$. Typically, the number of photoelectrons collected at a given photon energy is a function of the inelastic mean free path (λ), which is the average distance travelled by photoelectrons in a solid without change in their kinetic energy. Mean free path depends strongly on the energy of the photoelectrons, which in turn depends on the photon energy. Photoelectrons can suffer from both elastic and inelastic collisions.

The loss in kinetic energy of the photoelectrons due to inelastic collisions induces a broad background in the XPS spectrum.

XPS with conventional laboratory sources is a surface sensitive technique, since, due to the photon energies used (Mg K_α -1253.6 eV and Al K_α -1486.6 eV), the kinetic energy of the emitted photoelectrons is relatively low. In fact, the escape depth of the emitted electrons with K.E in between 10-1000 eV varies between 5-30 Å [4], making this technique surface sensitive as only few atomic layers are probed. As the binding energies of core levels are different for each element, XPS acts as fingerprint for each element and makes this tool a useful analytical technique for the detection of each element except hydrogen and helium [4,5].In addition to elemental analysis, XPS is able to monitor changes in the chemical environment / bonding state of the atom, which modify the binding energy, width and shape of the core level peaks. This change in the binding energy (E_B) compared to the one of the pure elements is called "chemical shift". Chemical shifts can arise because of several reasons such as screening effects, relaxation effects and effective chemical potential difference [6]. Usually, the electrons in the core levels of an atom with positive oxidation state display a higher binding energy, due to increase in the Coulomb interaction with the ion core, caused by the chemical bond. A quantitative analysis of elemental composition and concentration of elements on the surface of the samples can be done considering the intensity of photoelectrons acquired. In the photoemission process from the inner subshells (p, d, f, etc.,), the spectral lines are split into two components as shown in figure 3 [6].

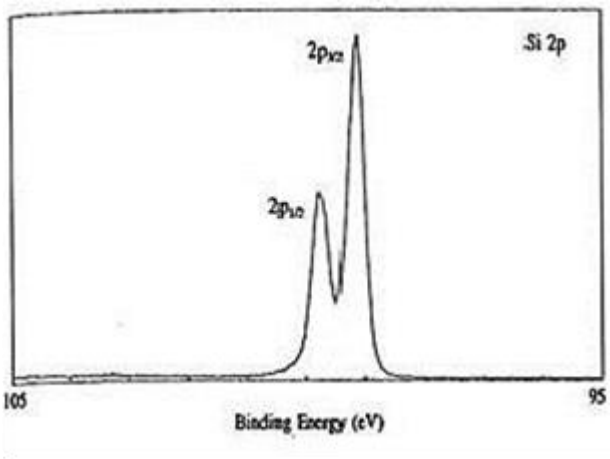

Figure 3: Spin-orbit splitting of a photoemission spectra of Si 2p, adapted from [6].

The splitting of the spectral lines arises from the spin-orbit coupling effect from the final state after photoemission process. Inner subshells in the initial state are completely filled but an unpaired spin is left in the final state an electron is removed due to the photoemission process. So, there will be a coupling

between the unpaired spin and orbital angular momentum if the core hole belongs to an orbital with non-zero orbital angular momentum giving rise to two non-degenerate ($j_+ = \ell + ½$ and $j_- = \ell - ½$) states and a spin-orbit doublet is observed in the photoemission process [7,8]. However, in some cases the spectrum acquired can be far more complex than a mere doublet, such as for example in the case of Ce 3d (figure 4). The Ce 3d spectrum of a pure CeO_2 sample has the two spin-orbit components (Ce $3d_{3/2}$ and Ce $3d_{5/2}$) which are further divided by final state effects into six components as shown in figure 4.

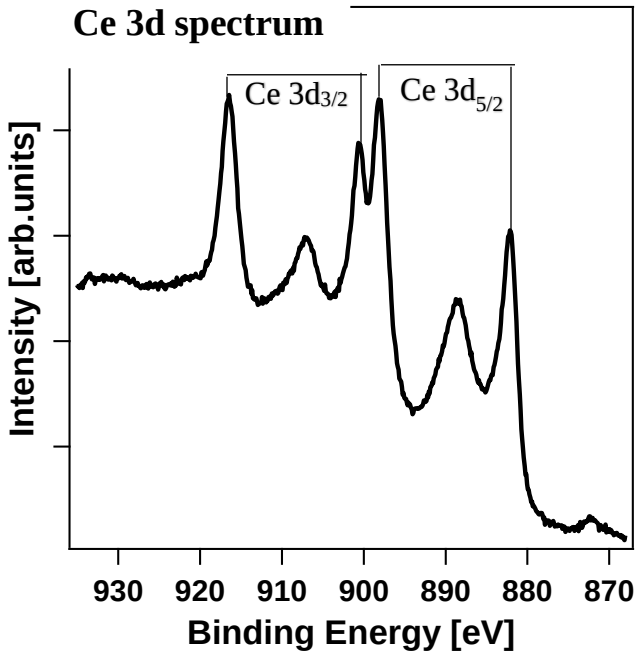

Figure 4: Ce 3d spectrum of a pure CeO_2 with spin orbit splitting (Ce $3d_{3/2}$ and Ce $3d_{5/2}$).

In this work, XPS was extensively used to determine the electronic structure of the ultrathin films and its change in different environments. Specifically, XPS helped us to investigate the evolution of the concentration of Ce^{3+} ions during thermal treatments which is mandatory for this work. Ce 3d spectral line shape analysis with the procedure by Skala et al. [9] provided us the information regarding the electronic configuration and oxidation state of Ce ions. Copper oxidation state analysis with Cu 2p XPS spectra were quite difficult. The complexity of Cu 2p spectrum arises from the overlapping binding energies of Cu_2O and Cu metal and CuO shakeup structures. Also, the low concentration of Cu atoms in our samples made the quantification of the oxidation state harder. So, we have performed NEXAFS experiments at APE-HE beamline, Trieste to extract more information on the Cu oxidation state during the treatments. The detailed explanation of the experimental and theoretical aspects are discussed in the following sections.

2.3 Scanning tunneling microscopy

All the surface morphology measurements that are presented in the next chapters were performed at SESAMo laboratory, Modena under UHV conditions at RT. Scanning tunneling microscope (STM) is a surface characterization method used for nanometer scale real space imaging of the surfaces. STM was developed by G. Binning and H. Rohrer in the beginning of 1980s [10] and earned them the Nobel prize for physics in 1986. STM works on the principle of quantum tunneling of electrons between two electrodes separated by a potential barrier which is classically forbidden. STM has a resolution of few Angstroms in the lateral directions and below an Angstrom in the direction perpendicular to the surface [11]. After the invention, STM experienced a revolutionary development which has helped the scientific community to investigate nanostructures at the atomic scale. A conductive tip scanned across a surface at small distances produces a topographic image of atomic resolution. Due to the continuous improvements and development of new type of STMs, the range of phenomena studied are also growing. STM can be used to measure the surface topography, local electronic properties, magnetic [12], optical [13], strength of atom/molecule bonds adsorbed on the surface etc.

A basic experimental set up sketch of a STM is shown in figure 5 (a). It consists of a sharp metallic tip, which is made of tungsten in our case, guided with the help of 3-dimensional piezoelectric scanner. The tip can be moved laterally in x and y-direction and vertically in z-direction with sub-Angstrom precision with the scanner. STM has two operational modes: constant current mode and constant height mode. In constant current mode, the feedback loop acts on the distance between the tip and the sample to keep the tunneling current constant. In constant height mode the distance between tip and the sample is kept constant and the tunneling current is measured. A bias voltage V is applied between the conducting tip and the sample. Due to the applied bias, electrons quantum-mechanically tunnel between the tip and the sample via vacuum gap as shown in figure 5(b). The tip is usually kept at few Angstroms from the sample surface. In our experiments we have used the constant current mode with bias voltage between 0.5-3.3 V and feedback current from 0.03-0.1 nA.

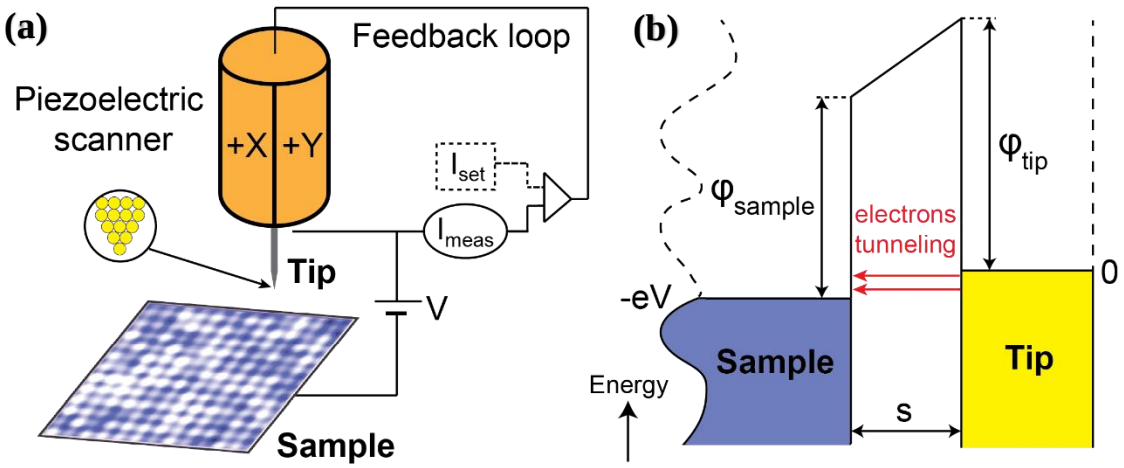

Figure 5: Schematic representation of STM (a), sketch of the energy levels of the tip and the sample, in the case of a positive bias applied to the sample, resulting in the tunneling of electrons across the barrier of width S (b) [14].

When a positive bias is applied to the sample with respect to the tip, electrons from the occupied states of the tip tunnel into the empty states of sample due to the alignment of the Fermi energy levels. The measured tunneling current depends on the local density of states (LDOS) of the sample and the separation distance between the tip and the sample.

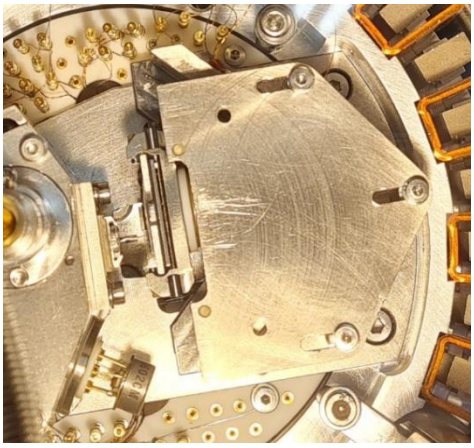

Figure 6: STM apparatus in the SESAMo laboratory, Modena.

Usually, the tip is raster-scanned across the sample surface, the tunneling current measured during the scan is displayed in the form of a two-dimensional image. The tip shape plays a huge role in the measured current and thus the image resolution. The contrast in STM images displayed depends not only on the surface morphology but also on the local electronic structure (material, defects). Depending on the applied bias,

structures made of different materials can result as protrusions in the images. Due to the above-mentioned effects, the interpretation of STM data can be non-trivial [15].

2.4 NEXAFS

2.4.1 X-ray absorption spectroscopy

Synchrotron based x-ray absorption spectroscopy (XAS) has become a key method for investigating the structure and the composition of heterogeneous catalysts. This method helps to disclose the nature of the active sites and also establishes a connection between structural motifs in a catalyst, internal electronic structure and catalytic properties [16]. XAS plays a prominent role in the catalyst research, because of its unique ability to provide the diverse information about the single element (active sites) specifically in a multielement system. Moreover, this method provides an expansive amount of information about the physical and chemical properties of the sample. Wide range of ordered, disordered and nanostructured materials [17,18] have been studied exploiting this method. Soft X-rays (100 eV - 3 KeV) and hard X-rays (> 3 keV) can interact effectively with most of the core electrons in materials. When the x-ray radiation is absorbed by a core electron, it undergoes an electronic transition from the core level to an empty orbital, leaving behind a core-hole. This absorption process strongly depends on the local environment of the atom, due to the strong localization of the core-electrons. Owing to the unique capabilities, XAS can provide vast information regarding the local and geometrical environment of the atom where the hole is created.

Absorption of the electromagnetic radiation is described by the Beer-Lambert law, which states that, when an electromagnetic radiation of intensity I_0 is absorbed by a sample of thickness d, the transmitted intensity (I_T) decreases exponentially as the thickness of the sample increases:

$$\mathbf{I_T = I_0\, e^{-\mu d}} \tag{2.2}$$

where μ is the linear absorption coefficient, which strongly depends on the energy E of the incident photon. The linear absorption coefficient (μ) in the X-ray range energy (E) for a monatomic material shows a dependency on the density of the material (ρ), on the atomic number Z, and on the relative atomic mass A as in the empirical relation below [19]:

$$\mathbf{\mu(E) \sim \rho Z^4 / AE^3} \tag{2.3}$$

However, if the energy of the incident photon matches the binding energy of the core level, a sharp increment in the absorption (absorption edges) is observed. X-ray absorption spectroscopy is the measurement of the x-ray absorption coefficient of the material which depends on the photon energy (excitation energy). The XAS spectrum can be roughly divided into two energy regions: Near Edge X-ray Absorption Fine structure (NEXAFS) also referred as X-ray Absorption Near Edge Structure (XANES) and

Extended X-ray Absorption Fine Structure (EXAFS) as shown in figure 7. NEXAFS and EXAFS provide different information regarding the element and its environment as the physics behind those processes are different [20]. NEXAFS is very sensitive to the density of electronic states near Fermi level, and it provides the information about the chemical state of the absorbing atoms, chemical bonding and internal symmetry [21]. Whereas EXAFS extends a few thousands eV above the absorption edge energy, and it is sensitive to the spatial ordering of nearest neighboring atoms around the absorbing atom [22,23].

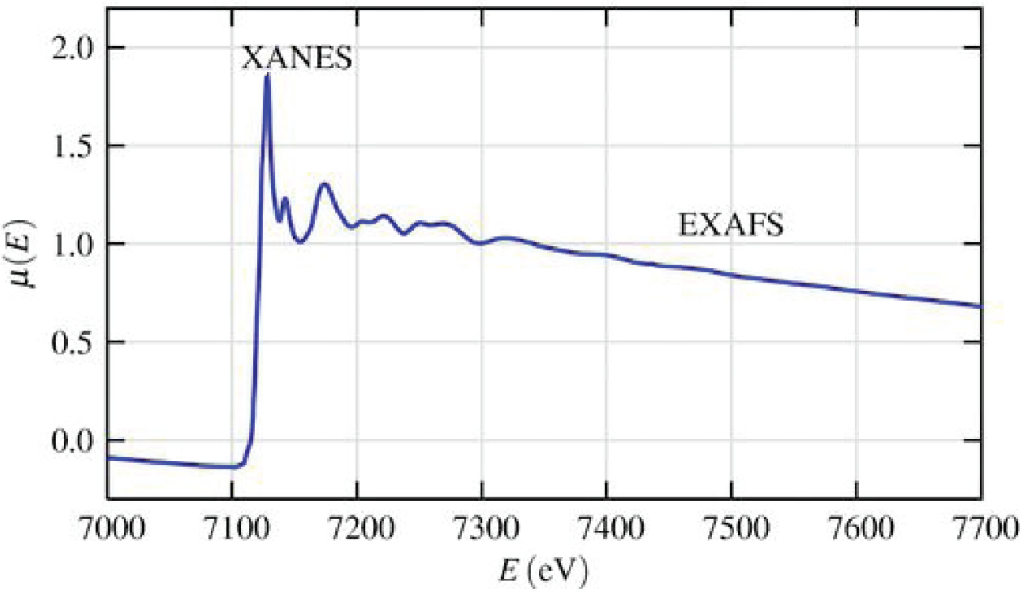

Figure 7: X-ray absorption spectrum of FeO with NEXAFS (XANES) and EXAFS regions, adapted from [19].

The absorption of the X-rays by the absorbing atom is described by the Fermi's Golden Rule which is given by:

$$\mu(E) \approx \sum_f \left|\langle f|\hat{T}|i\rangle\right|^2 \delta(\varepsilon_f - \varepsilon_i - E) \tag{2.4}$$

where |i⟩ is the ground (initial) state and |f⟩ is the final state of the absorbing atom. Summation is carried out all over the all the available final states. This corresponds to one photoelectron excited from initial state to higher energy level and all other electrons in atom which are rearranged due to the presence of positive holes in the core level. Higher energy levels may be localized or delocalized. The delta function describes the conservation of the energy of the system. $\hat{T}$ operator represents the interaction of the electron with the incident photon. So, the intensity and shape of the NEXAFS features are affected by the density of unoccupied (localized and delocalized) states. Onset transitions from core level to delocalized continuum

states reflect the position of the absorption edge and the feature in the region below the main absorption edge is due to the transitions to dipole forbidden states. The resolution of the NEXAFS features depends highly on the absorption edge energy.

XAS measurements can be performed using three main acquisition modes:1) Transmission, 2) Fluorescence and 3) Electron yield mode. The most frequently used mode is transmission mode, where the intensity of the beam before and after sample are used to determine the absorption coefficient using Lambert Beer equation. Generally, this mode is used with hard x-ray sources. This mode is not really suitable for catalysts as it is not surface sensitive. In the fluorescence yield mode (FY), the fluorescence photons are measured with a photon detector. The third mode is electron yield (EY), where the emitted electrons are measured. It is further divided into partial electron yield (PEY) and total electron yield (TEY). In PEY, electrons are collected only in a certain (selected) energy window. In TEY mode, primary, Auger and secondary electrons are collected. Auger and fluorescence are competitive decay processes. Auger decay is dominant for core-levels with binding energies values Eb < 1 keV. In both FY and EY, the emission intensity is often considered proportional to the absorption coefficient. TEY is a surface sensitive method due to the short mean free path of the electrons.

2.4.2 NFFA APE-HE experimental beamline facility, Trieste

APE stands for advanced photoelectric effect and HE for high energy. The photons emitted from the storage ring (section number 9) at Elettra synchrotron are emitted simultaneously by two-collinear insertion devices and then are delivered to two independent branches (HE and LE) as shown in figure 8.

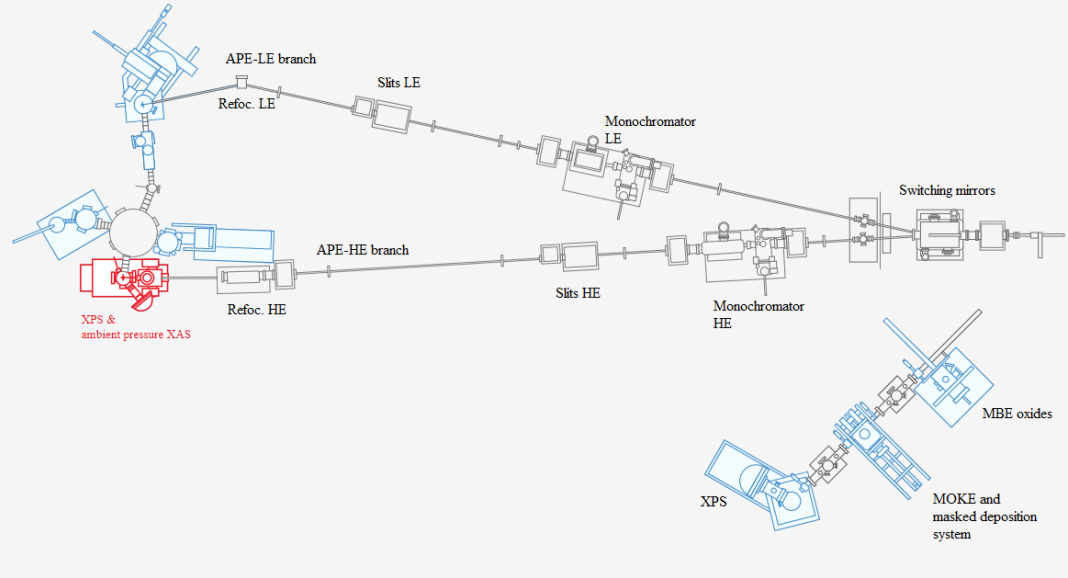

Figure 8: Graphical representation of experimental facilities at APE beamline, Elettra Trieste.

An APPLE-II type undulator is employed in APE-HE branch which is made of 36 periods of 2.16 cm each. It can polarize the photon flux both linearly and circularly. By tuning the vertical gap and the longitudinal phase between top and bottom magnetic arrays the polarization can be tuned. APE-HE provides photon energies ranging from 140-1500 eV, obtained using plane grating monochromators, and it is specifically devoted to the core-level spectroscopies, such as XAS, XPS and XMCD.

2.4.3 Reaction cell

For in operando NEXAFS studies, a reaction cell is placed at the end of the APE-HE beamline. The cell used for the present experiment was a prototype model which was developed in 2018 [24], which allows to perform XAS in ambient pressure. The ambient pressure absorption experimental set-up is fully compatible with the UHV environment of the synchrotron radiation facility, thanks to Si_3N_4 ultrathin membranes. These membranes function as a seal for the atmospheric pressure in the sample chamber, keeping the UHV system safe and act as windows for the passage of X-ray beam on to the sample in the reaction cell for XAS. NEXAFS detection is performed in total electron yield (TEY) mode by measuring the drain current from the sample.

The scheme of the reaction cell chamber where the NEXAFS at ambient pressure was performed is shown in figure 9 [24]. The reaction cell is placed inside the reaction chamber coaxially with the X-ray beam. It is mounted on an x-y table, and it can be moved in the plane perpendicular to the incident photon beam. This movement helps to align the sample surface in the focal point of the incident beam. The beam spot size depends on the photon energy, polarization, and entry slit aperture. The beam spot size can be can adjusted down to less than 100 μm in diameter with the help of double slit system positioned at the entry of the end station. Two UHV valves namely v1 and v2 (figure 9) are devoted to separate the vacuum of the reaction chamber from the beamline. The v1 gate valve is used to keep the vacuum of the beamline, while the reaction chamber (HE) is vented. Whereas v2 gate valve consists of an X-ray window (figure 9 c), made of an array of 4×4 Si_3N_4 membranes, each of the size 1mm × 1mm and 50 nm thickness, inserted in a supporting frame (10nm × 10nm size and 200 μm thick). Si_3N_4 membranes are used due to their good transmission capacity of X-rays (see figure 9 c) and good resistance to differential pressure between the experimental ($p \approx 1 \times 10^{-5}$ mbar) and the UHV beamline section. Valve v1 is closed during the venting process of the reaction chamber, for the insertion of the reaction cell and it is kept open during the measurements while valve v2 is closed. Thus, the valve system configuration (v1 and v2) makes the replacement of samples in the reaction cell quite fast (tens of minutes).

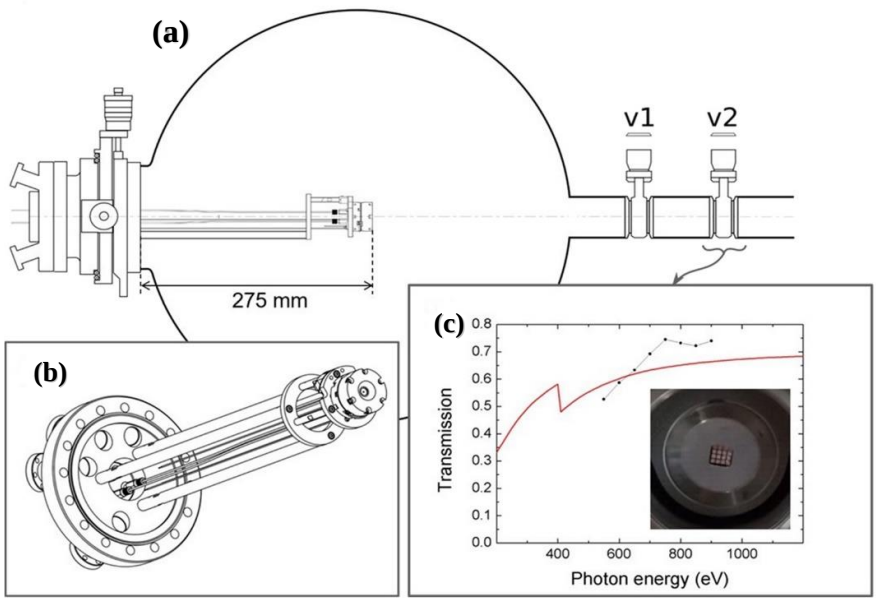

Figure 9: Schematic representation of the reactor cell inserted in the UHV chamber of the APE-HE beamline (a). sketch of the reactor cell (b) and, estimated (red curve) and measured transmission (black dots) of the X-ray window mounted on valve 2. Image is adapted from reference 24.

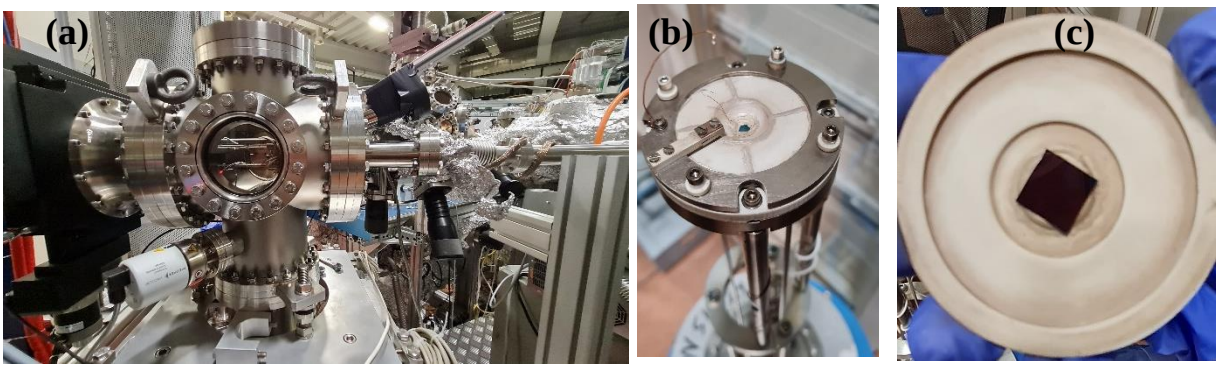

Figure 10: Photo of the experimental setup of the ambient pressure NEXAFS chamber (a), reaction cell (b) and, the Si_3N_4 membrane.

Valve v2 also acts as a protecting or safety valve during unwanted scenarios, such as leak from the membrane cell, thus protecting the UHV of the beamline. The main body of the reactor cell (figure 11) consists of a cylinder with a sample holder both made of aluminum, 4 cylindrical holes for gas inlets and an electrical contact for the collection of the total yield signal (drain current).

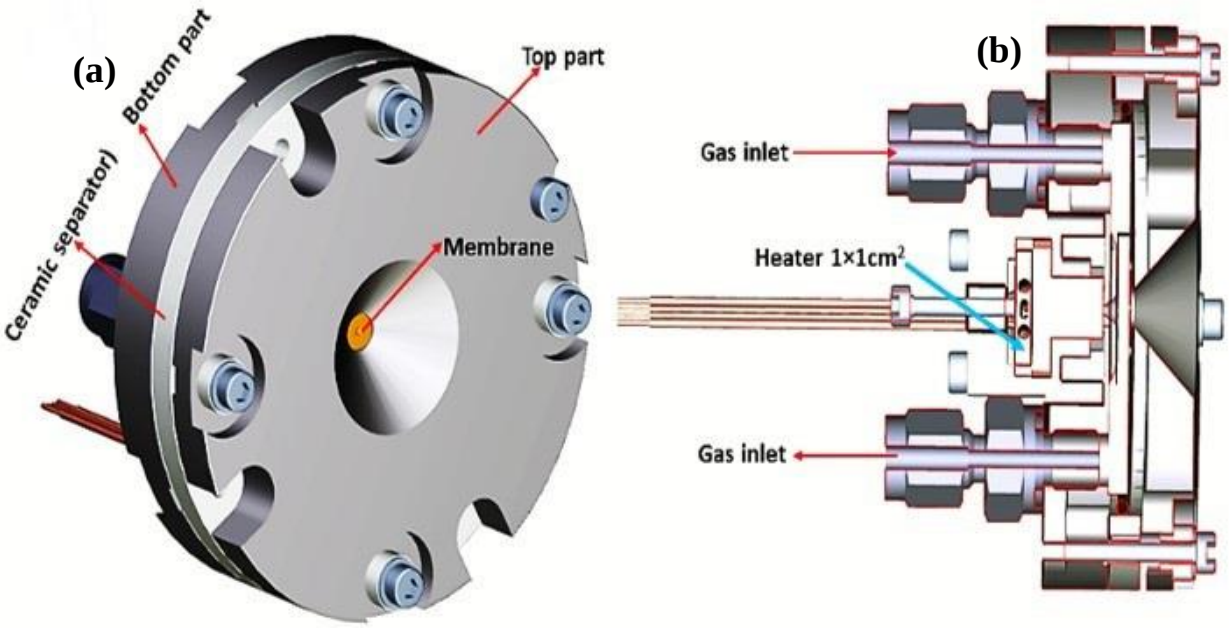

Figure 11: 3-D sketch of the reaction cell, front view (a) and vertical section (b).

In figure 11, the geometry of the reaction (front and sideview) is shown. The top part of the cell is made of polyether ether ketone (PEEK). PEEK is chemically inert and compatible with UHV condition. A Si_3N_4 membrane (500 µm × 500 µm in size and 100 nm thick) is glued in the center of the top PEEK case. Silver conductive paste is used as a glue for better electrical conduction and easy removal of the membrane when needed. Membrane X-ray transmission ranges between 40 to 80% in the soft X-rays.

Between top and bottom part of the cell, a molybdenum or Kapton spacer is positioned to separate the sample from the membrane. Due to this geometry, a space is created between top and bottom part where the catalytic reactions take place. A heater is placed below the sample, as shown in figure 11 (b), to control the temperature of the sample from RT-670 K. But the maximum temperature reached in our experiments was 620 K, due to the limitation of Viton O-rings sealing used between membrane and the sample.

The reactant gases enter through the gas inlet and the products formed after the reaction with the sample exit through the gas outlet conduct. The X-Ray beam passes through the Si_3N_4 membrane and the gas layer and hits the sample surface. As the radiation hits the sample, it is absorbed, and emission of secondary electrons occurs. The secondary electron current is proportional to the photo-absorption rate. A measure of the electric current flowing from ground to the membrane monitors the secondary electron leaving the sample (Total Electron Yield, TEY), so the absorption rate can be indirectly measured. Two electrical contacts allow the TEY measurements: the first electrical contact is placed on the membrane, and it applies a voltage bias between sample and membrane. The applied bias drives the emitted electrons during the

reactions on the sample to the membrane. The second electrical contact is connected to the sample and is used to measure the drain current to collect the TEY signal. TEY mode is made possible as the sample and membrane are electrically isolated. So, the measured current intensity (in the pA range) originates from the photoelectron emission process. The sample drain current is measured through a Keithley 6514 picoammeter.

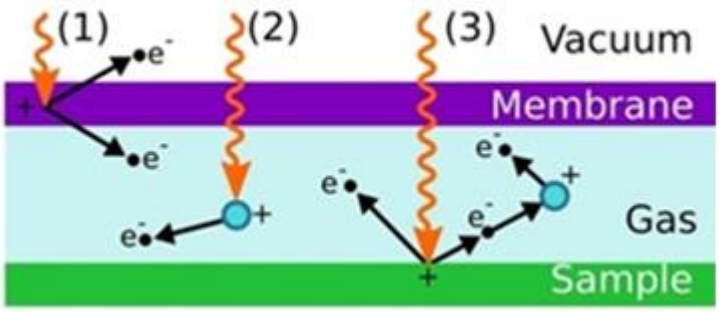

Figure 12: Scheme of all electron and ion yield channels created by photons hitting the (1) membrane, (2) gas, and (3) sample. Image is taken from ref 15.

In figure 12, a representation of the of the different sources of the electrons generated in the experiments are shown. Membrane emits its own TEY signal both in vacuum (front surface) and in the reactor cell (back surface). Electrons emitted in the reactor cell travel through the gas in the cell and collide gas molecules and finally reach the sample. The X-ray beam absorbed by the gas molecules also creates photoelectrons and thus ionized molecules. These generated electrons and ions can finally collide with the sample surface and modify the effective drain current measured from the surface [24]. So, the total drain current measured from the sample is the sum of TEY current from the sample and currents originating from the membrane, from the electrons from the gas, and from the positive ion current and it is expressed by the following equation (2.2).

$$\mathbf{I_{DRAIN,\,Sample} = I_{TEY,\,sample} - I_{TEY,\,membrane} - I_{electron\ from\ gas} + I_{ions\ from\ gas}} \quad (2.5)$$

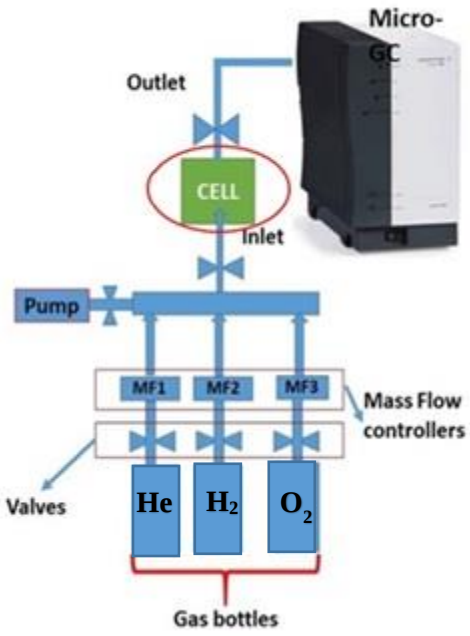

Figure 13: Gas circuit scheme at the APE-HE beamline.

The gas circuit configuration at APE-HE is depicted in the figure 13. There are 3 gas inlets, one for He (inert) and other two for the reactant gases (O_2 and H_2 in our case). All these lines finally converge as a single line inside the cell. The gas flux is controlled by three mass flow meters. The catalytic reaction takes place inside the cell and the gaseous products after the reaction flow out though an outlet gas line. This gas line is directly connected to the micro gas chromatograph (Micro GC 490 Agilent), where the gases are detected (figure 13), providing information regarding the catalytic activity inside the reactor. Exhaust coming from the micro-GC is connected to the gas recuperation unit of the Elettra experimental hall. A liquid nitrogen trap is mounted to the gas line to remove the water contaminants from the reactant gases.

2.5 **Bibliography**:

1. CRESI, J. S. P. (2019). Struttura e trasferimenti di carica in nanostrutture di ossido di cerio.
2. Chambers, A. (2004). *Modern vacuum physics*. CRC Press.
3. Siegbahn, K. (1967). ESCA: atomic, molecular and solid state structure studies by means of electron spectroscopy. *Nova Acta Regiae Societatis Scientiarum Upsaliensis*.Reinert, F., & Hüfner, S. (2005). Photoemission spectroscopy—from early days to recent applications. *New Journal of Physics*, *7*(1), 97.
4. Hortigüela, M. J., & Irurueta, G. O. (2017). X-ray Photoelectron Spectroscopy: a Surface Characterization Technique. *Mater. Today*, *8*, 18-25.
5. Chastain, J., & King Jr, R. C. (1992). Handbook of X-ray photoelectron spectroscopy. *Perkin-Elmer Corporation*, *40*, 221.
6. Ratner, B. D., & Castner, D. G. (2009). Electron spectroscopy for chemical analysis. *Surface analysis: the principal techniques*, *2*, 374-381.
7. https://www.ph.tum.de/academics/org/labs/fopra/docs/userguide-35.en.pdf
8. Skála, T., Šutara, F., Prince, K. C., & Matolín, V. (2009). Cerium oxide stoichiometry alteration via Sn deposition: Influence of temperature. *Journal of Electron Spectroscopy and Related Phenomena*, *169*(1), 20-25.
9. Binnig, G., Rohrer, H., Gerber, C., & Weibel, E. (1982). Surface studies by scanning tunneling microscopy. *Physical Review Letters*, *49*(1), 57.
10. Van de Leemput, L. E. C., & Van Kempen, H. (1992). Scanning tunnelling microscopy. *Reports on Progress in Physics*, *55*(8), 1165.
11. Heinrich, A. J., Gupta, J. A., Lutz, C. P., & Eigler, D. M. (2004). Single-atom spin-flip spectroscopy. *Science*, *306*(5695), 466-469.
12. Qiu, X. H., Nazin, G. V., & Ho, W. (2003). Vibrationally resolved fluorescence excited with sub molecular precision. *Science*, *299*(5606), 542-546.
13. https://capricorn.bc.edu/wp/zeljkoviclab/research/scanning-tunneling-microscopy-stm/
14. Besenbacher, F., Lauritsen, J. V., & Wendt, S. (2007). STM studies of model catalysts. *Nano Today*, *2*(4), 30-39.
15. Timoshenko, J., & Roldan Cuenya, B. (2020). In situ/operando electrocatalyst characterization by X-ray absorption spectroscopy. *Chemical Reviews*, *121*(2), 882-961.
16. Bordiga, S., Groppo, E., Agostini, G., van Bokhoven, J. A., & Lamberti, C. (2013). Reactivity of surface species in heterogeneous catalysts probed by in situ X-ray absorption techniques. *Chemical Reviews*, *113*(3), 1736-1850.
17. Billinge, S. J., & Levin, I. (2007). The problem with determining atomic structure at the nanoscale. *Science*, *316*(5824), 561-565.
18. Newville, M. (2014). Fundamentals of XAFS. *Reviews in Mineralogy and Geochemistry*, *78*(1), 33-74.

19. Wongjamras, A., Schlachter, A. S., & Stolte, W. C. (2011). Progress of Soft-x-ray Absorption End station for Environmental Samples. *Energy Procedia*, *9*, 56-62.
20. Koningsberger, D. C., & Prins, R. (1987). X-ray absorption: principles, applications, techniques of EXAFS, SEXAFS and XANES.
21. Benfatto, M., & Meneghini, C. (2015). A close look into the low energy region of the XAS spectra: the XANES region. In *Synchrotron radiation* (pp. 213-240). Springer, Berlin, Heidelberg.
22. Rehr, J. J., & Albers, R. C. (2000). Theoretical approaches to x-ray absorption fine structure. *Reviews of Modern Physics*, *72*(3), 621
23. Castán-Guerrero, C., Krizmancic, D., Bonanni, V., Edla, R., Deluisa, A., Salvador, F., ... & Torelli, P. (2018). A reaction cell for ambient pressure soft x-ray absorption spectroscopy. *Review of Scientific Instruments*, *89*(5), 054101.

Chapter 3

Surface modifications induced by H_2 in Cu-modified CeO_2

Cerium oxide (CeO_2, ceria) and ceria-based materials have received great attention due to their remarkable redox properties. Due to their excellent oxygen storage capacity, they represent promising candidates for heterogeneous catalytic reactions, such as for example the water gas shift reaction [1]. The catalytic properties of CeO_2 can be enhanced by doping the material with aliovalent cation species or surface modification with metal atoms such as Ag and Cu [2,3]. Metal-modified CeO_2 is considered as a suitable electrode material for proton exchange membrane fuel cells [2], due to the relatively low activation barrier for H_2 dissociation on the surface. In this chapter, I discuss in detail the surface reactivity of CeO_2 ultrathin films modified with low concentration of Cu atoms towards H_2 dissociation.

3.1 Sample preparation and reduction treatments

Cu: CeO_2 ultrathin films were grown on a Pt (111) single crystal in the UHV chamber. The Pt (111) substrate was prepared by repeated cycles of Ar sputtering (1 keV, 1 $\mu A/cm^2$) and annealing (1040 K). Surface purity after cleaning procedure was checked with XPS, and no impurities were detected before the deposition of the Cu:CeO_2 films. A 6 ML thick Cu: CeO_2 film was deposited on Pt (111) kept at RT in O_2 partial pressure ($1x10^{-7}$ mbar). Co-deposition method was employed for the preparation of the film employing an e-beam evaporator and an effusion cell for evaporating Ce and Cu atoms, respectively. The quartz microbalance was used to measure the evaporation rate before deposition and XPS was used to measure the thickness of the film deposited and the stoichiometry. The Cu concentration in the sample was estimated using the intensities of the Ce 3d and Cu 2p XPS lines to evaluate the atomic densities of Ce and Cu, as will be explained in detail in the following chapter. The nominal Cu concentration (at. %) in the film was found to be 6 at. %. The film was annealed at 770 K for 45 minutes in partial O_2 pressure (1×10^{-7} mbar) for complete oxidation and for better crystalline order before thermal treatments in UHV and in H_2. In-situ chemical and morphological characterization of the film was performed with x-ray photoelectron spectroscopy (XPS) and scanning tunneling microscopy (STM).

Thermal annealing treatments were performed both in ultra-high vacuum (1×10^{-9} mbar) and H_2 (1×10^{-7} mbar) atmospheres. The film was annealed at increasing temperature in four steps, at T= 470, 570, 670 and 770 K, each for 15 minutes, and it was subsequently cooled after each temperature to RT in reducing atmosphere (either in UHV or in H_2 pressure). XPS measurements were performed at RT after each thermal treatment, exploiting a non-monochromatized Al K_α X-ray source and hemispherical analyzer with an overall resolution of 1 eV. Spectra were measured both at normal emission and at 65° grazing emission angle with respect to surface normal to enhance the surface sensitivity. Scanning tunneling microscopy (STM) was used to investigate surface morphology of the film after thermal

cycles. STM images of the films were acquired at RT with an Omicron RT AFM/STM using a tungsten tip in constant current mode and were processed with WSxM software [4].

3.2 XPS Ce 3d spectra data analysis

XPS Ce 3d spectra of CeO_2 film and of a partially reduced CeO_2 film are shown in the figure 1 (a) and 1(b) respectively. Even though the XPS Ce 3d spectra are quite complex, the extraction of information about the concentration of Ce ions in the two different oxidation states, Ce^{4+} and Ce^{3+}, is possible with a well-established fitting procedure proposed and developed by Skala [5] and Romeo et al. [6]. The spectra can be fit using a Shirley type background plus three doublet Voigt-shaped peaks related to Ce^{4+} (u, u^{II}, u^{III}, v, v^{II}, v^{III}) and with two additional doublets for Ce^{3+} (u_0, u^{I}, v_0, v^{I}). Figure 1 (a) shows that the CeO_2 film spectrum can be fit using only the Ce^{4+}-related components, while also the Ce^{3+}-related components have to be included in the case of reduced CeO_2 as highlighted in figure 1(b), showing that the sample contains a mixture of both Ce^{4+} and Ce^{3+} ions.

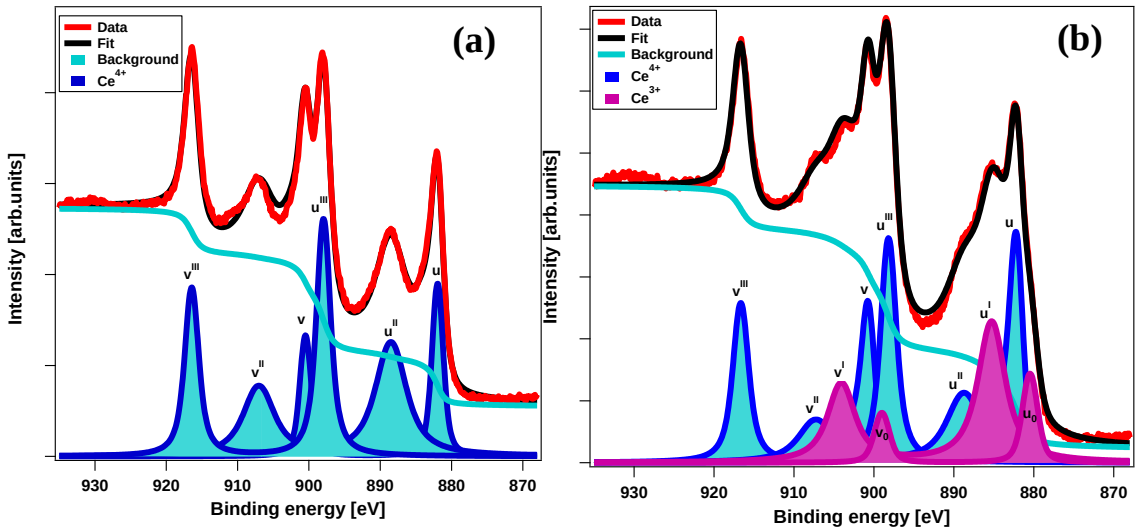

Figure 1. Experimental Ce 3d XPS spectra of CeO_2 (a) and a reduced CeO_2 (b) film and corresponding fit. The fitting components related to Ce^{4+} and Ce^{3+} ions and the Shirley background are highlighted.

The only free parameters to fit the spectra were the area of the doublets, while all the other parameters (branching-ratio, spin-orbit splitting, and widths) were adjusted on the spectra from reference samples and kept fixed in the subsequent steps. The concentration of Ce^{3+} ions is obtained by taking the ratio between the areas of Ce^{3+} and Ce total (Ce^{3+} + Ce^{4+}). The obtained values are affected by an error of +/- 2%.

The Ce 3d XPS spectra acquired in all our experiments were fitted with the above procedure to evaluate the Ce^{3+} ion evolution after each thermal step performed in UHV and in H_2. Both normal and 65° grazing emission spectra were acquired after each thermal step after cooling the film to RT. Grazing spectra were fitted in order to estimate the surface reduction of the Cu:CeO_2 films. The Cu atom concentration did not change during reducing cycles discussed in the following. In previous studies, it was established

that mobility of Cu atoms was higher than the one of Ag atoms [7], due to the lower ionic radius. Variation in the Cu dopant concentration during the treatments is discussed in detail in the next chapter.

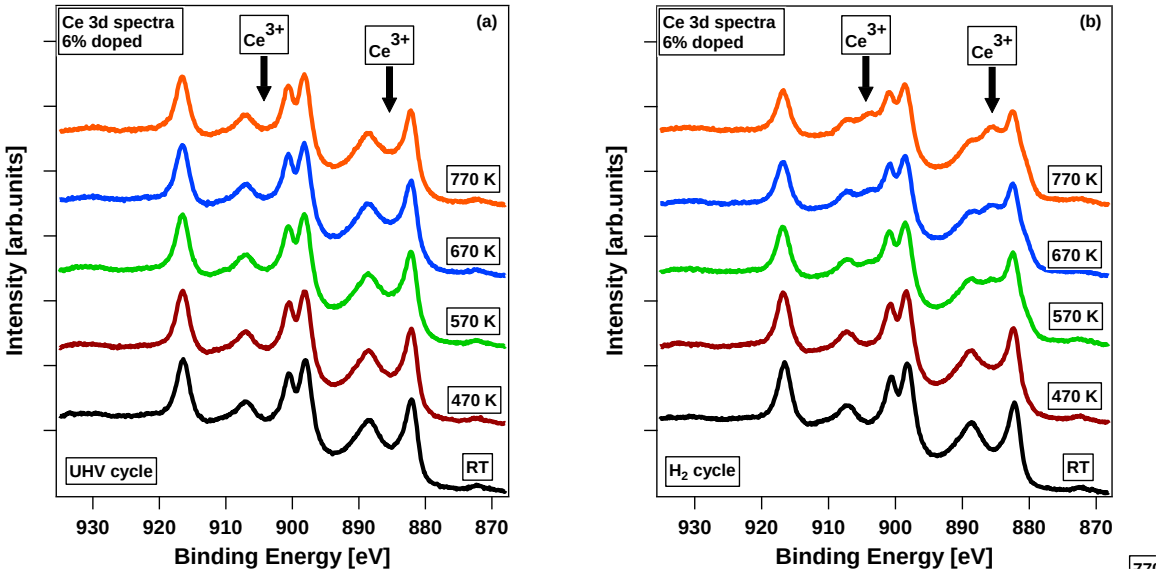

Figure 2. Ce 3d XPS spectra (grazing emission) of 6 ML Cu:CeO_2 doped with 6% Cu atoms after growth and at different annealing temperatures in UHV (a) and in H_2 (b).

In figure 2, the XPS spectra of Ce 3d line acquired at RT after the oxidation and after each thermal annealing step in UHV and H_2 are shown, the spectra were taken at 65° grazing emission. After oxidation, the spectrum had the characteristic shape of Ce^{4+} ions only (complete oxidation). This highlights the fact that the inclusion of Cu atoms into the CeO_2 had no significant effect on the oxidation state of the Ce ions. The modifications in Ce 3d spectra during thermal treatments in UHV (black) is negligible even at higher annealing temperatures. Annealing in H_2 induces a larger modification in Ce 3d spectra, which show a significant modification already at 570 K, indicating a relevant contribution from Ce^{3+} ions. Recent work done by S. Benedetti et al. [8] on Ag-modified CeO_2 also observed negligible changes in the Ce 3d spectra during UHV treatments but a non-negligible modification during temperature treatments in H_2. The reduction starts at higher annealing temperature (670 K) in H_2 for Ag:CeO_2 compared to the Cu:CeO_2 films here investigated [9], which are already significantly reduced at 570 K.

Ce 3d XPS spectra were fitted with the procedure explained before to extract the information about the Ce^{3+} evolution on the surface of the Cu:CeO_2 film during thermal annealing treatments both in UHV and in H_2. Evolution of the Ce^{3+} concentration in Cu:CeO_2 and in a pristine CeO_2 film of the same thickness during thermal annealing treatments in UHV and in H_2 are compared in figure 3.

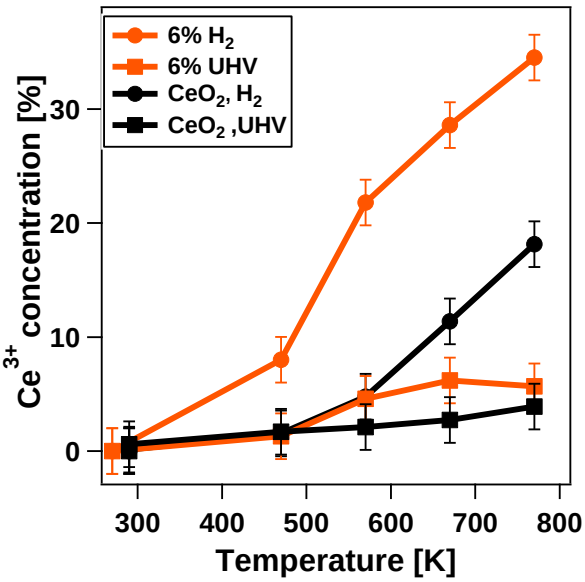

Figure 3. Evolution of Ce^{3+} ion concentration in 6% doped 6 ML Cu: CeO_2 film during UHV and H_2 thermal treatments [9] compared to pristine CeO_2. Respective Ce^{3+} values for CeO_2 are taken from reference [8].

During thermal treatments in UHV, Ce^{3+} ion concentration increases to 5.6% at 770 K for Cu: CeO_2, a value slightly higher than in pristine CeO_2 (3.9% at 770 K). On the other side a significant increase in the evolution of Ce^{3+} ions during thermal treatments in H_2 is observed in Cu:CeO_2 film, reaching up to 35% at 770 K, which is almost two times the pristine CeO_2 film at the same temperature (18%). Also, a higher Ce^{3+}concentration is observed in Cu:CeO_2 film than Ag:CeO_2 [8] during thermal treatments in H_2 (9%).

3.3 O 1s XPS spectra data analysis

To extract the information about the formation of O-H species or water species on the surface during the thermal reducing treatments, O 1s XPS spectra after each thermal step in UHV and in H_2 was acquired at 65° grazing emission angle and the spectra are shown in figure 4. Overall peak shape observed is asymmetric, with the main peak at around 529 eV related to the O-Ce bond and a shoulder at 531 eV associated to O-H groups on the surface [9].

O 1s spectra taken after oxidation at RT before reducing treatments were slightly asymmetric. Thermal treatments in UHV (black) do not induce any significant modifications in the O1s spectra even at higher annealing temperature. But in H_2, already at 570 K, a pronounced O-H shoulder is present at around 2 eV higher binding energy and evolves with increasing temperature. Due to the presence of low coordination sites (terrace steps and defects) on our film surface the asymmetric shape can be ascribed to the presence of O-H species even before the thermal treatments in H_2, due to the adsorption of H_2/ H_2O molecules, present in the background pressure of the chamber, at the defective sites on the surface.

Attribution to O-coordinated to Cu is discarded, as the binding energy observed in our case is not compatible with the Cu-O bond in Cu oxides [10].

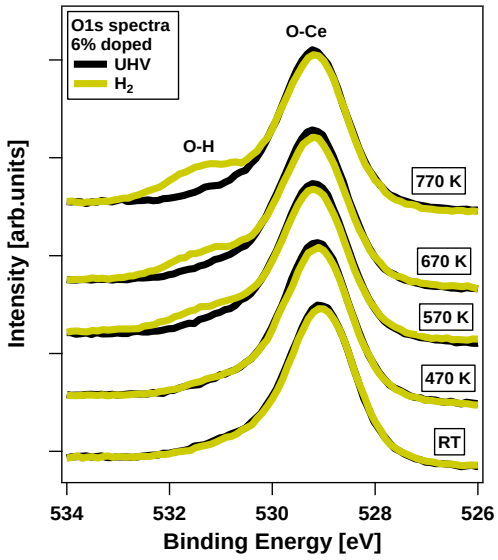

Figure 4. O 1s XPS spectra of Cu:CeO_2 sample after oxidation and after thermal treatments in UHV and in H_2.

O1s XPS spectra of 6 ML Cu:CeO_2 taken after thermal treatments have been fitted to obtain a quantitative analysis of the evolution of O-H species on the surface during thermal reducing treatments in UHV and in H_2. O 1s spectra were fit using two peaks, one related to O-Ce and a second one at approximately 2 eV higher binding energy, related to OH groups on the surface. In the fitting procedure, the intensity and the position were the free fitting parameters for both peaks to compensate for any minor changes in the O-H group binding energy and the width was fixed to the standard reference. O 1s spectrum acquired after thermal reduction cycles in H_2 together with the O-Ce and O-H fitting components are shown in the figure 5.

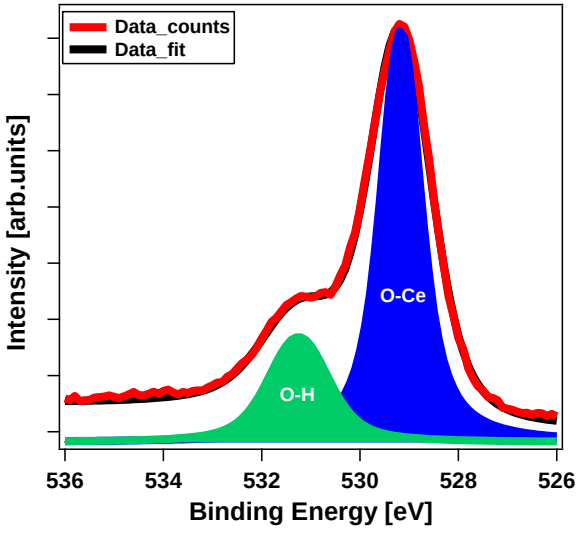

Figure 5. O1s XPS spectrum of 6 ML Cu:CeO_2 film taken after thermal treatments in H_2 and fitting components related to O-H and O-Ce.

The evolution of O-H species on the surface after reducing treatments in UHV and in H_2 is displayed in figure 6, which shows the ratio between the area of the two fitting peaks at the different temperatures.

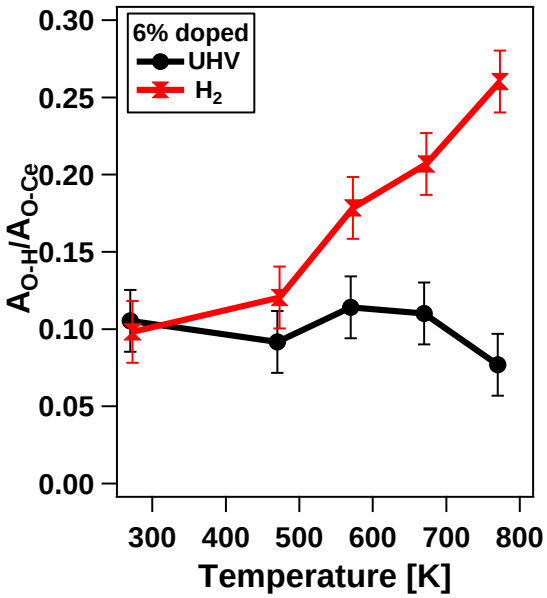

Figure 6. Ratio between O-H and O-Ce peak areas in UHV and H_2 for 6% doped 6 ML Cu:CeO_2 film.

After oxidation, the Cu:CeO_2 film showed a dominant contribution of O atoms bound to Ce and also a minor shoulder related to O-H species. UHV thermal reduction steps showed no significant increase of O-H species. On the contrary the thermal steps in H_2 induced a significant increase in the O-H relative weight, which reaches up to 25% at 770 K. The observed O-H concentration on the film surface during H_2 thermal steps is considerably higher than on the pristine CeO_2 and Ag:CeO_2 surface [8], which were 10% and 5% respectively. Density functional theory (DFT) calculations, discussed in the following sections helped us to clarify the reason for higher concentration of O-H species on the surface on the Cu-doped sample.

The information regarding O-vacancy formation on the surface during the thermal reducing treatments in UHV and in H_2 is extracted from the O 1s fit by taking the ratio of areas between O-main component and Pt $4p_{3/2}$. The XPS spectrum acquired after the reduction cycle in H_2 containing O 1s and Pt $4p_{3/2}$ is shown in figure 7. Since the photoelectrons from O 1s and Pt $4p_{3/2}$ have very close kinetic energies, and thus have similar escape depths, the ratio of the intensity of the two peaks provides the information about evolution of oxygen vacancy concentration.

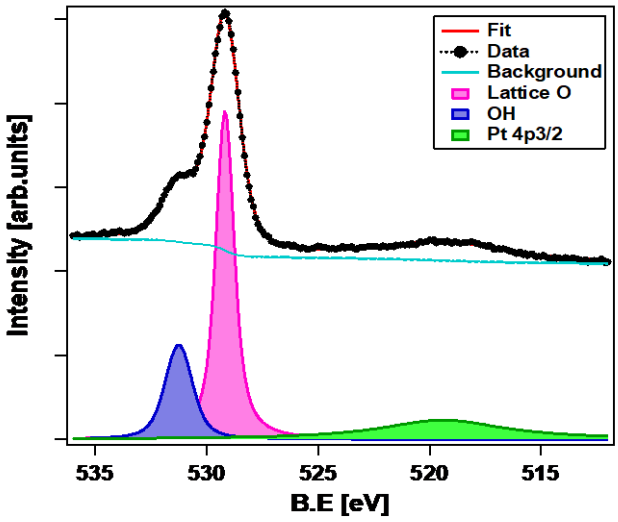

Figure 7. XPS spectrum containing O 1s and Pt $4p_{3/2}$ regions acquired after reduction cycle in H_2 with fitting components and background.

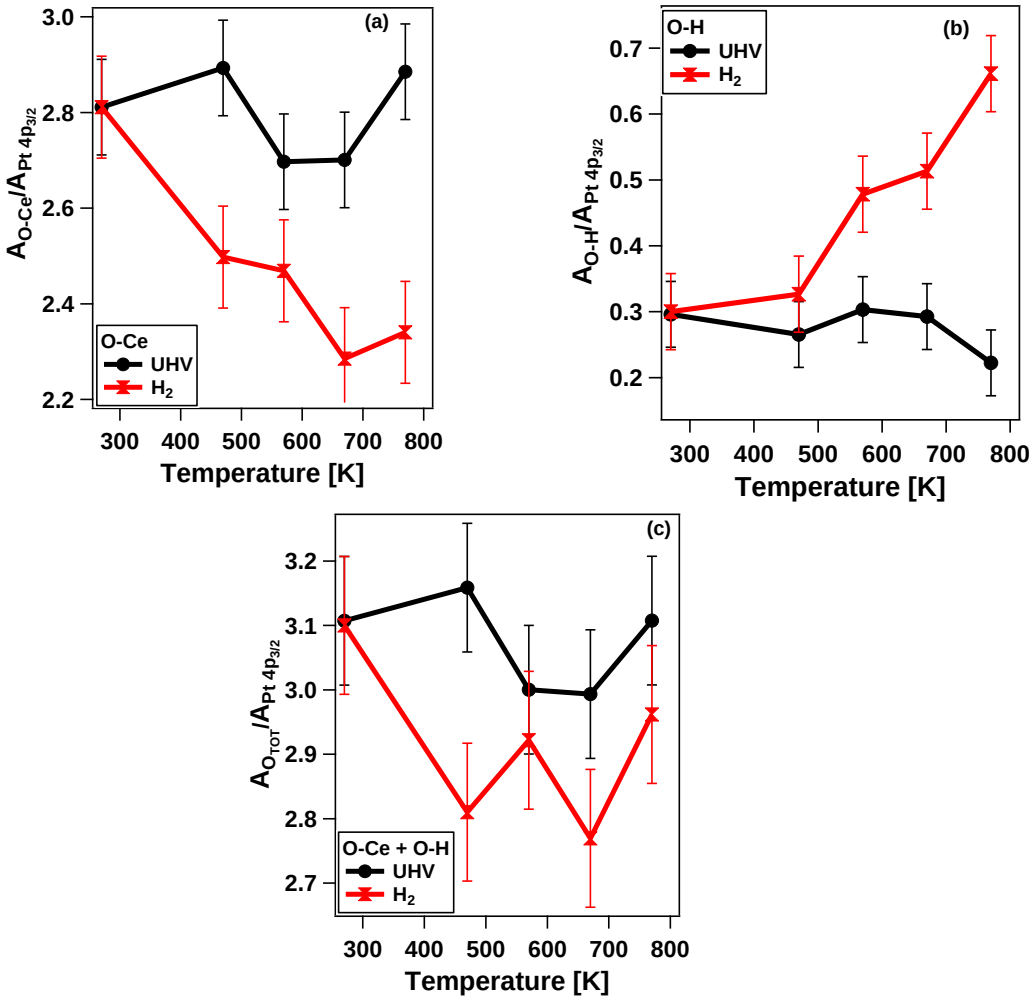

Figure 8. Ratio of the areas of different components of O1s to Pt $4p_{3/2}$ extracted from O 1s XPS fitting of Cu:CeO_2 film after UHV and H_2 thermal treatments and: a) O-Ce; b) O-H; c) O-Ce + O-H

In figure 8, the ratio of area between O-Ce, O-H, and O-Tot (O1s total area) components to Pt $4p_{3/2}$ and their behavior during thermal steps in UHV and in H_2 is shown for 6% doped Cu:CeO_2 film. From figures 8a and 8b, it is clear that the variations in the ratios during the UHV treatments is small and is consistent with the evolution of Ce^{3+} on the surface of Cu:CeO_2 film (figure 3). A significant drop in the O-Ce component during H_2 treatment is observed, but as the temperature increases the variation tends to slow down, whereas the O-H area increase is more significant at higher temperatures (figure 8b). This indicates that during H_2 thermal steps, the O-vacancy formation on the surface is initiated at lower temperatures (470 K) probably due to the removal of O-atoms from defective sites. The formation of water and the desorption of the same creates O-vacancies on the surface. But the O-H weight increases due to the dissociative adsorption of H_2 molecules on the surface during the cooling phase. The decrease in the O-Ce area at higher temperatures is less pronounced, probably due to the finite density of defect sites and to the need of temperatures even higher than 770 K to remove further O atoms from more regular surface sites. The adsorbed hydrogen molecules dissociated on the surface can also bind to an oxygen atom on the surface forming water and leaving an oxygen vacancy. The drop in the ratio O_{tot}/ Pt $4p_{3/2}$ at 470 K can indicate oxygen removal and water formation. After higher temperature treatments, the re-adsorption of O-H during cooling in H_2 may determine the observed saturation in the O_{tot}/ Pt $4p_{3/2}$ ratio.

3.4 Surface morphology

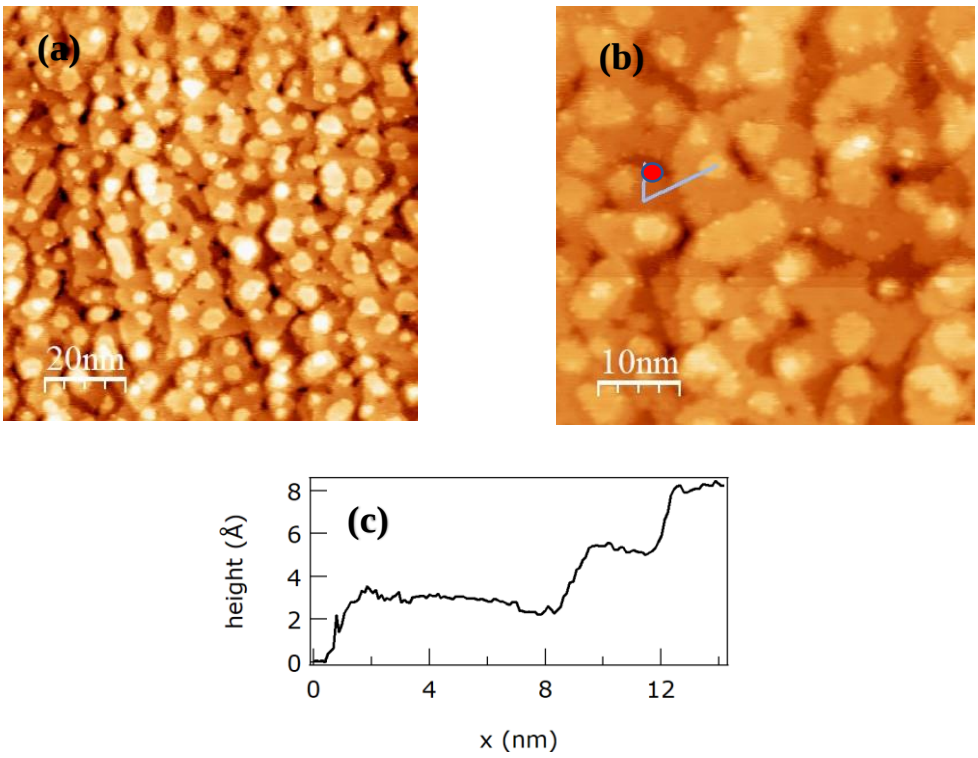

Figure 9. STM images of the oxidized 6% doped Cu:CeO_2 sample: a) 100×100 nm^2 (2.7 V, 0.03 nA); b) 50×50 nm^2 (2.67 V, 0.03 nA). c) height profile across the blue broken line shown with red dot as the initial point.

STM images of 6% Cu:CeO_2 were taken at RT before and after reduction cycles to investigate any changes occurred on the surface after treatments. Surface topography of the film after the oxidation before thermal reduction is shown in figure 9. The surface morphology is considerably rough, and the brighter spots are areas with irregular shapes with lateral size 3-6 nm. The area exposed in the STM images are 25%, 55% and 20% for the top, intermediate and the third layer respectively. The surface beneath the irregular shapes is uneven. In figure 9b, a height profile is drawn starting from the red dot and is reported in figure 9c. The height profile is compatible with different CeO_2 (111) planes being exposed with an average interplanar distance of 3 Å (expected 3.125 Å).

After the thermal reduction steps in H_2, acquiring STM images was tricky and unstable. Possible reason for this instability can be ascribed to the interaction between tip and the O-H species on the surface. The surface morphology of Cu:CeO_2 sample taken after reoxidation is shown in the figure 10, and it was comparable to the surface after reduction cycle in H_2. No appreciable difference between areas exposed was found before and after treatments (figure 9 and figure 10).

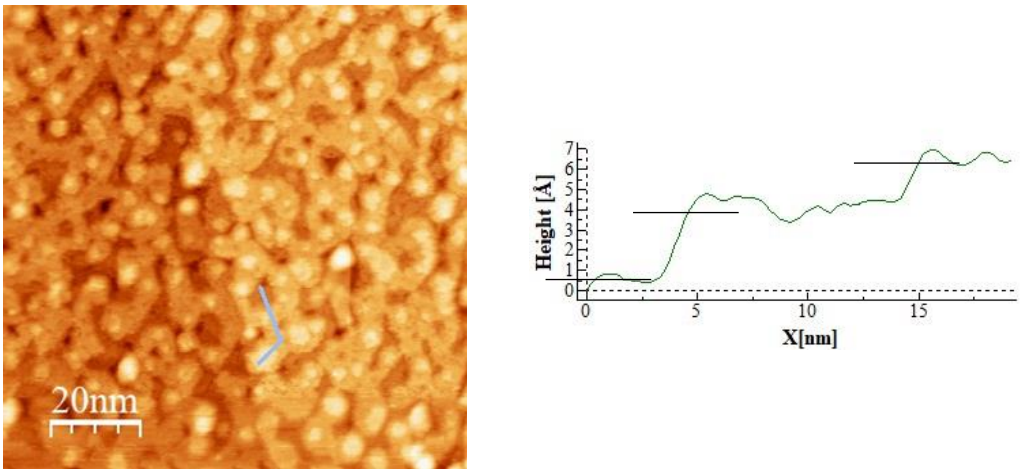

Figure 10. 100×100 nm² STM image of re-oxidized Cu:CeO_2 surface taken reduction cycle in H_2 with its height profile.

3.5 Theoretical calculations

DFT calculations to understand the reduction mechanisms of our film during thermal reduction cycles were performed by Dr. Giulia Righi, prof. Rita Magri and prof. Annabella Selloni [2, 9]. Cu atoms introduced into the stoichiometric CeO_2 (111) are in +2 oxidation state and cause distortion in the lattice and spontaneous O-vacancy formation [11]. The released O-atom in the calculations is not one of the four oxygens bonded directly to Cu atom but one of the atoms displaced away from it by the Cu-induced distortion of the lattice. The released O-atom does not directly bond with Cu atoms, and therefore the Cu atom remains in +2 state, whereas two Ce ions reduce from +4 to +3 state. The removal of an oxygen atom bonded to Cu is not spontaneous due to the higher formation energy (E_{Form} = +0.70 eV), but this would lead to the change of oxidation state of Cu atoms from +2 to +1.

3.5.1 Reduction during thermal steps in UHV

The effect of temperature on the reduction of CeO_2 due to the oxygen vacancy formation is well-established [3,8]. DFT calculations investigated also the formation of a second oxygen vacancy [9]. For Cu-doped CeO_2 two kinds of O-vacancies can be created on the surface. The first one, with a E_{Form} = 1.0 eV, determines the reduction of two Ce atoms from +4 to +3, whereas the second one, with E_{Form} = 1.4 eV, leads to the reduction of a Cu atom from $Cu^{2+}$to Cu^{1+} and the delocalization of additional electrons on two Ce ions and on surface O ions. So, the observed oxygen vacancy formation energy in Cu: CeO_2 is much smaller than on pristine ceria (E_{form} = 2.02 eV) and more oxygen vacancies are formed on the Cu-modified surface than on pristine ceria during thermal treatments. Due to some of the O-vacancies formed on the surface on the Cu:CeO_2 film, some Cu atoms with +1 oxidation state are produced and are highly active.

3.5.2 Reduction during thermal steps in H_2

During thermal treatments in H_2, the process of dissociation and adsorption of H atoms on the surface takes place along with the O-vacancy formation activated by the rise in the temperature. The activation energy for the dissociation of H_2 is slightly smaller (+0.8 eV) compared to pristine ceria (+0.99 eV). But the presence of highly active Cu^{1+} species on the surface can further decrease the energy barrier for H_2 dissociation. To prove this, theoreticians considered one additional O-vacancy per unit cell on the stable surface, which generated Cu^{1+} cation species. These active Cu^{1+} species significantly reduced the energy barrier for H_2 dissociation to 0.33 eV. So, the presence of active Cu^{1+} plays a huge role in the higher dissociation of H_2 on the surface compared to pristine and Ag:CeO_2 [8]. Furthermore, the dissociated hydrogen atoms move towards O atoms, overcoming an energy barrier of 0.37 eV giving rise to two OH groups on the surface.

3.5.3 Discussion

Our combined experimental and DTF results allow us to obtain valuable information on the interaction between Cu:CeO_2 and H_2. The calculations predict a barrier for H_2 dissociation on the stable (111) surface of Cu:CeO_{2-x} of 0.8 eV, not significantly lower than the barrier on the pure CeO_2 surface (0.99 eV) [2,8]. However, the dissociative adsorption of H_2 on Cu:CeO_{2-x} leads to the reduction of a Ce ion from 4+ to 3+ and of a Cu ion from 2+ to 1+. The Cu^{1+} species is very reactive and significantly decreases the dissociation barrier for an additional H_2 to about 0.33 eV, a value much lower than on pure CeO_2 [2,8]. Based on these results, it is reasonable to assume that the initial dissociation of H_2 on the Cu:CeO_2 surface is promoted by temperature and possibly also by the non-ideal surface morphology of the films investigated here, where extended terrace edges, kinks, and other defect-related low coordination sites may contribute to a further decrease in the barrier for H_2 dissociation. After the initial dissociation, the Cu^{1+} ions present on the surface greatly facilitate further dissociation. This explains

the marked increase in Ce^{3+} concentration during the thermal cycle in H_2 experimentally observed by XPS (Figure 3). The same mechanism allows us to ascribe the increase in the OH-related signal with temperature (Figure 6) to the gradually more efficient dissociation of H_2 molecules as the temperature is increased, leading to the formation of surface OH groups upon cooling. Although water formation was not explicitly simulated, recent results for Ag:CeO_2 suggest that water formation and desorption can explain the observed decrease in O 1s/Pt $4p_{3/2}$ ratio already at mild temperatures (Figure 8). The creation of an O vacancy due to water formation and desorption leaves the two Ce ions involved in H_2 dissociation in the 3+ oxidation state. For this reason, the increase in Ce^{3+} concentration with respect to the initial value during the thermal cycle in hydrogen (Figure 3) can be partly ascribed to the electrons left on the lattice by oxygen vacancy formation and partly to those left by H_2 dissociation and OH formation during the cooling phase. We note that although in the present experiment, it was not possible to reliably determine the Cu oxidation state experimentally, previous work showed that Cu^{1+} species can be stabilized both in the form of dopants in ultrathin ceria films [3] and by depositing Cu atoms at RT on a pure ceria surface [2,12].

Interestingly, the Cu:CeO_2 film in a H_2 environment investigated in this work showed a behavior different from that of both pure CeO_2 and Ag-modified CeO_2 films of the same thickness grown with the same method in the same conditions, although with a higher dopant concentration [8]. A direct comparison of the Ce^{3+} concentration and OH surface concentration with the thermal treatment in H_2 for the Ag- and Cu-doped samples is reported in Figure 11.

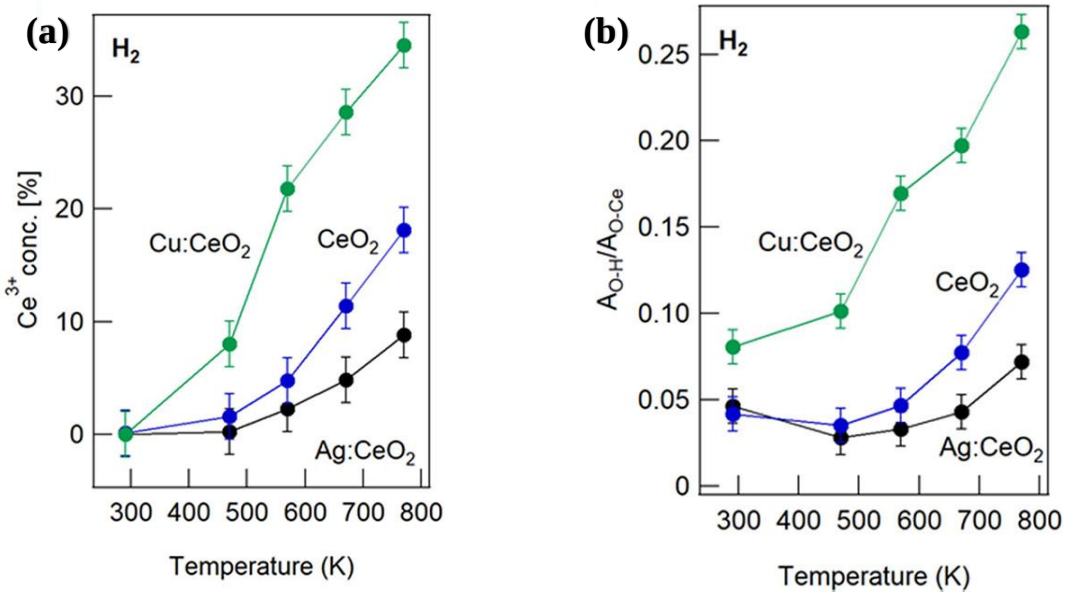

Figure 11. (a) Ce^{3+} concentration and (b) OH surface concentration after the different thermal annealing steps in H_2 for 6% Cu-doped sample investigated here, a 10% Ag-doped film, and a pure CeO_2 film with the latter two investigated in ref 8.

In the Ag-doped sample, the Ce^{3+} and OH concentrations only show a mild increase upon thermal treatment in H_2, in spite of the higher Ag concentration. Figure 12 summarizes the reactions that are predicted by the model to occur on the two stable doped surfaces, i.e. the surfaces on which the spontaneous formation of the compensating oxygen vacancy has taken place. The scheme shows that on $Ag:CeO_2$, the formation of an additional O vacancy, or the dissociative absorption of hydrogen, leads to the localization of one of the two electrons on the Ag dopant, which changes its oxidation state from 2+ to 1+, while only one of the electrons is localized on a Ce ion, which changes its formal oxidation state from 4+ to 3+. On the Cu-doped sample, instead, the lower reducibility of Cu as compared to Ag ions makes it much more likely for both electrons left by an O vacancy to localize on two Ce ions. Moreover, the formation energy of the second oxygen vacancy is higher for the Cu doped sample than for the Ag-doped sample. Therefore, the different redistribution of charge after O vacancy formation or H_2 dissociation in the two systems can explain the more pronounced increase of Ce^{3+} in $Cu:CeO_2$. The rationale for the higher OH surface concentration in the case of the Cu-doped sample with respect to the Ag-doped one during the reduction cycles in hydrogen can be found in the lower concentration of surface O vacancies.

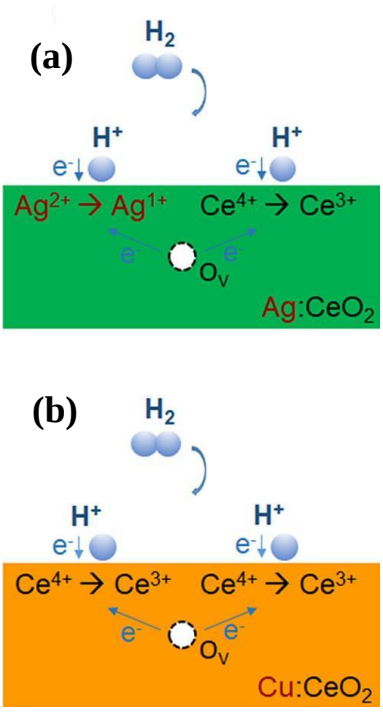

Figure 12. Sketch of the two doped surfaces exposed to H_2 with an O vacancy. (a) On the $Ag:CeO_2$ surface, the dissociative absorption of H_2 or the formation of an O vacancy reduces an Ag atom, which changes its oxidation state from 2+ to 1+, and a Ce atom from 4+ to 3+. (b) On the $Cu:CeO_2$ surface, the dissociative absorption of H_2 or the formation of an O vacancy preferentially reduces two Ce atoms

We note that the Ce^{3+} concentration shows a similar trend also in UHV, with the Cu (Ag)-doped sample having a systematically higher (lower) concentration than the undoped film (Figure 13). Moreover, the

films investigated here have a significantly lower reducibility in UHV than the much thinner Cu:CeO_2 films investigated in reference 3, in agreement with the already observed dependence of the reducibility on the thickness of the film, ascribed to the interaction with the substrate [13,14]. Ag and Cu dopants exhibit a very different behavior. Ag captures part of the excess electrons released by the oxygen vacancies or when H_2 is dissociatively adsorbed on the surface because Ag^{1+} is the most stable oxidation state. The 2% error bars used in figure 13 indicates the precision in the Ce 3d fitting procedure employed to estimate Ce^{3+} concentration on the samples.

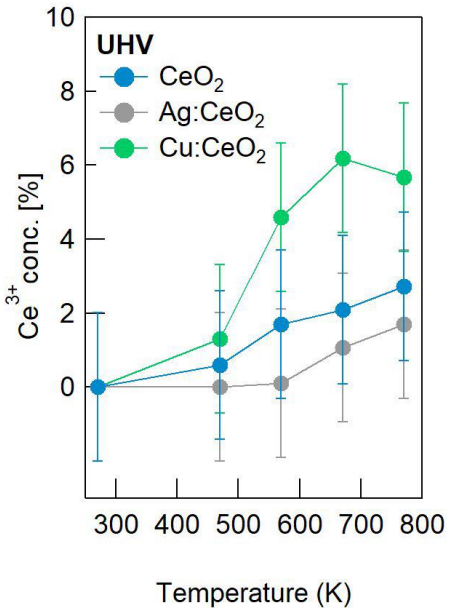

Figure 13. Comparison of the Ce^{3+} concentration derived from the fitting of Ce 3d XPS lines for the pure ceria film and the Ag- and Cu-doped ones. The data concerning the Ag-doped sample are taken from reference [8].

On the contrary, in the case of Cu-doped ceria, the excess electrons prefer to localize on the Ce ions, and Cu keeps its most stable 2+ oxidation state. Interestingly, however, when some Cu^{1+} species are formed, driven by the thermal treatments, the barrier for H_2 dissociation can be significantly decreased, leading to a further increase in the concentration of Ce^{3+} and surface OH groups as compared to the case of pure ceria.

3.6 Bibliography:

1. Gorte, R. J. (2010). Ceria in catalysis: From automotive applications to the water–gas shift reaction. *AIChE Journal*, *56*(5), 1126-1135.
2. Righi, G., Magri, R., & Selloni, A. (2019). H2 dissociation on noble metal single atom catalysts adsorbed on and doped into CeO2 (111). *The Journal of Physical Chemistry C*, *123*(15), 9875-9883.
3. Gasperi, G., Brugnoli, L., Pedone, A., Menziani, M. C., Valeri, S., & Luches, P. (2019). Reducibility of Ag-and Cu-Modified Ultrathin Epitaxial Cerium Oxide Films. *The Journal of Physical Chemistry C*, *123*(22), 13702-13711.
4. Horcas, I., Fernández, R., Gomez-Rodriguez, J. M., Colchero, J. W. S. X., Gómez-Herrero, J. W. S. X. M., & Baro, A. M. (2007). WSXM: A software for scanning probe microscopy and a tool for nanotechnology. *Review of Scientific Instruments*, *78*(1), 013705.
5. Skála, T., Šutara, F., Prince, K. C., & Matolín, V. (2009). Cerium oxide stoichiometry alteration via Sn deposition: Influence of temperature. *Journal of Electron Spectroscopy and Related Phenomena*, *169*(1), 20-25.
6. Romeo, M., Bak, K., El Fallah, J., Le Normand, F., & Hilaire, L. J. S. (1993). Analysis, I. XPS study of the reduction of cerium dioxide. *Surf. Interface Anal*, *20*, 508-512.
7. Shannon, R. D. (1976). Revised effective ionic radii and systematic studies of interatomic distances in halides and chalcogenides. *Acta crystallographica section A: Crystal physics, Diffraction, Theoretical and General Crystallography*, *32*(5), 751-767.
8. Benedetti, S., Righi, G., Luches, P., D'Addato, S., Magri, R., & Selloni, A. (2020). Surface reactivity of Ag-modified ceria to hydrogen: a combined experimental and theoretical investigation. *ACS Applied Materials & Interfaces*, *12*(24), 27682-27690.
9. Vikatakavi, A., Benedetti, S., Righi, G., Magri, R., D'Addato, S., Luches, P., & Selloni, A. (2022). Interaction of Hydrogen with Cu-Modified Cerium Oxide Surfaces. *The Journal of Physical Chemistry C*.
10. Platzman, I., Brener, R., Haick, H., & Tannenbaum, R. (2008). Oxidation of polycrystalline copper thin films at ambient conditions. *The Journal of Physical Chemistry C*, *112*(4), 1101-1108.
11. Yang, Z., He, B., Lu, Z., & Hermansson, K. (2010). Physisorbed, chemisorbed, and oxidized CO on highly active Cu− CeO2 (111). *The Journal of Physical Chemistry C*, *114*(10), 4486-4494.
12. Li, G., Hu, S., Xu, Q., & Zhu, J. (2019). Interaction between Cu Nanoparticles and CeO2 (111) Film Surfaces. *The Journal of Physical Chemistry C*, *123*(38), 23563-23571.
13. Luches, P., Pagliuca, F., & Valeri, S. (2014). Structural and morphological modifications of thermally reduced cerium oxide ultrathin epitaxial films on Pt (111). *Physical Chemistry Chemical Physics*, *16*(35), 18848-18857.
14. Gasperi, G., Amidani, L., Benedetti, F., Boscherini, F., Glatzel, P., Valeri, S., & Luches, P. (2016). Electronic properties of epitaxial cerium oxide films during controlled reduction and oxidation studied by resonant inelastic X-ray scattering. *Physical Chemistry Chemical Physics*, *18*(30), 20511-20517.

Chapter 4

Dopant stability and modifications in Cu:CeO_2 at increasing dopant concentration

In this chapter, I will describe and discuss the results obtained on the Cu-doped CeO_2 ultrathin films for different dopant concentration, prepared using the same procedure explained in chapter 3. The main goal was to investigate the modifications induced by H_2 in UHV-compatible conditions on the chemical and electronic properties of ceria when an increasing amount of Cu dopant atoms is included in the oxide. Previous works have in fact shown that the doping of CeO_2 with aliovalent atoms can reduce the barrier for H_2 dissociation [1,2]. Theoretical calculations [4] predicted that Cu dopant atoms substitute Ce atoms in the matrix rather than being introduce interstitially in the oxide. Also, we have also focused on understanding the effect of thermal treatments on the stability of Cu dopant atoms in the samples after each thermal treatment in both UHV and H_2. Moreover, we have also studied the surface modifications of the samples using STM at room temperature to detect any changes due to the thermal treatments. For this purpose, we have investigated films with two different Cu concentration and two films with different architectures.

4.1 Films with different doping concentration

We prepared two 6 ML Cu-doped ultrathin films of CeO_2 with two dopant concentrations, namely 6% and 27%, and investigated their behavior in UHV and in H_2 environments at different annealing temperatures. The dopant concentrations were chosen to appreciate the difference induced by the dopant concentration on the reactivity of the films. The basic structure of the films is shown in figure 1. 6 ML Cu-doped CeO_2 films were grown on Pt (111) substrate at RT as described in chapter 3, section 3.1. Due to the growth method employed, Cu atoms are expected to be distributed evenly throughout the film. Samples prepared at RT were oxidized at 770 K for 45 minutes in partial pressure of O_2 (1×10^{-7} mbar) for complete oxidation and to improve crystalline order before any treatments in UHV and in H_2. After the oxidation, the thermal reduction cycles of these films were done both in UHV (1×10^{-9} mbar) and in H_2 (1×10^{-7} mbar) at 4 different temperatures: 470 K, 570 K, 670 K and 770 K respectively for 15 minutes each. The first cycle undergone by each sample was in UHV. The samples were re-oxidized before performing the following reduction cycle in H_2. XPS spectra of the Ce 3d, Pt 4f, Pt $4p_{3/2}$, O1s and Cu 2p regions were measured employing an Al-K_α x-ray source and a hemispherical electron analyzer. XPS spectra were measured after growth and after each thermal treatment step after cooling the sample in reducing environment to RT, both at normal (0°) and grazing emission angles (65° from the surface normal). Grazing emission spectra of the

samples were taken to enhance the surface sensitivity and to better determine the surface modifications of the films in UHV and H_2 environments.

Figure 1. Basic architecture of the Cu-doped CeO_2 films grown on Pt (111) substrate.

4.1.1 Cu doping stability

To understand the effect of the thermal treatments on the Cu dopant atoms, we measured the XPS Cu 2p line for the two films at both normal and grazing emission before and after the treatments. As the Cu doping concentration on the surface of the film influences the reduction of CeO_2, it is essential to determine if the Cu included during co-deposition remains stable and diluted in the film and formulate the relation between doping and reduction of the CeO_2 at each step of the treatment. Therefore, we have calculated the doping of the sample surface for each UHV and H_2 reduction treatment steps.

As shown in figure 2a, the Cu 2p spectra of the 27% doped sample after growth at normal and grazing emission are comparable in intensity, as expected for a uniform distribution of the Cu atoms across the sample. However, a pronounced decrease of the Cu 2p peak intensity at grazing emission (pink curve) is noticeable after the full treatment in H_2 (770 K) when compared to the normal emission. This indicates that the Cu dopant atoms have a tendency to migrate underneath the top surface layers towards the bulk/interface with the support, at variance with the case of Ag dopant atoms previously investigated [1].

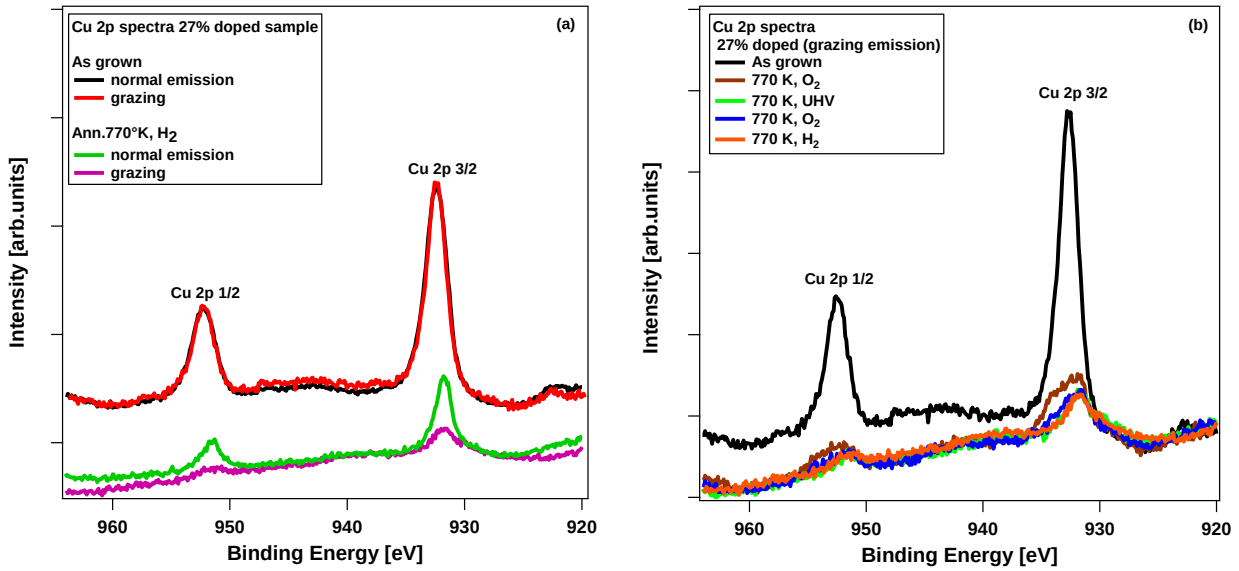

Figure 2. (a) Comparison of the variation in the Cu 2p intensities before (as grown) and after treatments in H_2 for 27% doped sample in both normal and grazing emission. (b) Variation in Cu 2p grazing emission spectra of 27% doped Cu: CeO_2 film after the various treatments.

The variation of Cu 2p peak intensities after each step at grazing emission for the 27% doped sample is shown in figure 2b. From the figure it is quite clear that a significant decrease in the Cu 2p intensity occurs after the first oxidation treatment, while the variation in the intensities after the following treatments is small. So, the first oxidation step causes a strong migration of the Cu atoms towards the interface with the support.

To estimate the actual Cu doping concentration (at.%) after each treatment in UHV and H_2, we have calculated it from the Cu 2p spectra with the procedure explained below.

First the background has been subtracted in two steps:

Step 1. Linear background subtraction from the Cu 2p XPS spectra.

Step 2. Subtraction of Ce 3d satellite arising due to plasmon excitation.

An example of background subtraction is reported in figure 3.

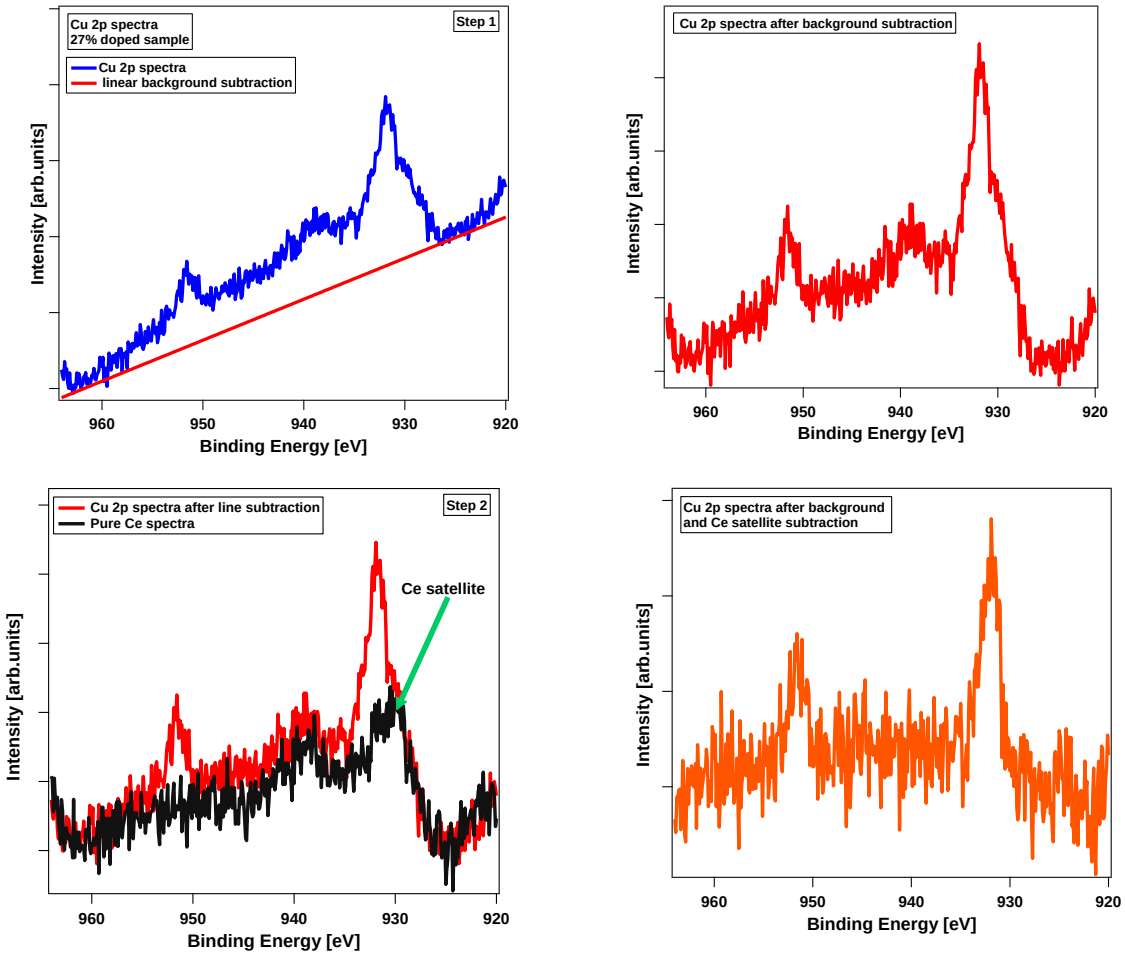

Figure 3. Illustration of the Cu 2p background subtraction.

Doping is then calculated from the Cu 2p spectra after background subtraction by calculating the area of Ce 3d and Cu 2p regions.

Given than

$$\frac{M_{Ce}}{M_{Cu}} = \frac{[\sigma\phi T\lambda Q(s,\lambda)]_{Ce}}{[\sigma\phi T\lambda Q(s,\lambda)]_{Cu}} \cdot \frac{n_{Ce}}{n_{Cu}}$$

Where M_{Ce} is the area under Ce 3d peak, M_{Cu} the area under Cu 2p peak after background subtraction, σ is the photoionization cross-section, ϕ the asymmetry parameter, T the analyzer transmission function, λ the inelastic mean free path of photoelectrons, Q(s,λ) the attenuation of the photoelectron intensity due to inelastic scattering through a sample of thickness s and depends on λ. Since T and λ depend on the kinetic energy of photoelectrons that is the same for Ce3d and Cu2p, and the thickness is the same, the ratio depends only on tabulated σ and ϕ and on the atomic density ratio. Therefore, we can obtain the dopant concentration defined as:

$$C_{Cu} = \frac{n_{Cu}}{n_{Ce} + n_{Cu}}$$

as calculated from the ratio of the peak areas:

$$C_{Cu} = \frac{1}{1 + \frac{(\sigma\phi)_{Cu}}{(\sigma\phi)_{Ce}} \cdot \frac{M_{Ce}}{M_{Cu}}}$$

The results for 6% and 27% doped samples at different treatment steps are reported in figure 4.

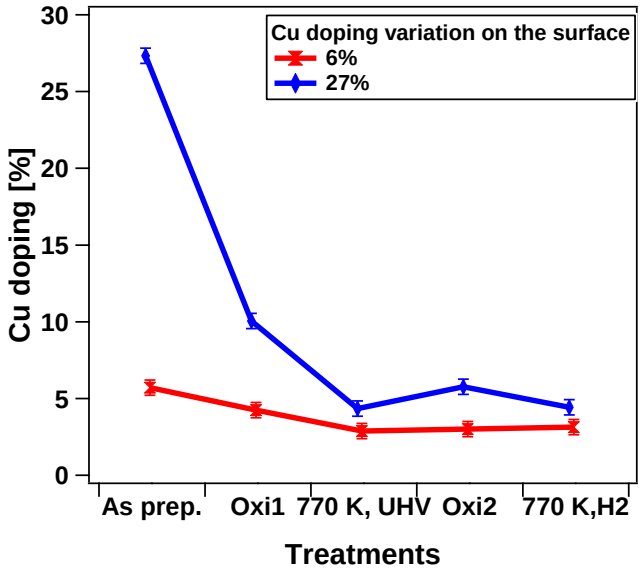

Figure 4. Cu doping concentration (at. %) after different treatment steps for 6% and 27% doped samples.

As can be seen from the figure, in the highly doped sample the doping concentration on the surface drops significantly from 27% to 10% after the first oxidation and stabilizes during the later treatments to value around 5%. The modification of the Cu concentration is much less pronounced but non-negligible (from 6% to 3%) for the sample with a lower initial doping, possibly because Cu ions in low concentrations are more stable within the CeO_2 matrix, while when the concentration is high the dopant atoms are less stable and they tend to migrate from the surface to the buried interface. So, for both samples only a partial and similar amount of the dopant atoms remains on the surface after the first two cycles of treatments and play a role in the reactivity. From this we can estimate that the solubility limit of the Cu in CeO_2 is below 6%. However, films remain active even at higher doping concentration. Also, the possibility that part of the Cu atoms moves to the surface and desorbs cannot be excluded.

4.1.2 Evolution of Ce^{3+} concentration

We have measured Ce 3d XPS spectra of the two samples after each thermal treatment in both UHV and H_2 to understand the reduction of the Cu: CeO_2 films. The Ce 3d spectra measured at RT after post growth oxidation and after the thermal treatments in UHV and H_2 for the two films are displayed in figure 5. All the spectra are taken at grazing emission angle. Before any reducing treatment the films were annealed at 770 K in O_2 partial pressure (1 x 10^{-7} mbar) for 45 minutes for complete oxidation and to reach a stable distribution of Cu atoms.

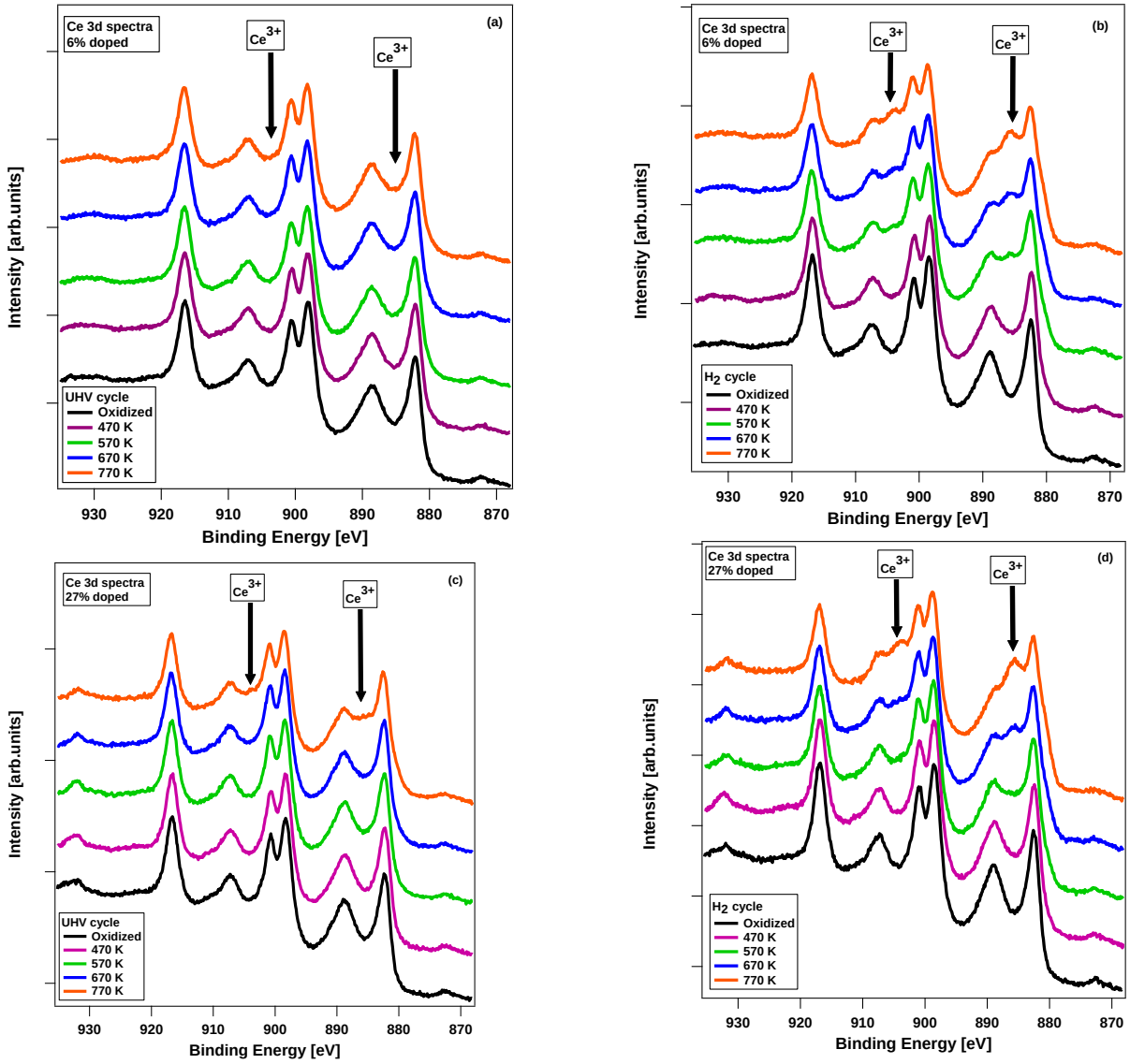

Figure 5. Ce 3d XPS spectra (grazing emission) of 6 ML Cu: CeO_2 doped with 6% (a and b) and 27% (c and d) at different annealing treatments in UHV and in H_2.

After this treatment Ce 3d spectra has a shape that corresponds to the presence of Ce^{4+} ions only. After the thermal reduction steps in UHV the modifications in the 6% doped sample are negligible (figure 5a), while they are clearly more pronounced for the 27% doped sample (figure 5c). However, temperature treatments in H_2 induce a greater modification to the Ce 3d spectra when compared to the UHV cycle for both samples (figure 5b and 5d).

Ce 3d peaks were fitted using the procedure explained in chapter 3, section 3.2 [3]. The Ce^{3+} concentration in the film was evaluated by taking the ratio of two Ce^{3+} doublets to the total Ce 3d area. The quantitative results from the analysis of the Ce 3d spectra for the evolution of Ce^{3+} ion concentration in 6% and 27% doped Cu: CeO_2 films is shown in figure 6 in UHV and H_2, in comparison with the values of reduction in pure CeO_2 of the same thickness measured previously [1].

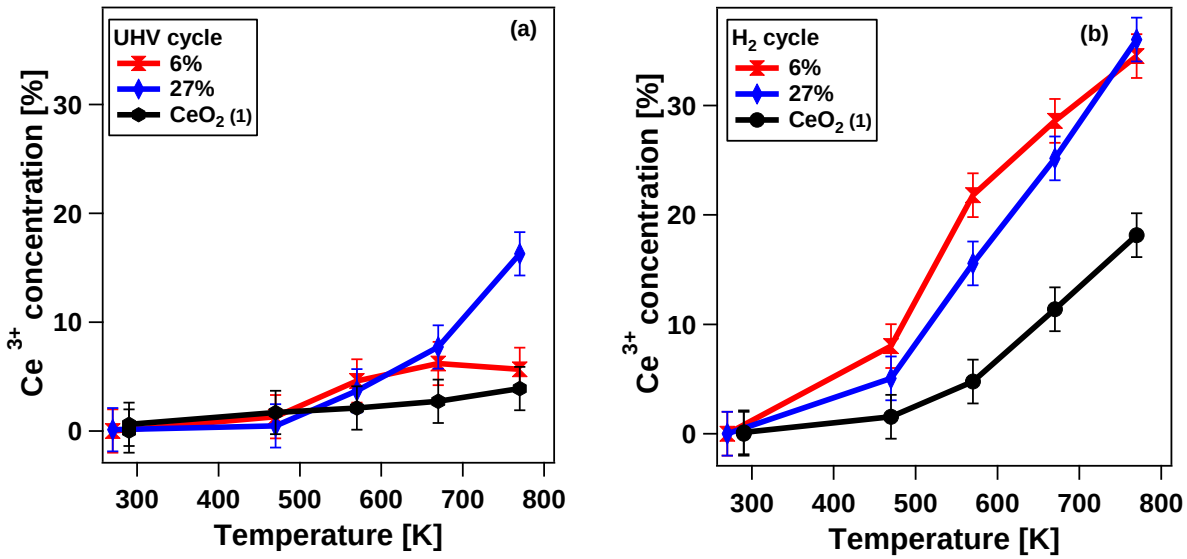

Figure 6. Evolution of Ce^{3+} in the 6% and 27% doped films in UHV (a) and H_2 (b) in comparison with pure CeO_2. The values for the pure CeO_2 film are taken from reference [1].

Treatments in UHV have shown to induce a moderate increase of Ce^{3+} concentration in the pure ceria and in the 6% doped as shown in figure 6(a). On the contrary 27% doped film showed a greater reduction in UHV and reaches up to 16% Ce^{3+} concentration at 770 K. This can be ascribed to the presence of higher amount of Cu atoms in the film, which possibly reduces more Ce atoms by creating more oxygen vacancy. Whereas a significant increase in the Ce^{3+} for both 6% and 27% was observed when treated in H_2 and the concentration reaches up to 35% and 36% respectively at 770 K. Already at 570 K, the reduction of the samples in H_2 were significantly high and the Ce^{3+} concentration increases with the increasing temperature as shown in figure 6b. Cu:CeO_2 films here investigated showed a higher Ce^{3+} concentration compared to pure and Ag-doped Ceria films, prepared with the same procedures, previously explored [1]. As discussed

in the chapter 3, Cu atoms in CeO_2 dissociates more H_2 than pure and Ag-modified CeO_2 which generates more electrons and most of these electrons are acquired by Ce ions. So, a higher reduction in the Cu:CeO_2 is observed than pure and Ag:CeO_2 samples.

4.1.3 OH surface adsorption

Along with the Ce 3d, we have measured the XPS spectra of the O1s region at grazing emission angle after each treatment in UHV and H_2 to understand the formation of OH (hydroxyl) groups or water species on the surface. O1s XPS spectra of 6% and 27% doped films taken after temperature treatments in both UHV and H_2 are shown in figure 7.

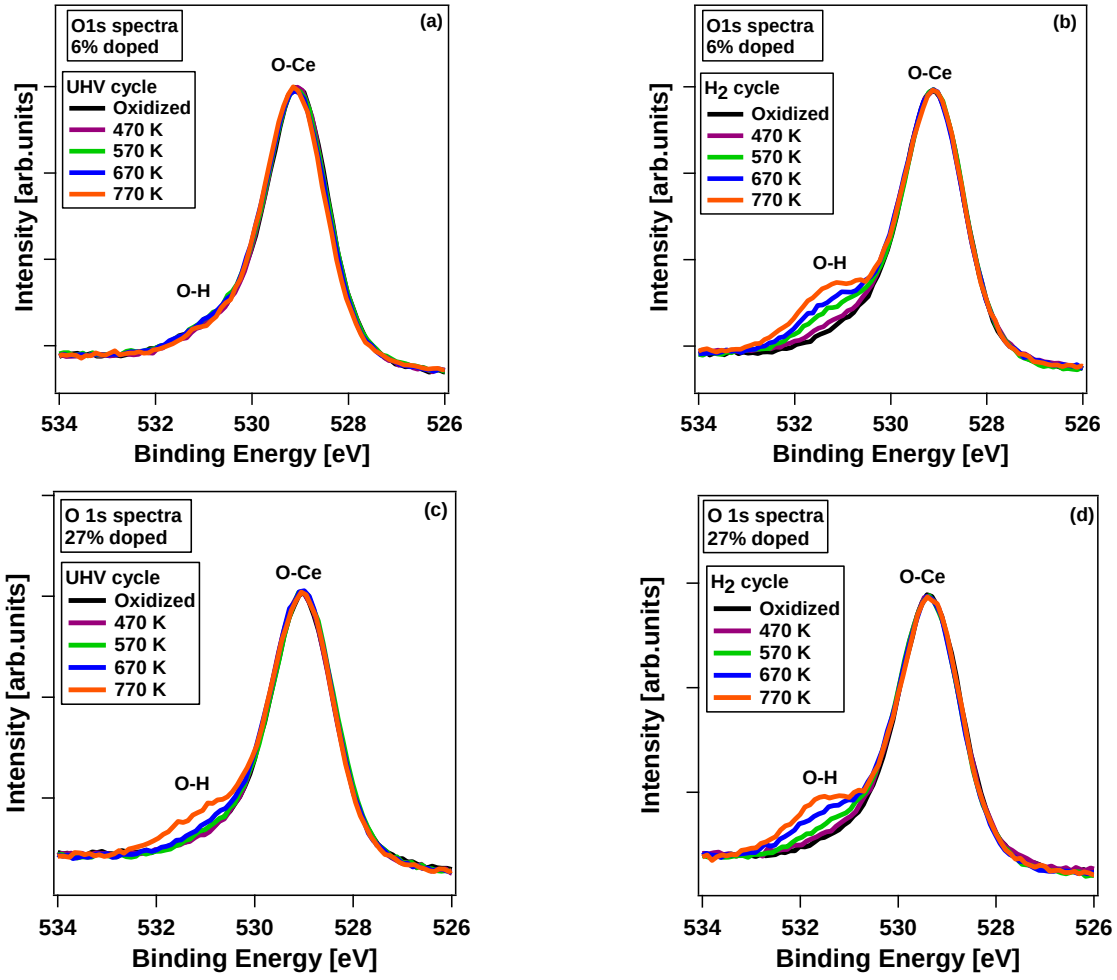

Figure 7. O1s XPS spectra of 6% (a and b) 27% (c and d) doped sample after reduction treatments in UHV and in H_2.

A shoulder is present at 531 eV, i.e., around 2 eV higher binding energy to the main O1s peak, even before the thermal cycles. This shoulder can be ascribed to the adsorption of the OH^- groups on the surface due to

residues present in the background pressure in UHV. UHV treatments showed no significant modifications to the O1s XPS spectra for 6% but an increase in the shoulder of 27% doped samples was observed (figure 7c). The treatments in H_2 have significant effect on the O1s spectra. A non-negligible OH group formation on the surface is quite evident already at 570 K. The shoulder corresponding to OH group starts to increase with increase in the temperature in H_2 as can been seen from figure 7b and 7d. At high temperatures possibly the films dissociate H_2 and OH species are adsorbed on the surface during the cooling process. No traces of molecular water are observed in XPS spectra.

For quantitative analysis, O1s spectra were fitted with two components as explained in chapter 3, section 3.3, to understand the evolution of OH species on the surface. The ratio of areas between O-H peak and O-Ce main component provides quantitative information about the OH group concentration on the surface. In figure 8, the OH/O-Ce area ratios for 6 and 27% doped samples for different temperature treatments in UHV and H_2 are shown in comparison to those on pure CeO_2 films of the same thickness [1]. The first points in the graphs are aligned to zero for a better comparison.

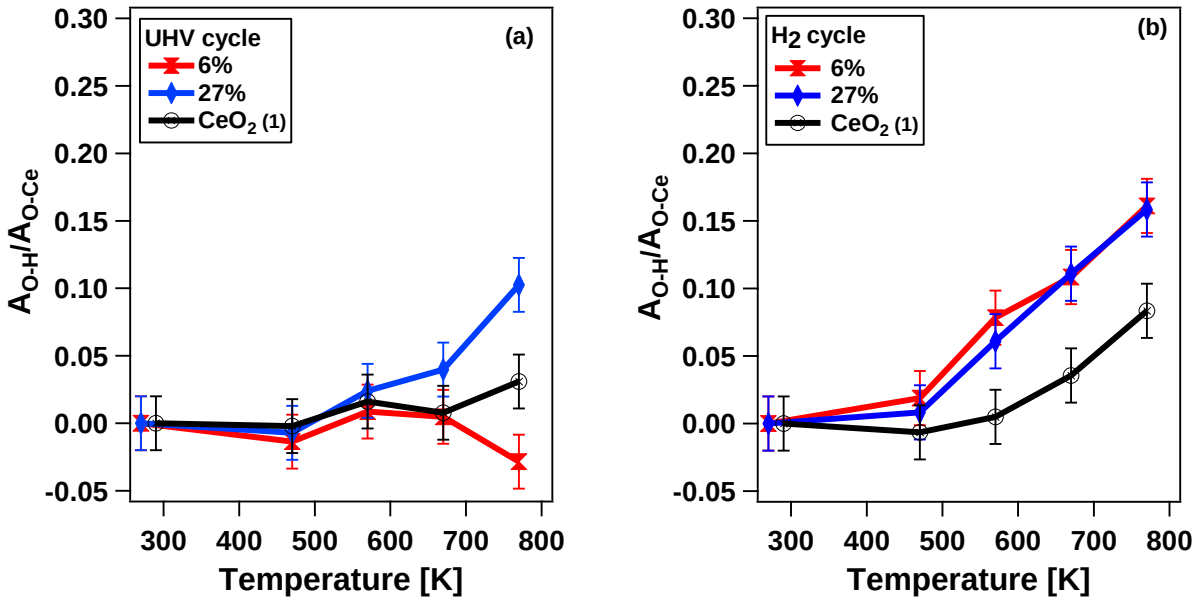

Figure 8. Ratios between areas of O-H and O-Ce peak in UHV (a) and H_2 (b) for 6% and 27% doped films are compared to pure CeO_2 film [1].

The formation of OH species on the sample surface for 6% during thermal treatments in UHV is negligible but for 27% doped sample they are significantly larger at higher temperatures and these behaviors are in accordance with those observed in Ce3d spectra. During the thermal treatments in H_2 a non-negligible concentration of OH species is formed, and it shows a comparable increase on the two Cu-doped films, more pronounced than on the pure ceria film. The observed trends of the increase in OH weight during thermal

cycles in H_2 are in agreement with the DFT calculations [2,4]. As discussed for the theoretical calculations (chapter 3, section 3.5), the Cu-doped samples have higher efficiency in the H_2 dissociation on the surface than pure and Ag:CeO_2 films.

4.1.4 Surface morphology

We have investigated the surface morphology of 6% and 27% doped films with STM at RT to understand any modifications in the surface morphology of the re-oxidized samples performed after thermal reduction treatments in H_2. Figure 9 shows the surface topography for the two samples and height profiles across different cerium oxide lattice planes.

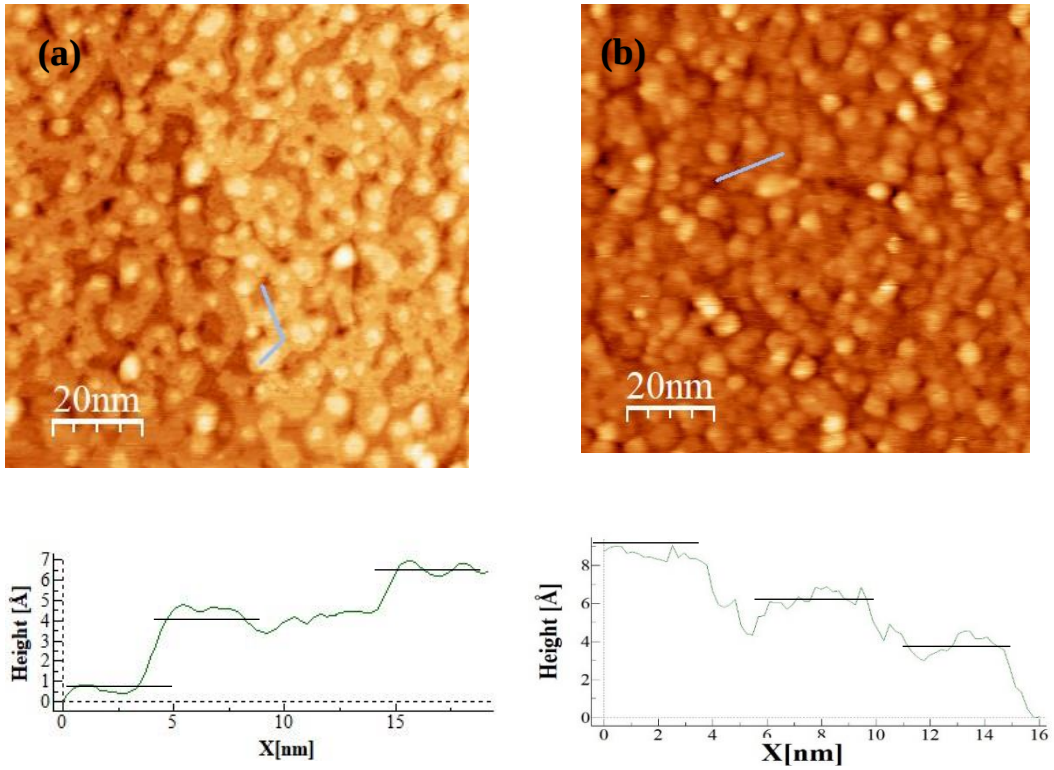

Figure 9. 100×100 nm² STM image of re-oxidized 6% (a) and 27% (b) doped Cu: CeO_2 samples after thermal reduction cycles in H_2 with their respective height profiles.

The surface shows different cerium oxide lattice planes with different contrast levels which corresponds to the different (111) planes of ceria with average interplanar distance of 3 Å (expected is 3.125 Å). The bright features on both sample surfaces correspond to the top plane of cerium and we did not observe any segregation of Cu atoms on the surface in both samples, consistent with the migration to interface of Cu atoms. At the same time no evolution of the surface oxide morphology appears evident, indicating an overall stability of the surface. Attempts to acquire images after H2 treatment have been done but the

quality of the images is scarce due probably to molecular H_2 and water adsorbed and mobile on the surface at RT.

4.2 Buffer layer sample

Since in Cu-doped ceria films we observed the migration of Cu atoms from the surface to the buried interface after thermal treatments, we prepared a sample with a different architecture, shown in figure 10, with a 3 ML thick buffer layer of pure ceria in between the 3 ML thick CeO_2 modified with 3 at.% Cu and the substrate to hinder the migration of the dopant atoms into the bulk.

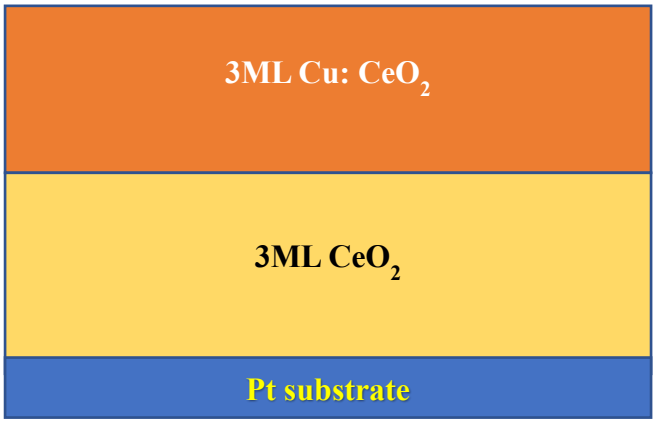

Figure 10. Architecture of the buffer sample with 3% doped Cu: CeO_2 on Pt (111) substrate.

We have followed the same procedure steps to investigate the reactivity of this film. The sample was oxidized at 770 K in O_2, before UHV treatments and then re-oxidized (770 K, O_2) before temperature treatments in H_2.

4.2.1 Cu doping stability

The main goal with the sample here described is to investigate the mobility of the Cu atoms in the sample during and after thermal treatments. The actual doping concentration is 3% in this sample and its variation on the surface estimated by the Cu2p and Ce3d intensity ratio is quite small compared to the 6% doped film discussed in previous section (figure 11), where the actual nominal doping before temperature treatments was 6% and first oxidation reduced it to 3%.This demonstrates that the mobility of the dopant atoms was hindered by the buffer layer or that it was low enough to be stable during the thermal treatments, probably because the less defective undoped film makes the diffusion less efficient.

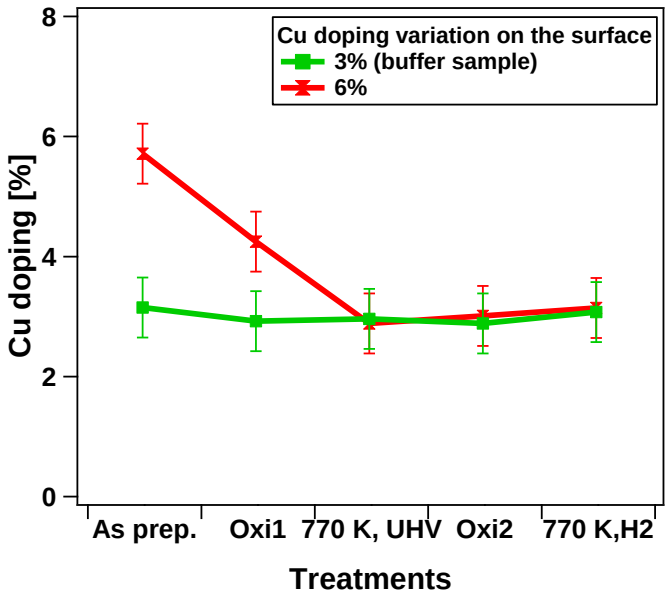

Figure 11. Copper doping concentration [%] variation comparison between 6% film and 3% buffer sample.

4.2.2 Evolution of Ce^{3+} concentration

Ce 3d XPS spectra of the buffer sample were measured after each thermal treatment in both UHV and H_2 at grazing emission angle and are shown in figure 12. Temperature treatments in UHV induced a small modification in the Ce 3d spectra (figure 12(a)). During thermal treatments in H_2, larger modifications in the Ce 3d spectra were evident already at 570 K, as can be seen from the figure 12 (b).

Ce 3d spectra were fitted using the procedure explained in the chapter 3, section 3.2, to understand the evolution of Ce^{3+} concentration during thermal treatments. The evolution of Ce^{3+} ions during thermal treatments in UHV and in H_2 are compared to 6% doped film in figure 13. The Ce^{3+} concentration in the buffer sample during thermal treatments in UHV increases with the temperature. Already at 470 K, 4% Ce^{3+} concentration was observed, and it reached up to 12% at 770 K. This is much higher than the 6% doped sample (6% at 770 K). Thermal treatments in H_2 induced a higher Ce^{3+} concentration and was significant already at 470 K (16%). Ce^{3+} concentration increased quite rapidly with the temperature in the buffer sample and reached up to 37% at 770 K, which is slightly higher than the value for the 6% doped film (35%). The higher reactivity of the buffer sample evident already at lower temperatures can be attribute to the presence of an effective 3 at.% Cu atoms concentration in the topmost part (3 ML) of the bilayer film, compared to a 3 at.% Cu probed by XPS across the whole 6 ML thick film in the initial 6% doped film. This means that the actual dopant concentration on the surface is higher in the buffer sample than in the 6% doped film.

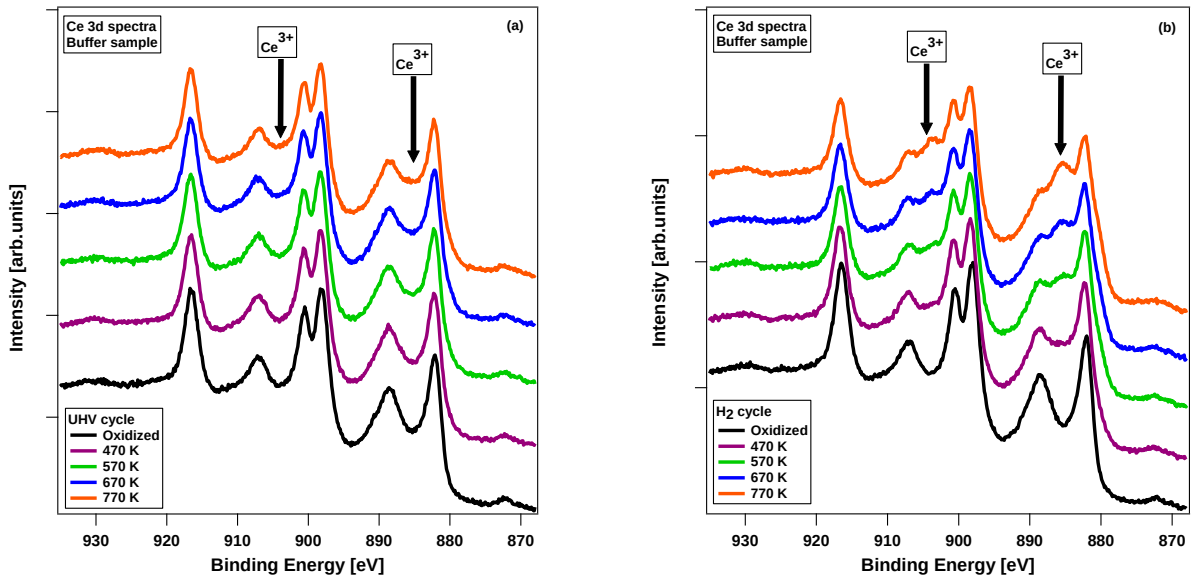

Figure 12: XPS spectra of Ce 3d of the buffer sample after thermal treatments in UHV (a) and H_2 (b).

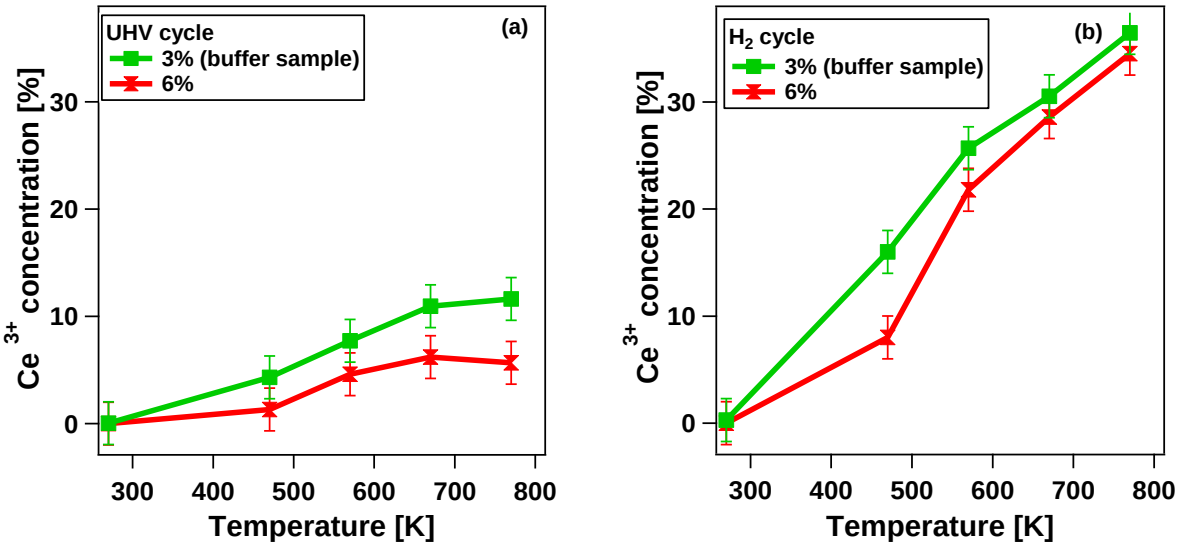

Figure 13. Comparison between the evolution of Ce^{3+} concentration in the buffer sample (3% doped) and 6% doped film in UHV (a) and in H_2 (b) atmospheres.

4.2.3 OH surface adsorption

The modifications to the XPS O 1s spectra after thermal treatments in UHV and in H_2 are illustrated in figure 14. O 1s XPS spectra had an asymmetric shape already before the thermal treatments possibly due to the adsorption of the OH species on the surface from UHV background pressure. Thermal treatments in UHV did not significantly modify the O 1s spectra (figure 14a). On the contrary H_2 thermal treatments

induced a significant modification. The shoulder at 531 eV rises with the increase in the temperature and it is quite intense already at 470 K as shown in figure 14(b).

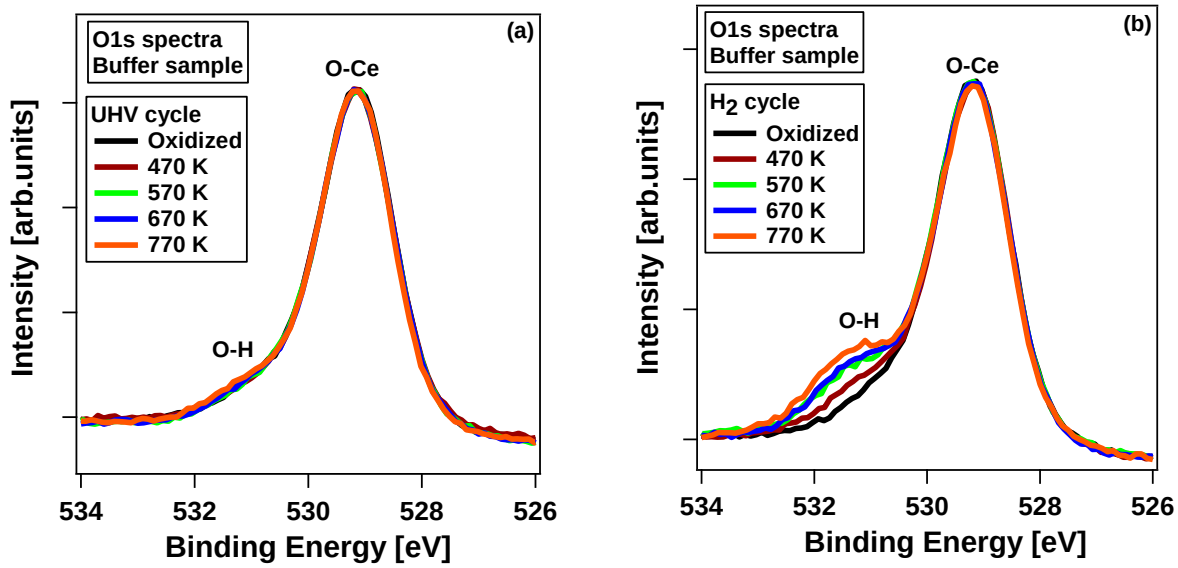

Figure 14. O1s XPS spectra of buffer layer sample after UHV (a) and H_2 (b) treatments.

The evolution of OH species on the surface during thermal treatments in UHV and H_2 as obtained by fitting are shown in figure 15, in comparison with 6% doped film. The first points in the graph are aligned to zero for a better comparison. As observed in the other two films discussed in previous section, the buffer sample also showed negligible modifications in O1s spectra in UHV treatments. As expected, the thermal treatments in H_2 showed a greater modification to O1s spectra indicating a higher concentration of OH species on the surface. However, the overall trend is not significantly different in the two samples, indicating a similar adsorption rate of OH during cooling.

With this architecture we have therefore demonstrated that it was possible to confine the Cu atoms on the topmost layers and slightly increase further the ceria reactivity.

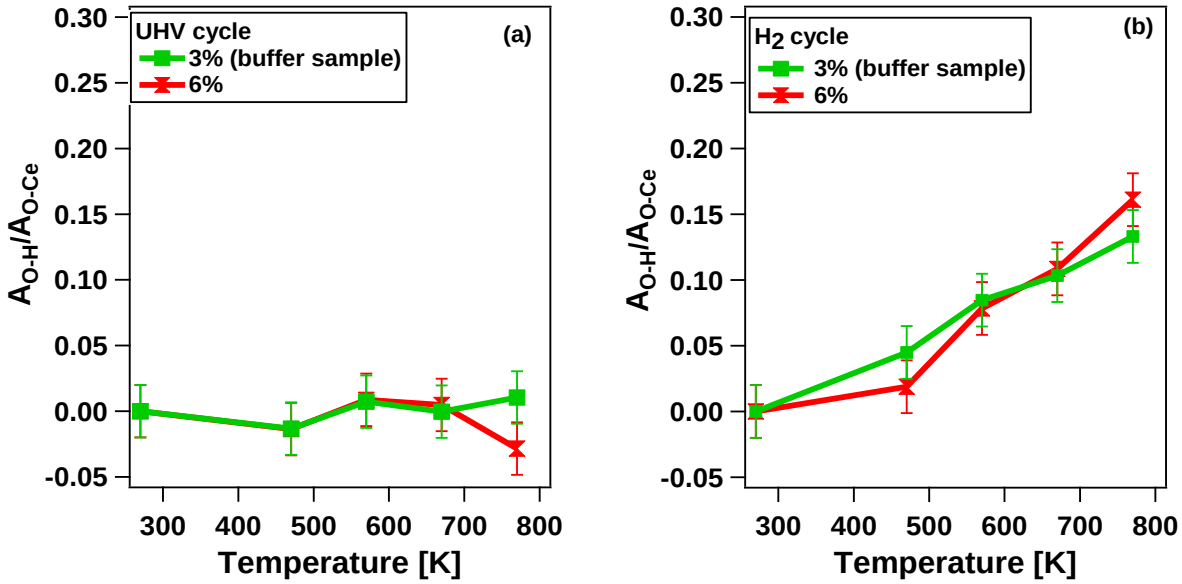

Figure 15. Ratio between areas of O-H and O-Ce peaks for buffer layer sample (3% doped) and 6% doped sample in UHV (a) and H_2 (b) treatments.

4.2.4 Surface morphology

We have taken STM images of the buffer sample at RT after thermal treatments in both UHV and H_2 to verify any changes on the surface morphology, since they can induce changes in the reduction behavior of the sample. In figure 16, an STM image of the re-oxidized buffer layer surface after thermal reduction treatments is shown along with a profile.

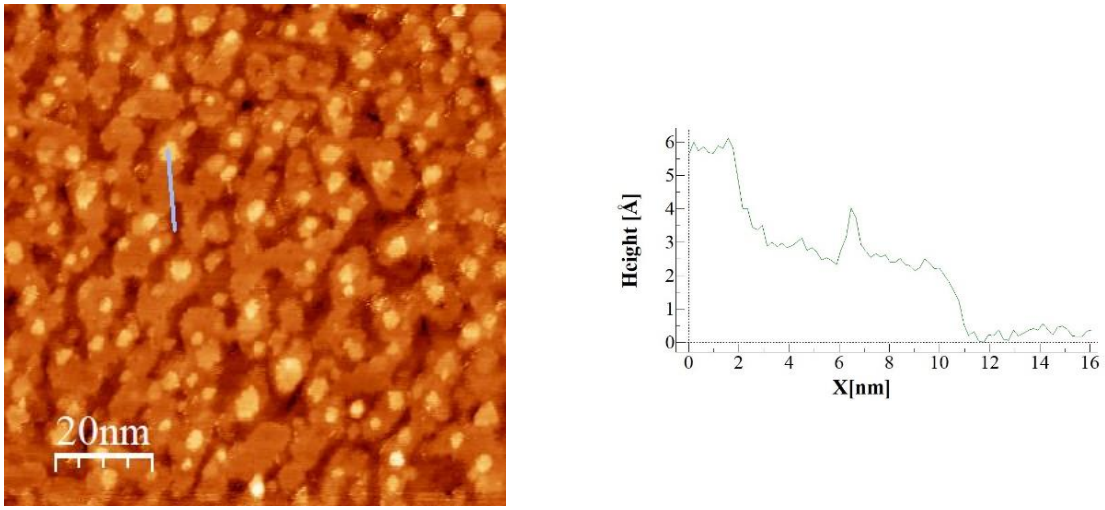

Figure 16. 100×100 nm^2 STM image of 3% doped Cu: CeO_2 buffer layer sample with the respective height profile taken after re-oxidation. Re-oxidation of the sample was performed after thermal reduction cycles.

Also, in this case we can observe several ceria layers exposed, as indicated by the steps in height profile. The top islands have an average size of about 3-7 nm. The fractional coverage exposed from the STM images estimates to be 12, 68 and 20% for top, intermediate and the third layer, respectively. No significant difference between the buffer sample and the previous homogeneously doped films is evident, indicating that from a morphological point of view at the hundred-nm scale the films are almost identical. A minor difference is the smaller fraction of top layer exposed, with a larger intermediate layer fraction. This indicates a modestly higher closure of the film obtained with the buffer layer.

4.3 Dilution of Cu deposited on CeO_2 film

In this section, I will report another way to dilute Cu atoms in the oxide (Cu/ CeO_2 system) by deposition and oxidation of Cu on the oxidized (770 K, O_2) CeO_2 surface (figure 17). Our goal in the study of this new architecture was to understand the behavior of Cu atoms deposited on the already oxidized pure CeO_2 film and determine the effect on its structure and reactivity.

Instead of co-deposition, subsequent deposition method and thermal treatment was employed to prepare the film, as previously reported for the doping of MgO [5]. First, we prepared 6 ML CeO_2 film by evaporating Ce atoms on Pt (111) in O_2 (1 x 10^{-7} mbar). Then the film was oxidized by annealing at 770 K, in O_2 (1 x 10^{-7} mbar) for 15 minutes to improve the crystalline order and complete the oxidation before deposition of Cu atoms. After the oxidation of the film, we deposited 0.2 Å of Cu atoms onto CeO_2 film in UHV and subsequently oxidized to 770 K to dilute Cu. We then followed the same procedure steps that we employed for Cu-doped films to study the reactivity of the film while exposed to H_2.

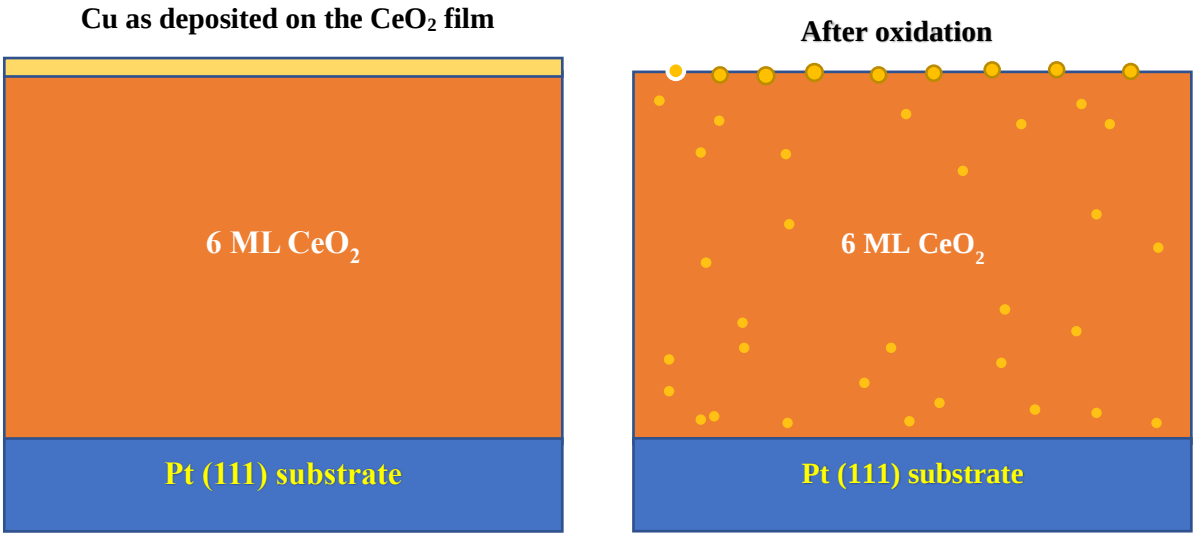

Figure 17. Architecture of the Cu/CeO_2 film prepared in sequential deposition method and after oxidation. Yellow balls represent Cu atoms in the oxide.

STM image acquired at RT after deposition of 0.2 Å of Cu atoms on the surface of CeO_2 annealed at 770 K in O_2 for 15 minutes is shown in figure 18. The deposited Cu atoms on the surface have agglomerated and formed NPs with diameter about 2 nm.

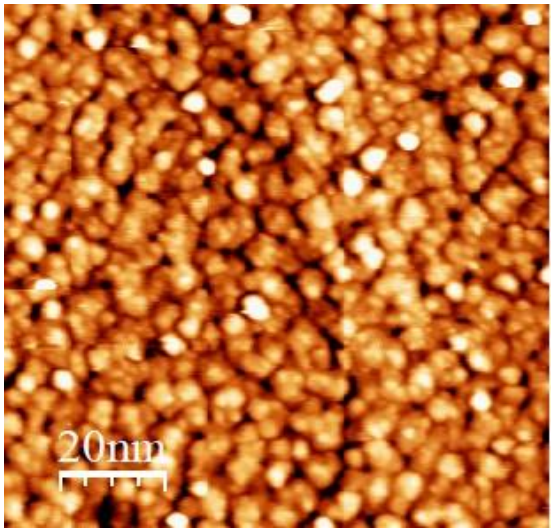

Figure 18. 100×100 nm² STM image of Cu/CeO₂ sample taken after the deposition of Cu atoms on the oxidized CeO₂ surface.

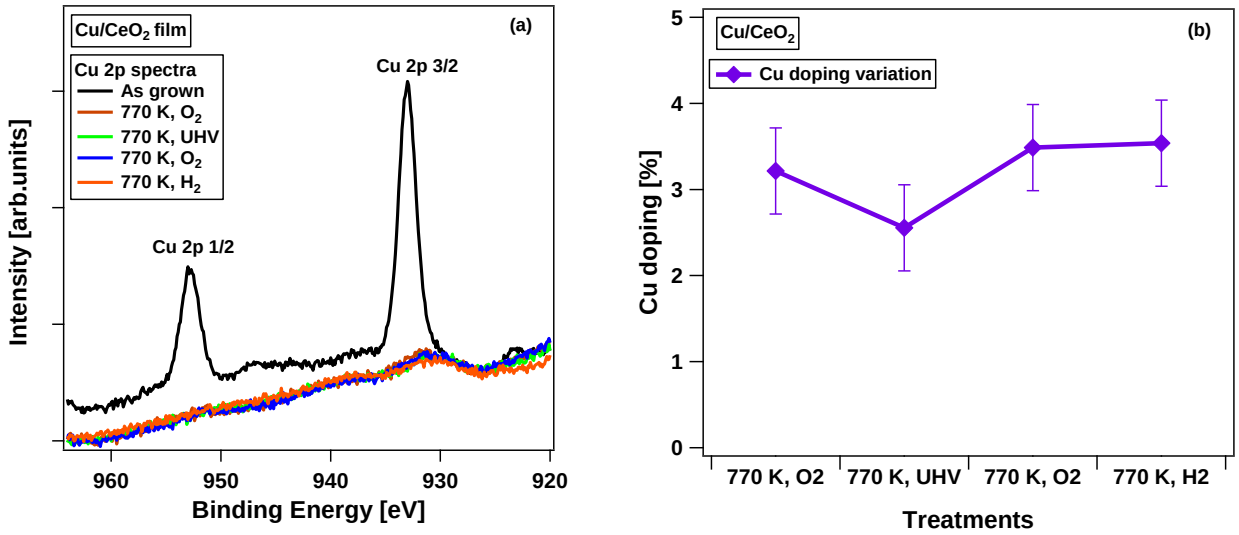

Figure 19. Cu 2p grazing emission spectra of Cu/CeO₂ film taken after each thermal treatment step (a) and the calculated Cu atoms concentration for the respective treatment steps (b) are shown.

Sample was then annealed in O_2 partial pressure (1 x 10^{-7} mbar) for 15 minutes before performing the thermal reduction cycles. Cu 2p XPS spectra acquired after growth and thermal treatments are shown in

figure 19 (a). After the first oxidation, the intensity in the Cu 2p spectra significantly drops and remains constant during the following thermal reduction cycles. The quantitative estimation of the Cu at.% after the oxidation process is shown in figure 19 (b). We can clearly observe that the amount of Cu did not significantly change and remained around 3 at.% during all the reduction cycles, an amount very similar to the one obtained in the doped samples discussed in previous sections. Figure 20 shows the Cu 2p XPS spectra acquired at normal and grazing emission after the oxidation process, where it can be observed that intensity is higher at normal emission, indicating that Cu migrates from the surface into the oxide towards the interface. However, we cannot exclude that part of the Cu atoms are desorbed from the process during the annealing.

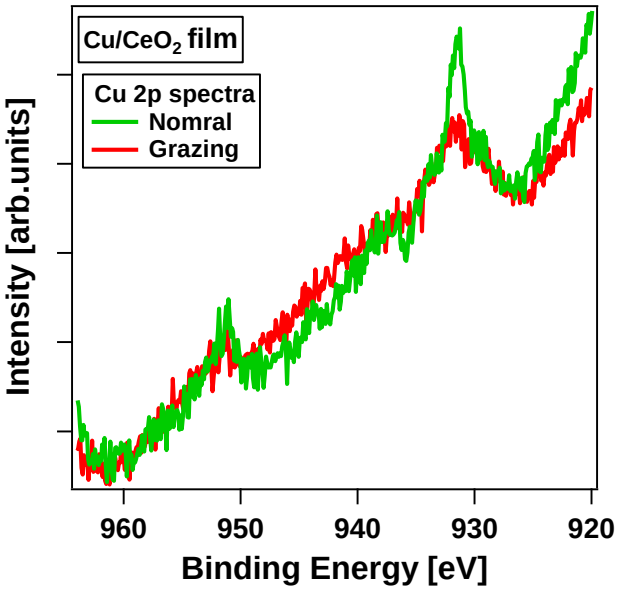

Figure 20. Cu 2p XPS spectra acquired at normal and grazing emission after the first oxidation.

Then temperature treatments of the film were performed both in UHV and in H_2 following the same procedure that was used for Cu-doped films. Ce 3d XPS spectra was taken after each thermal reducing step and the modifications induced in the Ce 3d spectra of the film are shown in figure 21. The modifications induced in the UHV thermal steps (figure21 (a)) are non-negligible. The effect of the temperature on the ceria reduction was clearly observed. But the modifications induced after thermal steps in H_2 are more pronounced. At already 470 K, a clear effect on the Ce 3d can be seen (figure 21(b)).

In figure 22, the evolution of Ce^{3+} ion concentration in the film during each thermal annealing cycle in UHV and H_2 is shown. As can be seen from the figure 22, the increase in Ce^{3+} concentration in the film starts at already 470 K and reaches up to 18% at 770 K in UHV. This film shows a Ce^{3+} concentration in UHV higher than the 6 at.% doped film, and comparable to the 27% doped film (16% at 770 K). In H_2 we

observe significant reduction at already 470 K (26%), which reaches around 47% at 770 K. The Ce^{3+} ion concentration in the film during thermal annealing treatments in H_2 is much higher than for the 27% doped film (36% at 770 K). The higher concentration of Ce^{3+} observed in this sample is probably due to the effect of a higher concentration of Cu atoms on the surface/subsurface as compared to the co-deposited films or to a large surface defectivity left by Cu atoms migration, as it occurs for highly doped CeO_2.

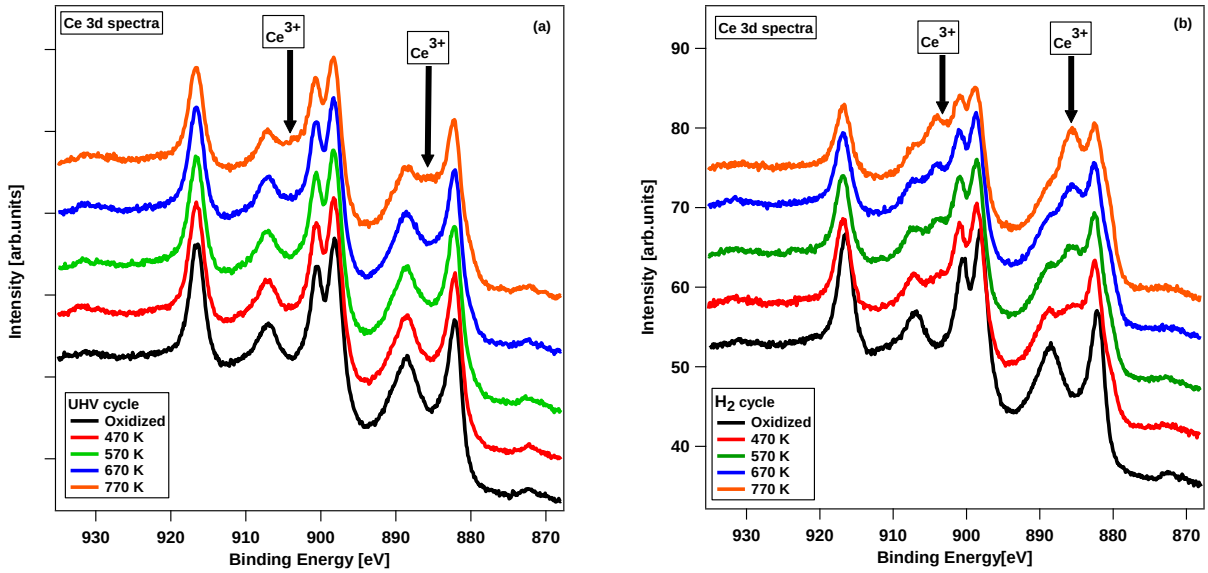

Figure 21. Ce 3d spectra of the Cu/CeO_2 film during thermal annealing treatments in UHV (a) and in H_2 (b).

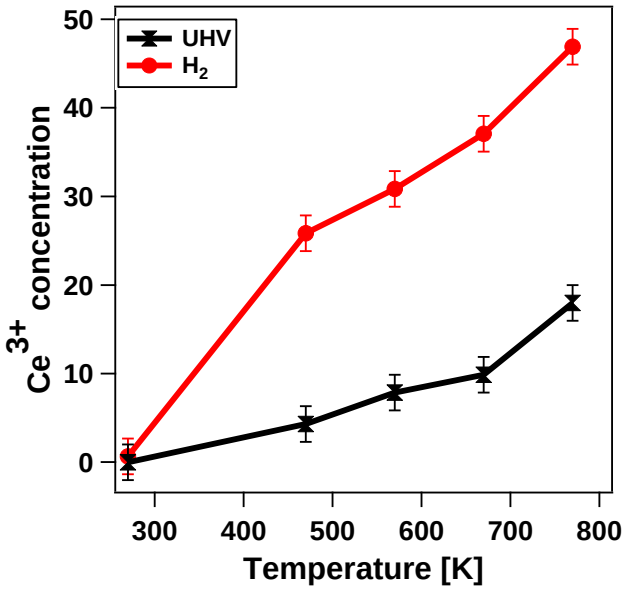

Figure 22. Evolution of Ce^{3+} concentration in Cu/CeO_2 during thermal treatments in UHV and H_2.

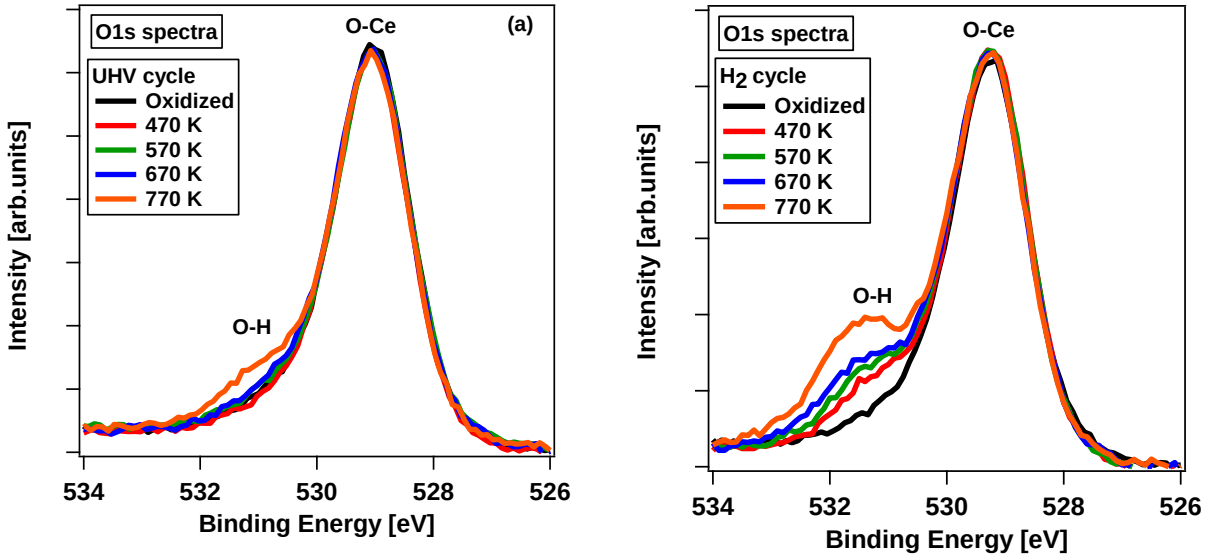

Figure 23. O1s spectra of Cu/CeO₂ film during thermal treatments in UHV (a) and H₂ (b).

The O1s spectra taken after thermal treatments in both UHV and H_2 are shown in figure 23. The modifications in O1s spectra in Cu/CeO_2 film during thermal treatments in UHV is more pronounced than in the case of 6% Cu-doped films. Significant modifications in O1s spectra are observed also during thermal treatments in H_2 (figure 23(b)). The shoulder at 531 eV related to O-H species starts to increase already at 470 K and goes on increasing with the temperature.

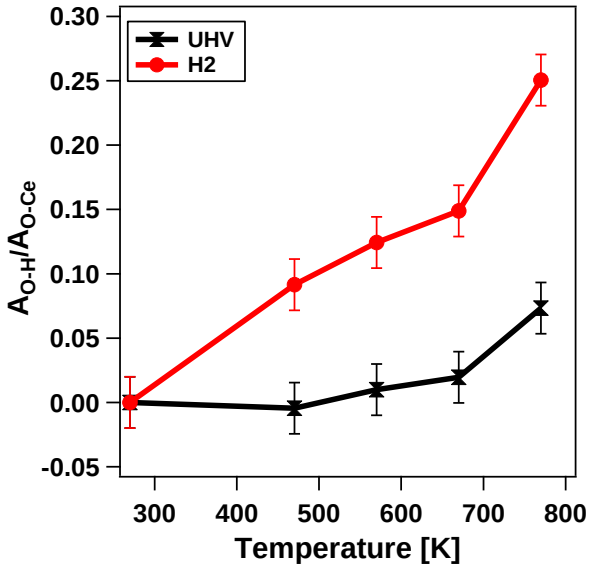

Figure 24. Ratio between areas of O-H and O-Ce peak in UHV and H₂.

Quantitative information about the formation of O-H species on the surface during thermal treatments is evaluated by taking the ratio between areas of O-H component and O-Ce component. In figure 24, the ratio between O-H/O-Ce for Cu/CeO_2 film for both UHV and H_2 conditions for different temperature treatments is shown. O-H group formation on the surface of Cu/CeO_2 film during thermal treatments is non-negligible already in UHV and it increases during H_2 treatments. This signifies the fact that Cu/CeO_2 film is more active in dissociating H_2 than Cu-doped films of comparable dopant concentration at already 470 K. The higher activity of Cu/CeO_2 sample in H_2 dissociation can be ascribed to the higher concentration of Cu atoms and oxide defects in the top layers of the film compared to the doped films.

4.4 Bibliography:

1. Benedetti, S., Righi, G., Luches, P., D'Addato, S., Magri, R., & Selloni, A. (2020). Surface reactivity of Ag-modified ceria to hydrogen: a combined experimental and theoretical investigation. *ACS Applied Materials & Interfaces*, *12*(24), 27682-27690.
2. Righi, G., Magri, R., & Selloni, A. (2019). H2 dissociation on noble metal single atom catalysts adsorbed on and doped into CeO2 (111). *The Journal of Physical Chemistry C*, *123*(15), 9875-9883.
3. Skála, T., Šutara, F., Škoda, M., Prince, K. C., & Matolín, V. (2008). Palladium interaction with CeO2, Sn–Ce–O and Ga–Ce–O layers. *Journal of Physics: Condensed Matter*, *21*(5), 055005.
4. Vikatakavi, A., Benedetti, S., Righi, G., Magri, R., D'Addato, S., Luches, P., & Selloni, A. (2022). Interaction of Hydrogen with Cu-Modified Cerium Oxide Surfaces. *The Journal of Physical Chemistry C*.
5. Stavale, F., Nilius, N., & Freund, H. J. (2012). Cathodoluminescence of near-surface centres in Cr-doped MgO (001) thin films probed by scanning tunnelling microscopy. New Journal of Physics, 14(3), 033006.

Chapter 5

Cu nanoparticles on CeO_2: effect of hydrogen on the stability

In this chapter, I will discuss the interaction between Cu NPs supported on a CeO_2 oxide film grown on Pt (111) and H_2 in UHV conditions at different annealing temperatures. I will also provide details about the chemical and morphological changes on the surface of the films during thermal treatments in UHV and H_2 conditions. The main aim of the present study is to understand the effect of Cu NPs on ceria reduction, on H_2 dissociation on the films and also to understand the stability of Cu NPs during temperature treatments.

Epitaxial CeO_2 films were grown in the UHV chamber on a Pt (111) single crystal substrate employing the e-beam evaporator in partial oxygen pressure (1×10^{-7} mbar) at room temperature. The substrate was prepared by repeated cycles of Ar^+ sputtering (1 keV, 1 μA) and annealing (1040 K) to remove contaminants. A 6 ML thick CeO_2 film was grown by monitoring the evaporation rate through the quartz crystal microbalance. Then the CeO_2 film was oxidized by annealing at 1040 K in oxygen partial pressure of 1×10^{-7} mbar for 15 minutes to improve epitaxial quality and surface morphology. With this higher annealing temperature, a flatter surface is obtained to better observe the formation and modifications of Cu NPs. After the oxidation of the ceria film, nominally 0.2 Å of Cu were deposited on the oxide film using an effusion cell, as determined by the quartz microbalance. No further oxidation treatment was performed on the Cu NPs.

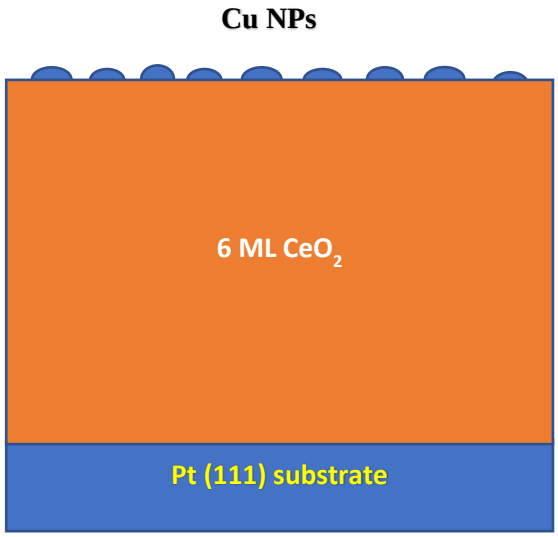

Figure 1: A sketch of Cu NPs grown on a CeO_2 film.

The deposited metal was found to self-assemble into NPs on the oxide surface, as shown in Figure 1. Two Cu NPs/ CeO_2 films of same thickness were prepared for separate investigation in UHV and in H_2

conditions. In situ chemical characterization of the Cu/CeO_2 film was performed using XPS with Al K_α photons and a hemispherical electron analyzer. XPS spectra were measured both at normal and 65° grazing emission to the surface normal after the thermal treatments in both UHV and H_2 conditions at RT. The surface morphology of the films was investigated using STM at RT after each treatment step and the images were processed with the WSxM software [1].

5.1 Cu NPs on CeO_2 and UHV cycle

Figure 2 shows STM image of the surface of the 6 ML CeO_2 film on Pt (111) after oxidation at 1040 K before the Cu NPs deposition and the height profile along the black line in the image. The surface morphology of the CeO_2 film has steps with a height of ~ 3 Å, as shown in figure 2 (right).

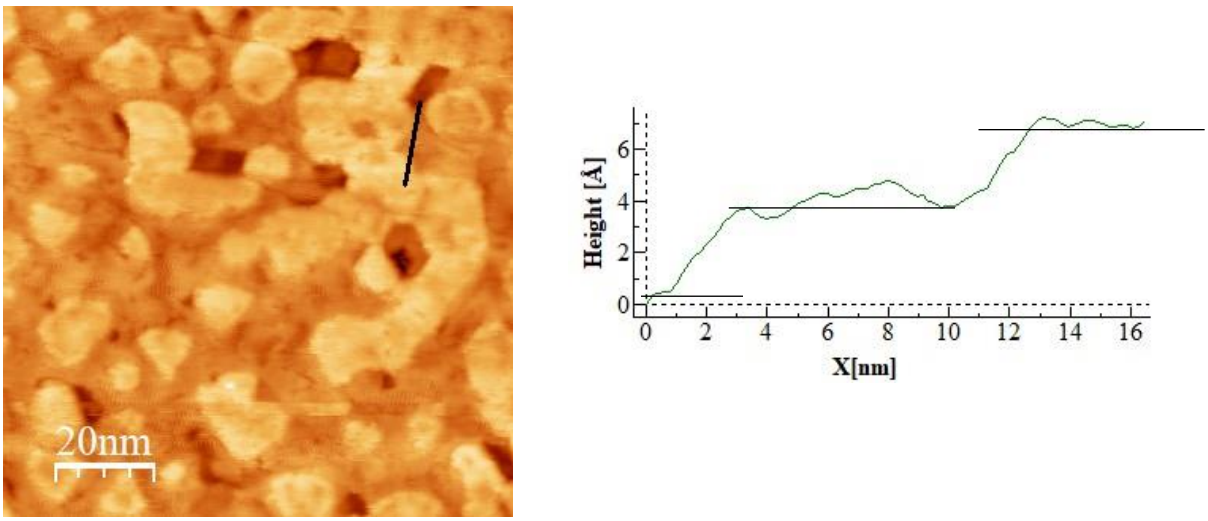

Figure 2: 100×100 nm² STM image of CeO_2 after oxidation and height profile along the black line.

The surface morphology of the sample after deposition of 0.2 Å of Cu atoms on the surface is shown in figure 3 (a). It is evident that the surface of the CeO_2 film is completely covered with Cu NPs with a circular shape and a diameter of the order of approximately 3 nm. In the literature it is shown that at very low Cu coverage the preferential adsorption sites for Cu NPs on CeO_2 surfaces are step edges rather than terraces [2]. In our case, we observed a uniform density of nanoparticles on the surface, consistent with literature results for similar Cu coverages [2]. Agglomeration of Cu nanoparticles was not evident, probably due to the strong interaction between the NPs and the oxide.

We have investigated the effect of temperature treatments on Cu NPs in UHV to understand the stability of the interaction between NPs and the oxide. A strong interaction between Cu atoms and CeO_2 (111) is reported in the literature [2,3]. STM images were acquired at RT after each thermal reduction step in UHV

to investigate the surface modifications (figure 3 (b), (c) and (d)). Annealing cycles were performed for 15 minutes each in UHV and the sample was allowed to cool down to RT before the STM measurements.

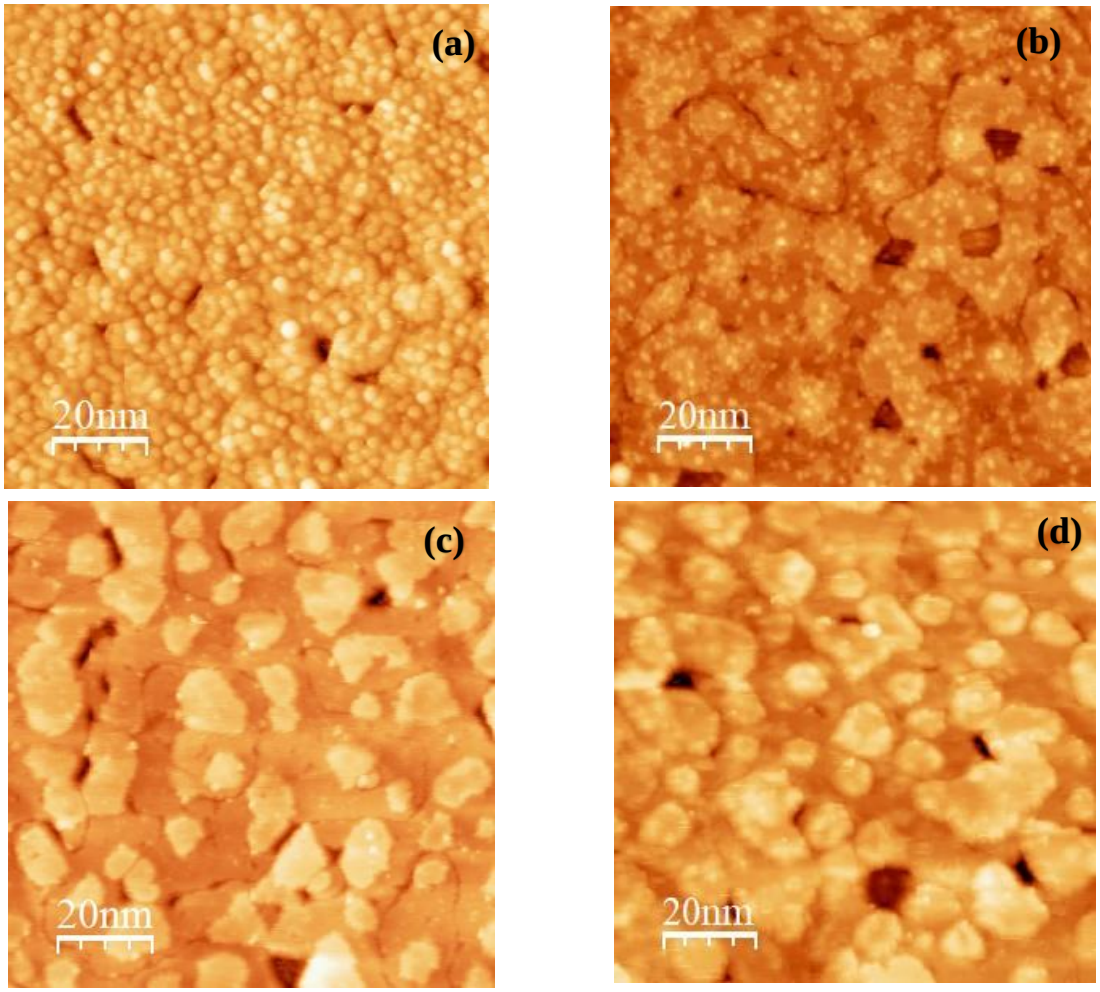

Figure 3: 100×100 nm^2 STM image of Cu NPs/CeO_2 film after growth (a) and after annealing at 370 K (b), 470 K (c) and 570 K (d) in UHV.

Already after heating at 370 K, we observed a significant decrease in the Cu NP density on the surface and the diameter of NPs decreased from ~ 3 nm (as grown) to ~ 1 nm (Figure 3 (b)). As the annealing temperatures were increased, the density of NPs diminished quite rapidly as can be seen from figure 3(c) and 3(d). Cu NPs are hard to detect on the surface after annealing at 570 K, although a small amount of Cu NPs is still visible (figure 3 (d)). The stability of Cu NPs on the CeO_2 surface becomes weaker as we increase the annealing temperature. The annealing temperature and the UHV conditions have played a role on the stability of Cu NPs. In addition to STM measurements, we have also measured Cu 2p XPS spectra to elucidate the effect of annealing treatments on Cu NPs stability. Cu 2p spectra were taken at grazing

emission to increase the surface sensitivity after each thermal treatment. Figure 4 shows the Cu 2p XPS spectra after each thermal treatment in UHV.

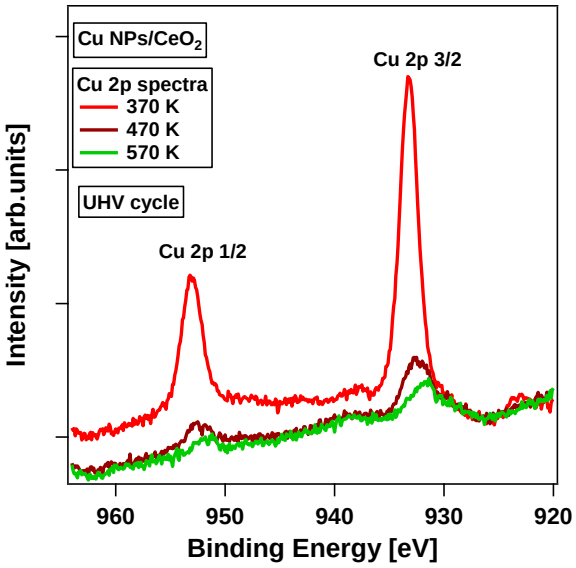

Figure 4: Cu 2p spectra of the Cu NPs/ CeO_2 film after each thermal treatment.

An intensity drop in the Cu 2p spectra is visible after each thermal annealing treatment in UHV (Figure 4). This coincides with the observations of the surface morphology, where the NPs started to disappear after annealing the sample at 470 K. The Cu 2p spectrum acquired after 570 K reveals the presence of only a tiny amount Cu on the surface which is in accordance with STM measurement. The decrease of Cu 2p intensity and the disappearance of the NPs from the surface can either be ascribed to a partial desorption of Cu from the surface with increasing temperature, or to a dissolution of the material within the cerium oxide film. The latter hypothesis is supported by the tendency for Cu to preferentially migrate towards the CeO_2/Pt interface, shown in the previous chapters. However, we cannot neglect a partial evaporation of Cu from the surface during the thermal treatments.

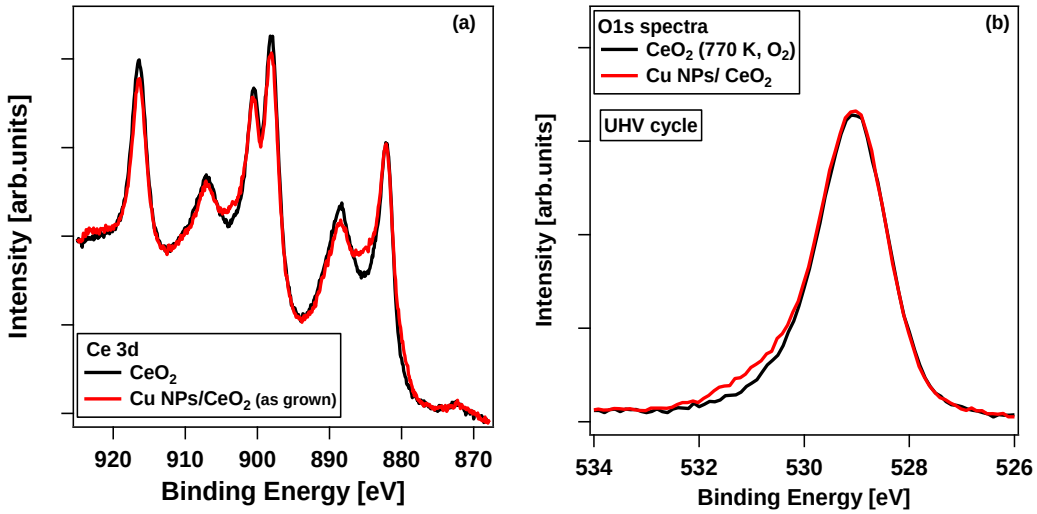

Figure 5: Ce 3d (a) and O 1s (b) normal emission spectra of the CeO_2 film before and after Cu NPs deposition.

XPS spectra of Ce 3d and O 1s regions after the deposition of Cu atoms on CeO_2 surface at normal emission are shown in Figure 5. A partial reduction in Ce was already visible after the deposition of Cu atoms on the CeO_2 surface (figure 5(a)). It is considered that the Cu atoms get positively charged upon deposition and adsorption on the ceria surface [2], due to charge transfer from metal to oxide support. According to the DFT studies [4], the adsorption of Cu on oxygen vacancy transfers charge from Ce to Cu and forms a partially negative Cu and thus oxidation of Ce^{3+} to Ce^{4+} whereas the adsorption of Cu atom on stoichiometric terraces does the opposite. As shown in figure 5 (b), a moderate modification in O 1s spectra of CeO_2 was also observed after the deposition of Cu on the surface with a slight increase of the shoulder at 531 eV, related to OH species. A possible explanation for this could be that Cu atoms induce a partial dissociation of the small amount of H_2 or H_2O present in the chamber background pressure, and a small amount of OH species get absorbed on the surface.

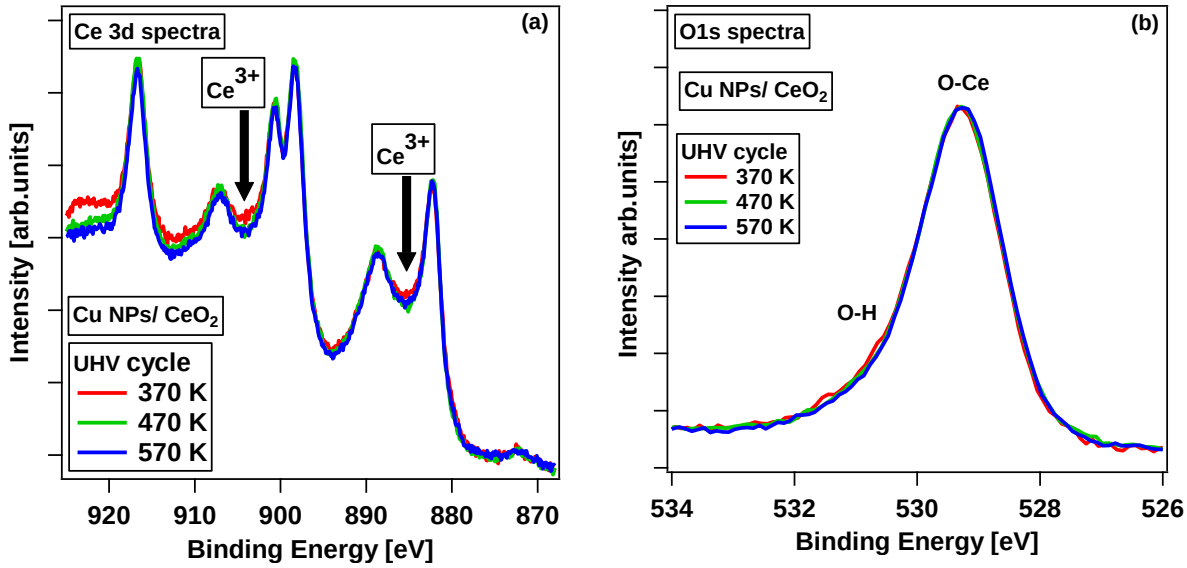

Figure 6: Ce 3d spectra (a) and O1s spectra (b) of Cu NPs/ CeO_2 film after each thermal step in UHV.

The modifications in the Ce 3d and O 1s spectra during temperature treatments were investigated by measuring XPS at grazing emission. The effect of thermal reduction treatments in UHV on Ce 3d and O 1s spectra are shown in figure 6. The modifications induced in the Ce 3d and O 1s spectra were moderate as it can be seen in figure 6 (a) and 6 (b) and show that the modifications undergone by the Cu NPs on top of the ceria during the thermal treatment in UHV do not alter significantly the ceria film itself.

5.2 H_2 cycle

A second CeO_2 film was prepared using exactly the same procedures as for the film used for the UHV cycle and showed the same morphology and stoichiometry as the first one (data not shown). On the second film we performed the thermal annealing treatments in H_2 atmosphere (1×10^{-7} mbar) and each thermal step was kept for 15 minutes. The surface morphology investigation of the film was done at RT using STM. We have investigated the surface morphology of the films at 570 K and 770 K, and the resulting images are shown in figure 7. Unlike the case of the UHV cycle, after the treatment at 570 K the Cu nanoparticles were agglomerated and formed larger NPs of lower density (figure 7 (a)) as compared to the initial situation (Figure 3 (a)). The diameter of the NPs ranged between 4 and 8 nm. When compared to the case UHV treatments where the Cu NPs are hardly visible (figure 3 (d)), the nanoparticles on the surface after H_2 treatment at 570 K have a higher density and they are bigger in diameter. An increase in the annealing temperature from 570 K to 770 K induces a decrease of the Cu NPs size, while the density does not seem to be significantly altered (figure 7 (b)). So, the presence of hydrogen seems to partially stabilize the metallic NPs on the surface, with the decrease in size occurring at significantly higher temperatures than in

the case of the UHV cycle, and agglomeration prevailing at temperatures below the evaporation/incorporation threshold.

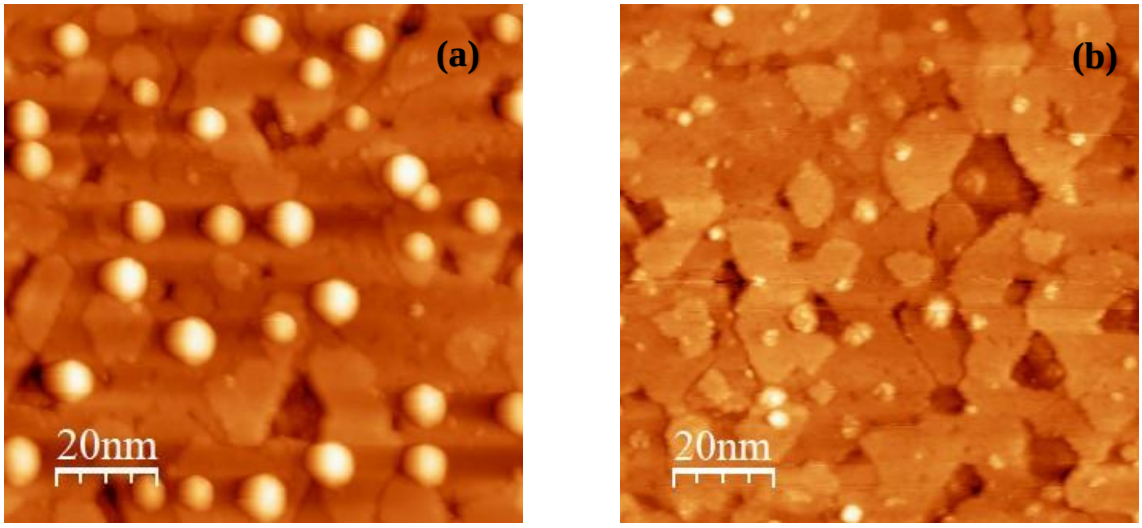

Figure 7: 100×100 nm² STM image of Cu NPs/CeO_2 film taken after treatments in H_2 at 570 K (a) and 770 K (b).

XPS spectra of the Cu 2p region were taken after each thermal treatment in H_2 at grazing emission to understand the stability of Cu NPs and they are presented in figure 8. During the annealing treatments, a decrease in the intensity of Cu 2p spectra was identified.

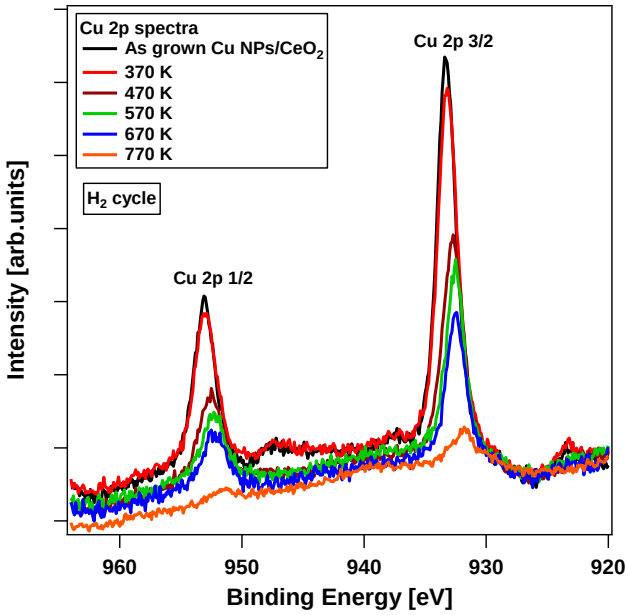

Figure 8: Cu 2p spectra of Cu NPs/CeO_2 taken at grazing emission after each thermal treatment in H_2

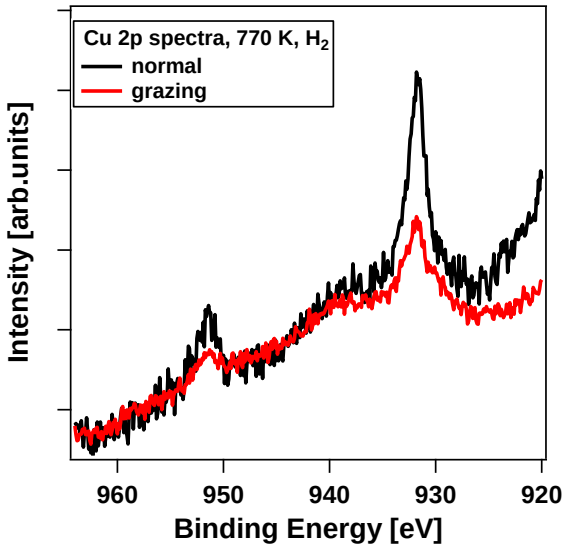

Figure 9: Cu 2p XPS spectra acquired at normal and grazing emission angles after the final step (770 K) of the thermal reduction treatment in H_2.

Figure 9 shows the Cu 2p XPS spectra taken at both normal and grazing emission after the final step (770 K) of the thermal treatment in H_2. The intensity of the Cu line is significantly higher at normal emission than at grazing emission. This evidence confirms the tendency of Cu to migrate towards the bulk of the oxide film, and eventually to the interface with Pt, also when the material is in the form of NPs with nanometric size.

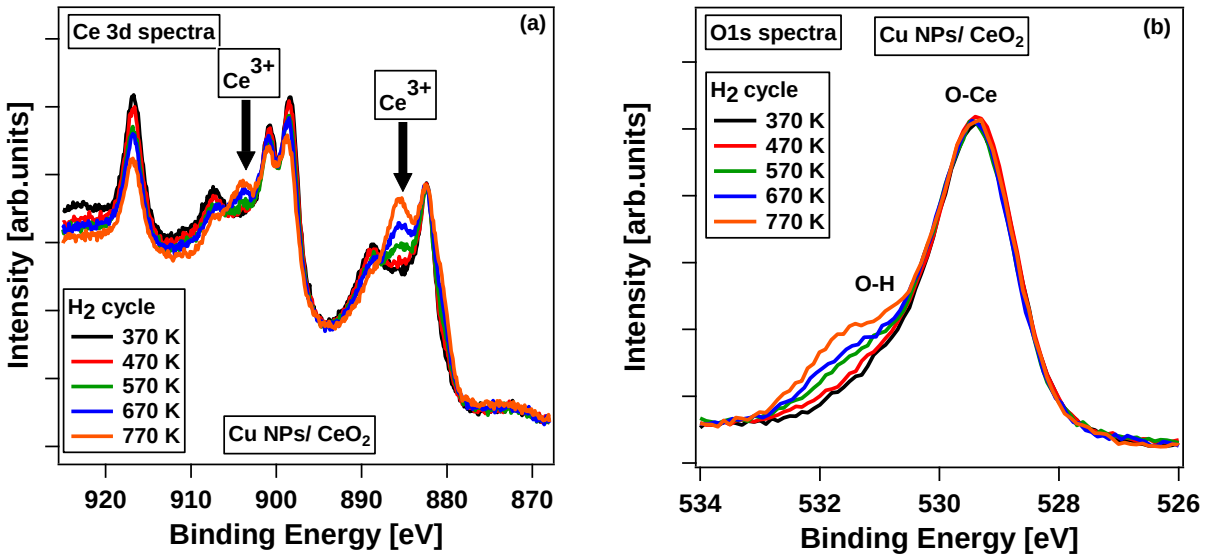

Figure 10: XPS grazing emission spectra of Ce 3d (a) and O1s (b) after each thermal treatment in H_2

XPS spectra were measured for Ce 3d and O 1s regions after each treatment step to understand any modifications induced during annealing treatments in H_2. The acquired spectra are shown in figure 10. After the deposition of Cu NPs on CeO_2, we observed a partial reduction of Ce as in the case of UHV cycle. A significant reduction was observed in the case of H_2 thermal reduction treatments (figure 10 (a)). Non-negligible modifications were also observed in O 1s XPS spectra after thermal treatments in H_2 (figure 10 (b)). A shoulder at 531 eV, ascribed to OH species, was already present after the deposition of Cu atoms on the surface and it increases with the annealing temperature. The shoulder increases in intensity with increasing temperature in H_2, due to the increasingly more efficient dissociation of the molecule on the sample surface.

5.3 Quantitative analysis

The Ce 3d and O 1s spectra acquired at each step of the UHV and H_2 cycles were fit using the procedures described in previous chapters to have quantitative information on the evolution of the sample surface.

5.3.1 Evolution of Ce^{3+} on the surface

The evolution of Ce^{3+} ions in the case of UHV and H_2 cycles are shown in figure 11. Thermal treatments were stopped after 570 K in the case of UHV, due to the almost complete disappearance of Cu NPs from the surface. In H_2 case, we could still observe Cu NPs on the surface at that temperature, so we have continued to investigate the response of the system up to 770 K. At the start of both UHV and H_2 cycles, the film was already mildly reduced due to some charge transfer between Cu NPs and CeO_2. The increase of Ce^{3+} concentration in the case of UHV is negligible, while for the H_2 cycle it grows almost linearly. As in the case of Cu-doped ceria discussed in the previous chapters, the observed increase is probably due to both dissociative adsorption of hydrogen on the surface and/or to water formation and desorption.

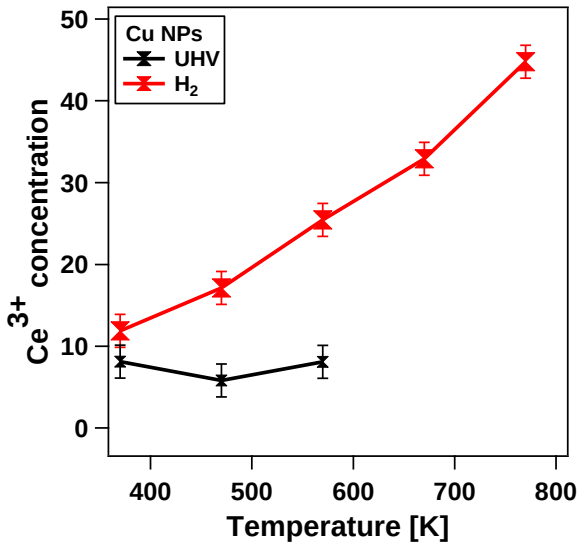

Figure 11: Evolution of Ce^{3+} concentration on the surface of Cu NPs/ CeO_2 films with UHV and H_2 thermal treatments.

After the deposition of Cu NPs 14% of Ce ions were found to be already reduced, while at 770 K the Ce^{3+} ions concentration reaches the value of 44%. So, the actual effect of H_2 thermal treatments on the evolution of Ce^{3+} ions on the Cu NPs/CeO_2 surface evaluated as the difference between the initial and final values of Ce^{3+} concentration 30% is comparable to 6 at.% Cu:CeO_2 sample (34%) as shown in chapter 3. Even though a large quantity of Cu NPs were lost from the surface during thermal treatments, the Cu NPs remaining on the surface/subsurface are active in reducing the ceria film in H_2 cycle.

5.3.2 OH adsorption on the surface

Adsorption of H atoms coming from the dissociation of the H_2 molecule on the surface forms O-H bonds with surface O atoms. The evolution of the concentration of O-H species on the surface was estimated by fitting O1s spectra using the using the procedure explained in chapter 3, section 3.3. Figure 12 reports the ratio between areas of O-H and O-Ce components of O 1s spectra at the different steps of the thermal treatments in UHV and in H_2. The ratio is more or less constant during the UHV cycle, while it shows a moderate increase in H_2. The O-H weight reached the maximum value of approximately 35% at 770 K. But already at 370 K, the weight of O-H species was 21%. We compared the difference between initial and final OH weight finding a value approximately 14% both for Cu NPs/CeO_2 and 6% Cu:CeO_2 [5]. This shows that the Cu NPs have similar effect as 6% Cu:CeO_2 on the H_2 dissociation.

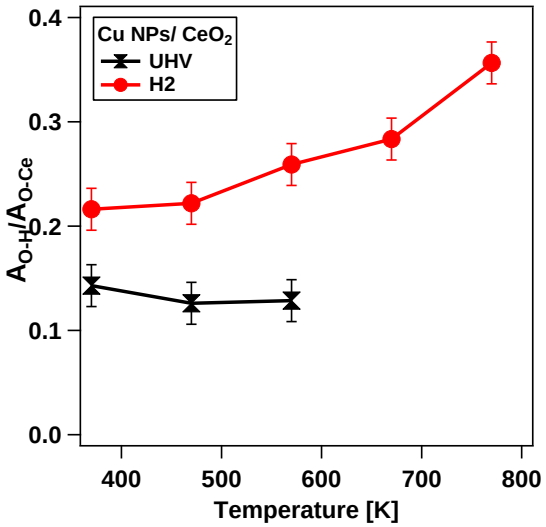

Figure 12: Ratio between areas of O-H and O-Ce peaks in Cu NPs/ CeO_2 film after thermal treatments in UHV and H_2.

5.4 Bibliography:

1. Horcas, I., Fernández, R., Gomez-Rodriguez, J. M., Colchero, J. W. S. X., Gómez-Herrero, J. W. S. X. M., & Baro, A. M. (2007). WSXM: A software for scanning probe microscopy and a tool for nanotechnology. *Review of Scientific Instruments*, *78*(1), 013705.
2. Li, G., Hu, S., Xu, Q., & Zhu, J. (2019). Interaction between Cu Nanoparticles and CeO2 (111) Film Surfaces. *The Journal of Physical Chemistry C*, *123*(38), 23563-23571.
3. Tang, Y., Zhang, H., Cui, L., Ouyang, C., Shi, S., Tang, W., ... & Chen, L. (2012). Electronic states of metal (Cu, Ag, Au) atom on CeO2 (1 1 1) surface: The role of local structural distortion. *Journal of Power Sources*, *197*, 28-37.
4. Szabová, L., Skála, T., Matolínová, I., Fabris, S., Camellone, M. F., & Matolín, V. (2013). Copper-ceria interaction: A combined photoemission and DFT study. *Applied Surface Science*, *267*, 12-16.
5. Vikatakavi, A., Benedetti, S., Righi, G., Magri, R., D'Addato, S., Luches, P., & Selloni, A. (2022). Interaction of Hydrogen with Cu-Modified Cerium Oxide Surfaces. *The Journal of Physical Chemistry C*.

Chapter 6

Ambient pressure NEXAFS on Cu:CeO_2/ MgO

To obtain a more accurate understanding of the interaction between Cu:CeO_2 and H_2, the system was investigated by Near Edge X-ray Absorption Spectroscopy (NEXAFS) in ambient H_2 pressure at APE-HE beamline of the ELETTRA synchrotron in Trieste. For this purpose, we have chosen to support the film on MgO substrates, inert towards H_2 dissociation and significantly less critical than Pt. The samples were grown by MBE in the SESAMO laboratories and preliminarily characterized by XPS in H_2 pressure compatible with UHV. In the first part of this chapter, I will describe the interaction between 6 ML CeO_2 modified with 5% Cu atoms in H_2 and UHV conditions. The second part of this chapter will describe and discuss the NEXAFS experiment performed on 5 nm Cu: CeO_2 films at ambient hydrogen pressure. The main objective was to understand the modifications of the chemical state of both Ce and Cu (dopant) atoms during thermal reduction cycles in real operating conditions. Also, to understand the role of copper atoms in the reduction of Ce atoms during interaction with H_2 and, most importantly, on the activation of H_2 dissociation.

6.1 XPS study of Cu:CeO_2/ MgO films

In this section, I discuss the experimental results obtained by XPS on 6 ML Cu: CeO_2 modified with 5% concentration of Cu atoms in the SESAMO laboratory, Modena. We prepared the sample exploiting the same growth methods as described for the Cu doped CeO_2 samples in previous chapters. An MgO(001) single crystal was used as a support. MgO was heated at 770 K for 10 minutes to remove the surface contaminants. The Cu-doped CeO_2 film was grown and subsequently oxidized by annealing at 770 K in O_2 partial pressure of 1 x 10^{-7} mbar. Thermal treatments in both UHV and in H_2 (1x10^{-7} mbar) were performed after oxidation. The same annealing temperatures as in previous chapters were used to treat the film (470 K, 570 K, 670 K and 770 K). After each thermal treatment, the sample was cooled down to RT and XPS spectra of Ce 3d, O 1s, and Cu 2p regions were acquired at grazing emission angle.

6.1.1 Evolution of Ce^{3+} ion concentration

Figure 1 shows Ce3d spectra after the thermal treatments in UHV and in H_2 at different temperatures. Due to the insulating nature of the substrate, we observed a rigid shift in the binding energy due to charging, therefore the spectra shown in figure 1 are shifted to align with the reference (Ce 3d on Pt).

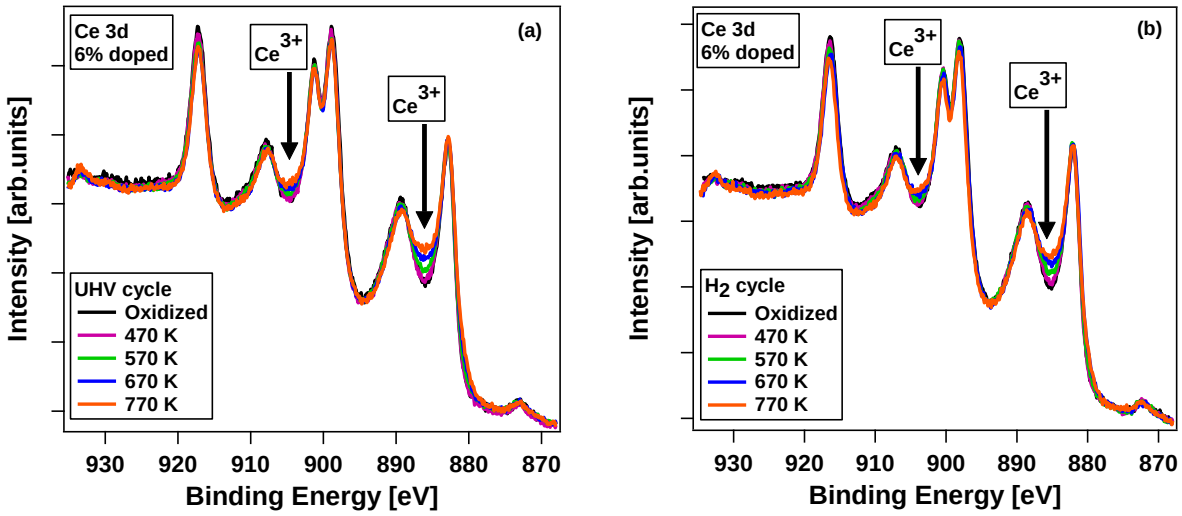

Figure 1: XPS spectra of Ce 3d regions acquired after thermal treatments in UHV (a) and in H_2 (b).

The modifications in the Ce 3d spectra in UHV (Figure 1 (a)) are small but non-negligible, comparable to the Cu-modified films grown on Pt. Surprisingly, also the thermal annealing treatments in H_2 (Figure 1 (b)) induced only minor modifications to the Ce 3d spectra.

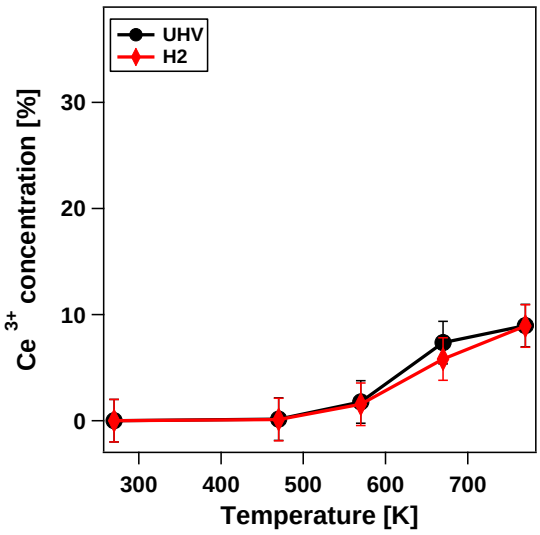

Figure 2: Evolution of the concentration of Ce^{3+} ions after thermal treatments in UHV and in H_2.

Ce 3d spectra were fitted with the procedure described by Skala et al. [1] to understand the evolution of the concentration of Ce^{3+} and Ce^{4+} ions during the thermal treatments. The results are shown in figure 2. Ce^{3+} ion concentration on the surface of the film during UHV and H_2 thermal treatments increases slowly and reaches up to 9% at 770 K in both cases. However, pure CeO_2 film grown on Pt (111) film has been reported to exhibit 18% Ce^{3+} concentration in H_2 at 770 K [2], which is two times higher than on the Cu: CeO_2 film

grown on MgO. Also, the 6% and 27% Cu: CeO_2 films grown on Pt showed a much higher concentration of Ce^{3+} ions after the full thermal treatment in H_2 (35 and 36% respectively, chapter 3 and 4) [3]. In order to exclude a possible role of Pt on the H_2 dissociation, we have simultaneously grown two Cu: CeO_2 films, one on a Pt and one on an MgO substrate, which were mounted in close proximity on the sample holder. The reduction treatments were performed in H_2. The results obtained on the two substrates (Pt and MgO) were similar to their individual counterparts. These results indicated that the direct effect of the Pt substrate on H_2 dissociation is negligible, otherwise the dissociated hydrogen would have interacted with the film grown on the close MgO substrate as well. So, we believe that the nature of the bonding between MgO substrate and Cu-modified ceria film affected the results obtained so far, that leads to a reduced mobility of the Ce, O and Mg atoms on the surface compared to those on platinum. Additionally, the oxygen diffusion from the MgO substrate into the CeO_2 is not possible as the O atoms are strongly bound to Mg. The LEED taken after the oxidation of the films grown on Pt is shown in figure 3. We did not observe any LEED pattern in the case of film on MgO, whereas on Pt crystalline pattern is observed. So, the films grown on Pt is in (111) orientation whereas on MgO are polycrystalline. Based on this, we would expect a higher reducibility on MgO, exposing different facets and being more defective. So, we can also exclude the effect of the different crystallinity of the substrate on the reducibility of the films.

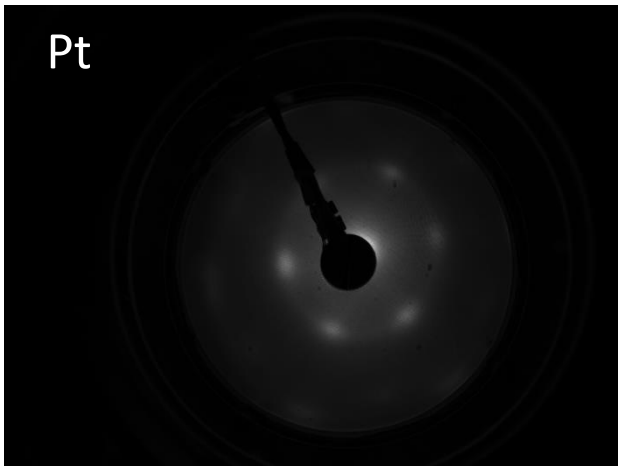

Figure 3: LEED image taken after oxidation of Cu:CeO_2 films grown on Pt.

6.1.2 Modifications to the O 1s spectra

We also acquired O 1s region spectra after each treatment to understand the impact of temperature and the reduction environment on the surface oxygen atoms, in particular to collect information on the formation of surface hydroxyl groups (O-H) during the interaction with H_2. The O 1s XPS spectra, acquired after each thermal step in UHV and in H_2 at grazing emission angle, are shown in figure 4. As in the case of Ce 3d, O 1s spectra in figure 4 were aligned to the reference position (O1s on CeO_2/Pt).

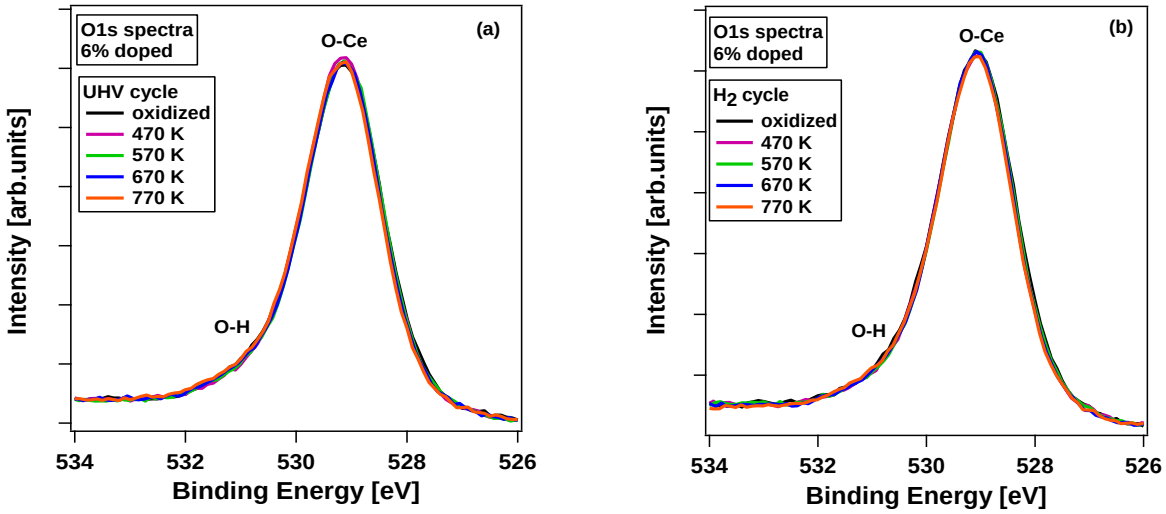

Figure 4: O1s spectra acquired after each thermal treatment step in UHV (a) and in H_2 (b).

As shown in figure 4, we observed no significant modifications to the O1s spectra after thermal treatments in both UHV and in H_2, which indicates that the concentration of hydroxyl groups on the surface does not change with the treatments. Hence, we can deduce that the H_2 dissociation on this film was lower compared to the films grown on Pt substrate. As a result, the Ce^{3+} concentration was comparably smaller in H_2 than in the samples grown on Pt.

6.1.3 Cu dopant stability

We have also measured Cu 2p spectra at both normal and grazing emissions to understand the stability of the dopant atoms in the oxide during thermal treatments.

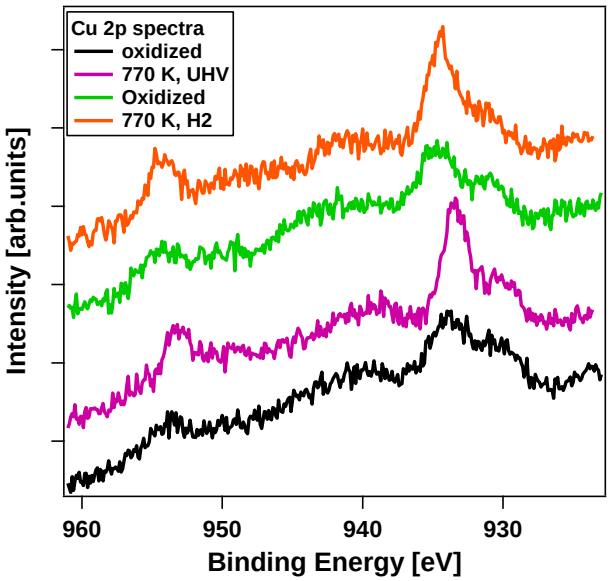

Figure 5: Cu 2p XPS spectra acquired at grazing emission angle after different treatments.

XPS spectra of the Cu 2p region acquired at grazing emission after oxidation (ann. 770 K in O_2), after annealing at 770 K in UHV and in H_2 are shown in Figure 5. Relevant modifications to the Cu 2p spectra after different treatments are clearly visible. We calculated the Cu dopant concentration as explained in Chapter 3. The Cu dopant concentration calculated after each treatment did not change significantly. Also, the normal and grazing spectra behavior are quite comparable indicating that Cu atoms are homogeneously diluted in the film and have a negligible mobility during the treatments, at variance with the case of the Pt support. However, the shape of the Cu2p line changes substantially, with a shift at lower binding energy and a narrowing of the line after annealing in reducing environment, in a reversible way.

Obtaining quantitative information on the changes in the oxidation state of the Cu atoms during thermal treatments from the analysis of XPS spectra was not straightforward due to the low concentration of Cu atoms in the film and to the complexity of Cu 2p spectra, that does not allow a simple and clear deconvolution. The complexity of the Cu 2p spectra arises from the overlapping binding energies of Cu^0 and Cu^{1+} and also due to the shake-up structures for Cu^{2+} species. To overcome this problem, we decided to exploit the NEXAFS technique to investigate the evolution of the oxidation state of both Ce and Cu atoms in Cu: CeO_2/MgO film during thermal treatments in H_2, exploiting at the same time the possibility to have ambient pressure of the gas during the analysis, in conditions similar to real operating catalysts. Synchrotron radiation was used as the source at APE-HE beamline, Elettra, Trieste.

6.2 Ambient pressure NEXAFS study on Cu:CeO_2/ MgO films

We studied the evolution of the oxidation states in Ce and Cu atoms during thermal treatments at ambient pressures in a mixed flux of He and H_2 using ambient pressure NEXAFS exploiting synchrotron radiation at APE-HE beamline of the ELETTRA, Trieste. We prepared 4 samples of 5 nm CeO_2 films in the SESAMo laboratory as shown in table 1, using the procedure employed for doped films. All the samples were grown on MgO(001) single crystals. All the films were transported in a nitrogen filled box to protect the samples from contamination.

Sample	Doping
CeO_2	-
Cu: CeO_2	5%
Cu: CeO_2	14%
Fe: CeO_2	6%

Table 1: 5 nm thick CeO_2 samples with different dopant concentrations used for in ambient pressure NEXAFS studies.

NEXAFS in the soft X-ray regime at ambient pressure was performed in the reaction cell described in Chapter 2. Total electron yield (TEY) mode was used for XAS detection by probing the drain current from the membrane. XAS from Ce $M_{4,5}$-edge originates from electron transitions from Ce $3d_{3/2}$ and Ce $3d_{5/2}$ core levels to the unoccupied 4f electronic levels and thus it contains information about the 4f level orbital occupancy [4]. To have information on possible changes of the oxidation states of the dopants, NEXAFS spectra at the Cu $L_{2,3}$ and Fe $L_{2,3}$ edges were acquired. The samples were loaded in the reaction cell, in the APE-HE instrument, consisting of a gas (O_2, H_2, He) delivery system and temperature control systems. Calibrated mass flow controllers were used to monitor the gas flow in the reaction cell. All the experiments were performed in gas atmosphere at ambient pressure (1 bar). A voltage up to 100 V was applied between sample and membrane in order to increase the collection of the electrons.

As a first step, the samples were oxidized in 10 sccm O_2/40 sccm He flux by keeping the sample temperature at 620 K for 15 minutes. The sample was cooled down to RT in He atmosphere and XAS was performed to record the required edge (Ce $M_{4,5}$, Cu $L_{2,3}$ and Fe $L_{2,3}$) in He atmosphere. Then the reduction thermal treatments in H_2 (2 sccm)/He (48 sccm) mixture for undoped, 5% Cu and 14% Cu:CeO_2, 6% Fe:CeO_2 films were performed by increasing the temperature up to 620 K and Ce $M_{4,5}$ and Cu $L_{2,3}$ or Fe $L_{2,3}$ spectra were measured every 10° C . Only for the undoped and for the 14% Cu:CeO_2 samples the NEXAFS spectra were also acquired during thermal treatments in pure He (50 sccm) after re-oxidation of the samples to understand the role of temperature in inert atmosphere on the chemical state of Ce and dopant atoms (Cu) during

annealing. From the comparison we can isolate the effect of only H_2 on the chemical state evolution of the film. During the thermal annealing treatments, we have also recorded the gas chromatography (GC) spectrum to gain the information about the reaction products.

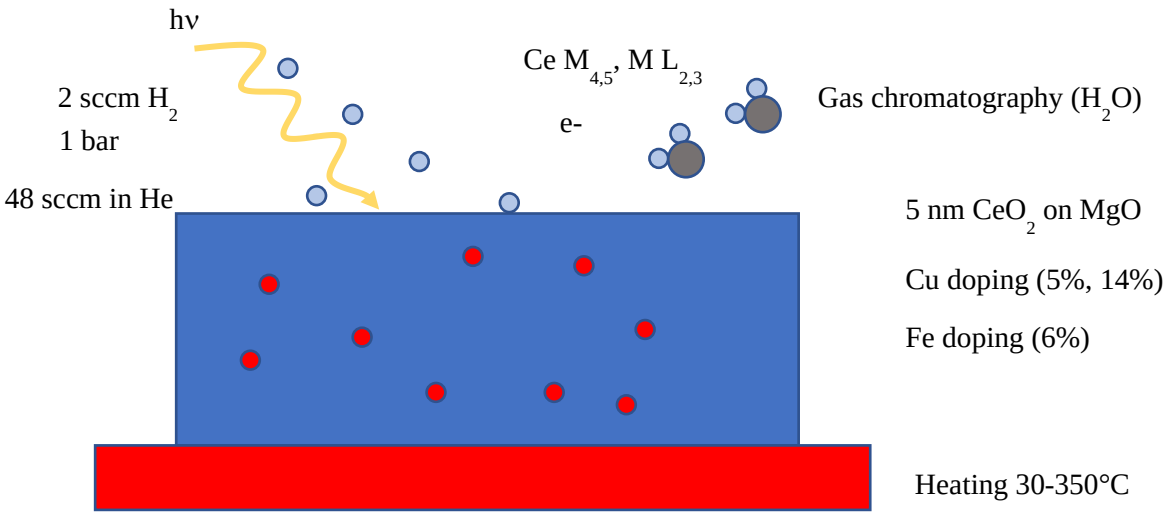

Figure 6: Sketch of the NEXAFS experiment performed at APE-HE.

6.2.1 Ce^{3+} ion concentration evolution

In this section, I will elucidate modifications in the XAS Ce M_5 spectrum and also provide a quantitative analysis of the evolution of Ce^{3+} ion concentration in the sample during thermal treatments in H_2 performed at ambient pressure. The reference spectra for CeO_2 and Ce_2O_3 shown in figure 7 were acquired from commercial CeO_2 powder from Umicore after oxidation in O_2 and reduction in H_2 at 670 K in the APE-HE reaction cell.

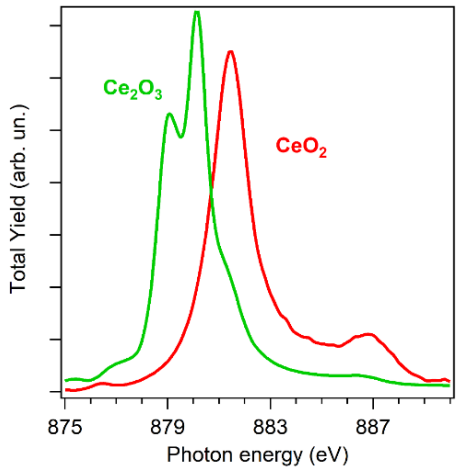

Figure 7: CeO_2 and Ce_2O_3 reference spectra taken from the oxidation and reduction of CeO_2 commercial powder.

Ce M_5 spectra in the undoped CeO_2, 5 % Cu: CeO_2 and 14% Cu: CeO_2 at different temperatures during the thermal treatments in H_2 are shown in figure 8. At room temperature all samples show a peak at around 881.4 eV, corresponding to the Ce M_5-edge, and a post edge peak at around 887 eV, resembling the XAS of typical CeO_2 NPs [4] and films [5,6]. The shape of the spectra results from multiplet splitting effects due to the interaction between the 3d core hole and 4f states. During the reduction cycles, two peaks start to appear at around 878 eV and 879 eV reflecting the increase in the Ce^{3+} ion concentration in the sample (see reference in figure 6). As the annealing temperature increases, these two peaks start to evolve and at 620 K they are higher for the Cu-doped films than undoped sample and are more intense for highly doped (14%) Cu:CeO_2.

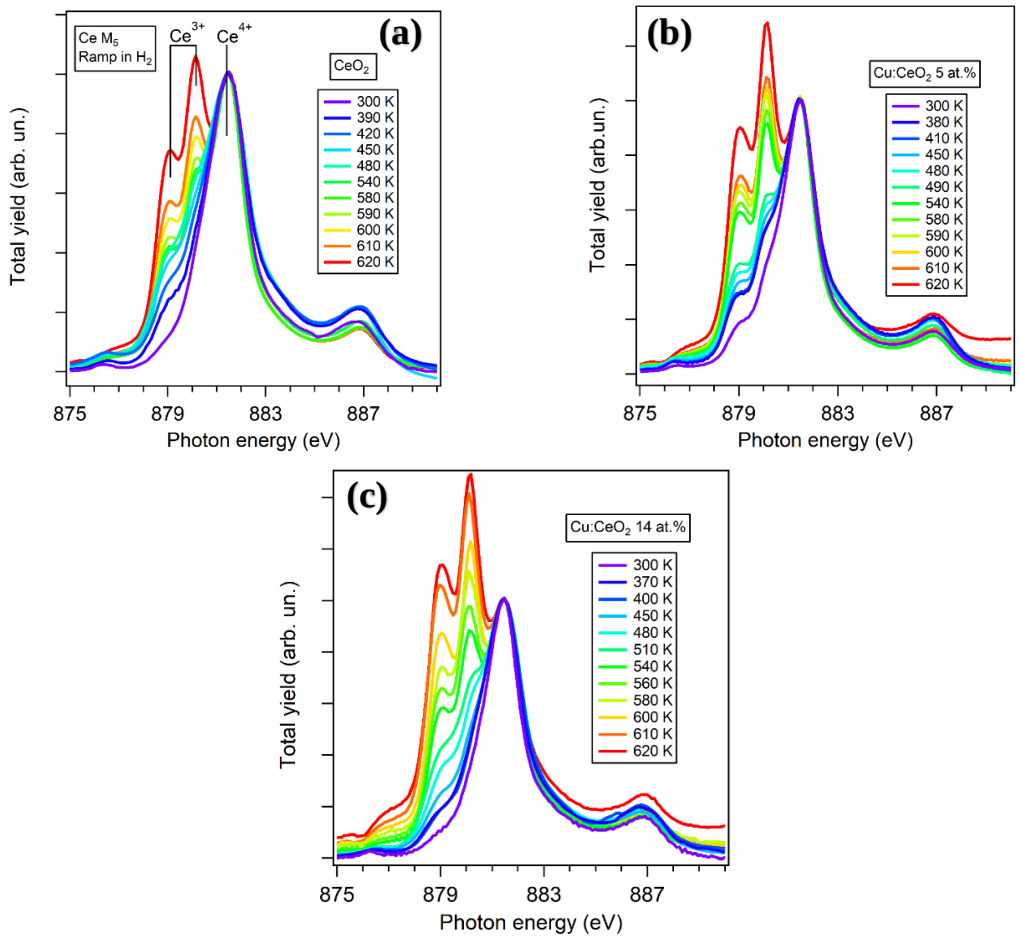

Figure 8: Evolution of Ce M_5 spectra during thermal treatments in H_2 for undoped (a), 5% Cu: CeO_2 (b) and 14% Cu:CeO_2 (c).

Ce M_5-edge has then been fitted to extract the information on the evolution of Ce^{4+} and Ce^{3+} ion concentration. As shown in figure 9, a pre-edge linear background was subtracted from the original spectrum for all the spectra before applying the fitting procedure to extract the information on the oxidation state of Ce ions. Function (6.1) was used to fit the Ce M_5-edge with a weighted function of NEXAFS spectra of the CeO_2 and Ce_2O_3 references to gain the information on the relative weight of the Ce^{3+}/ Ce^{4+}. Reference spectra were broadened to accommodate the fitting of our spectra.

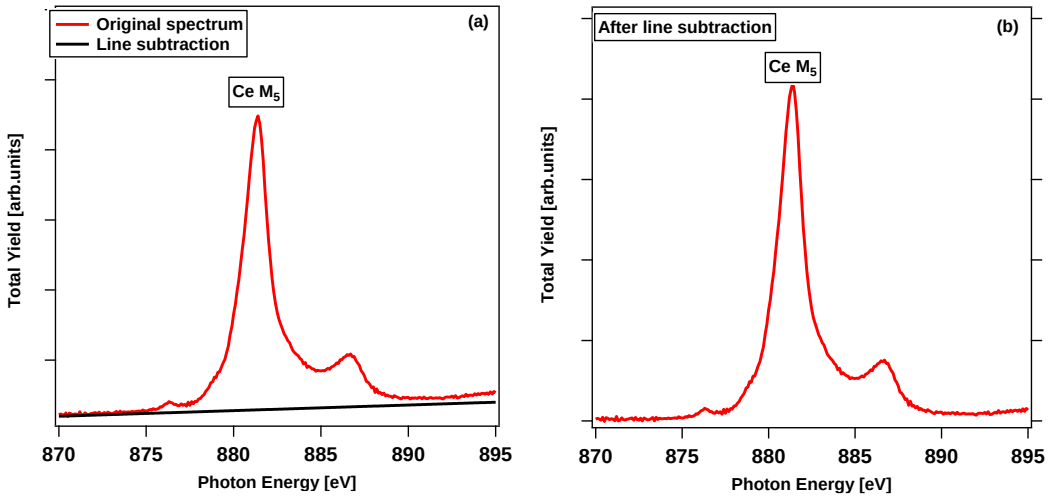

Figure 9: Background subtraction procedure from Ce M_5; (a) original spectrum with line background and (b) spectrum after background subtraction.

$$f(x) = A + B*CeO_2(x-x_0) + C*Ce_2O_3(x-x_0) + D*x \qquad (6.1)$$

A= pre-edge constant background

B= Ce^{4+} weight

C= Ce^{3+} weight

D= post edge background correction

x_0= correction factor for shift in the spectrum with respect to the references.

Figure 10 shows the fit of an oxidized and a partially reduced film with their relative fitting components.

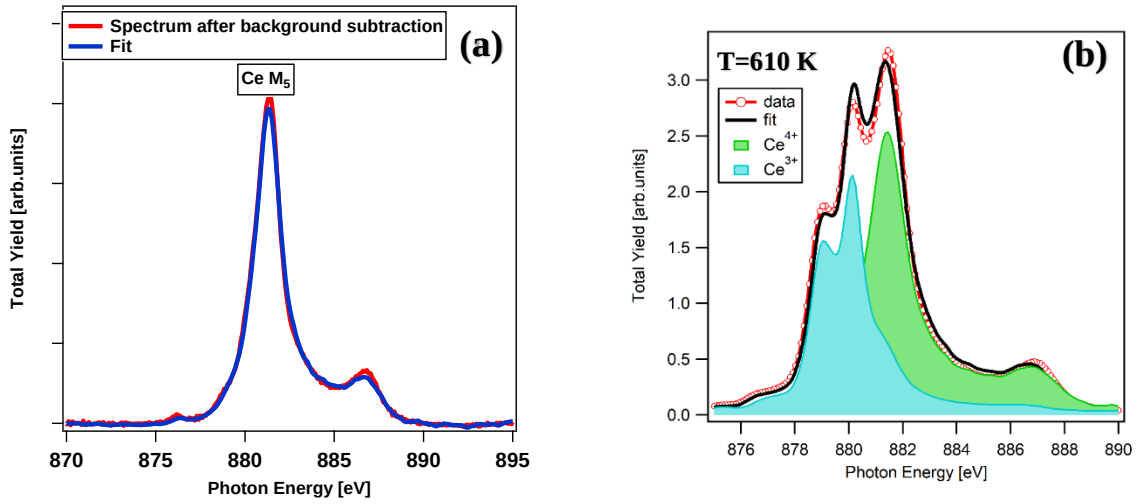

Figure 10: Ce M_5-edge spectrum and fit of an oxidized film (a) and a partially reduced (b) CeO_2.

The evolution of Ce^{3+} ions concentration was extracted by the ratio between the areas of the components as $Ce^{3+}/(Ce^{3+} + Ce^{4+})$ in the film. Figure 11 shows a comparison on the evolution of Ce^{3+} ions in the undoped CeO_2, 5% Cu: CeO_2 and 14% Cu: CeO_2 during the thermal treatment in H_2.

From figure 11, it is clear that the evolution of the reduced Ce ions for undoped CeO_2 and Cu:CeO_2 films follow a similar trend until around 500 K. Afterwards, Ce^{3+} ion concentration in the 14% doped Cu:CeO_2 film increased rapidly compared to the other two films and reaches up to 68% at 620 K. The Ce^{3+} concentration in the 5% Cu: CeO_2 film reaches 64% at 620 K even if at 300 K it is slightly higher than for the undoped and 14% doped films. The observed higher concentration of Ce^{3+} ions in the 14% doped CeO_2 can be ascribed to the presence of a higher concentration of active sites for H_2 dissociation. Additionally, we may also speculate that the higher concentration of Cu dopant atoms (14%) might have introduced some structural distortions which have an influence on the oxygen vacancy formation and thus on the reduction.

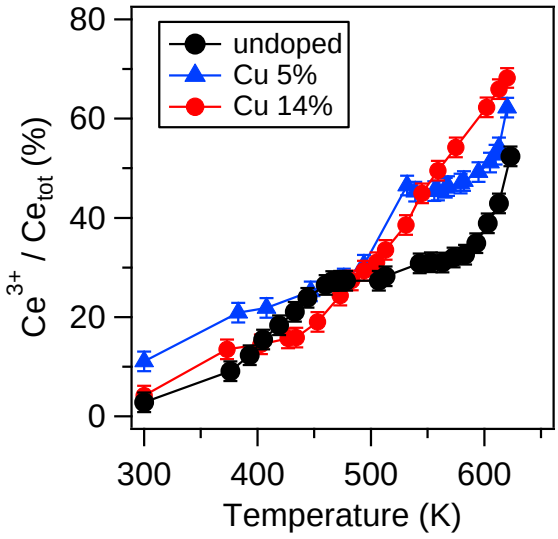

Figure 11: Comparison on the evolution of the Ce^{3+} ions concentration during thermal treatments in H_2.

The undoped CeO_2 film shows a slower increase of Ce^{3+} concentration above 500 K when compared to the Cu-doped films and reaches about 42% at 620 K. The final Ce^{3+} concentrations in the films disclose the fact that the Cu:CeO_2 films are more reactive and thus are more reduced than the undoped CeO_2.

For the undoped and 14% Cu:CeO_2 films a comparison of the Ce^{3+} concentration during He and H_2 temperature cycles is shown in figure 12.

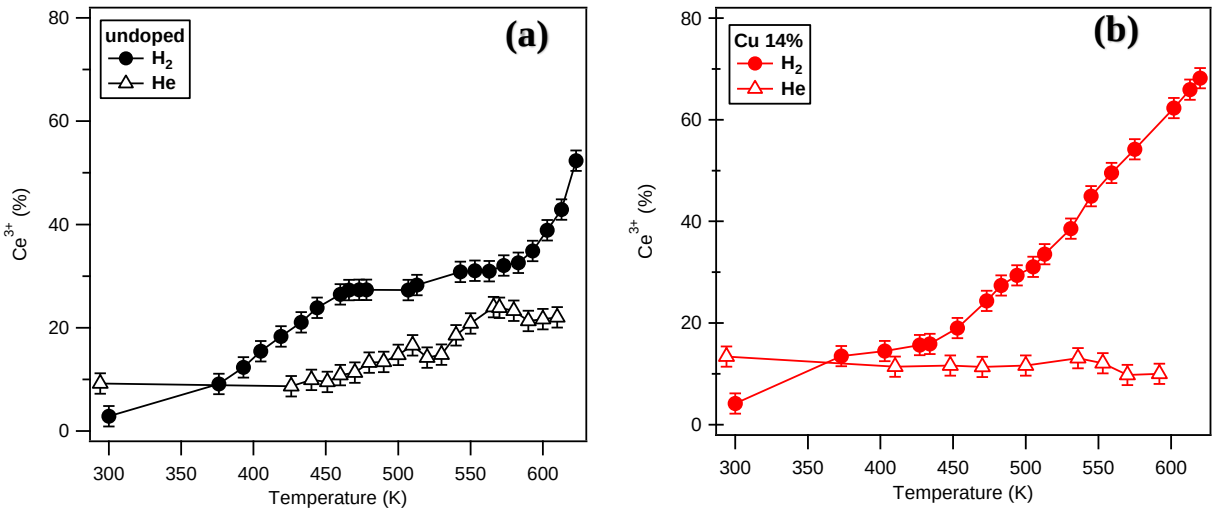

Figure 12: A comparison between evolution of Ce^{3+} concentration during temperature ramp in He and H_2 for undoped CeO_2 (a) and 14% Cu:CeO_2 (b).

From figure 12 (a), it is evident that the evolution of Ce^{3+} concentration in the undoped CeO_2 film is quite slower in He compared to H_2 treatments and the reduction of the 14% Cu:CeO_2 film is negligible in He as

compared to H_2 as shown in the figure 12 (b). So, we can clearly say that the observed reduction of Ce in the thermal treatments in H_2 are not impacted significantly by the presence of inert gas in the reaction cell or is not the effect of temperature only.

6.2.2 Evolution of Cu oxidation states

XAS of Cu $L_{2,3}$ spectra were also acquired during the temperature treatments in H_2 to find a correlation between the evolution of Ce and Cu oxidation states during thermal treatments. The XAS spectra of normalized Cu L_3-edge for 5% and 14% Cu: CeO_2 are shown in figure 14.

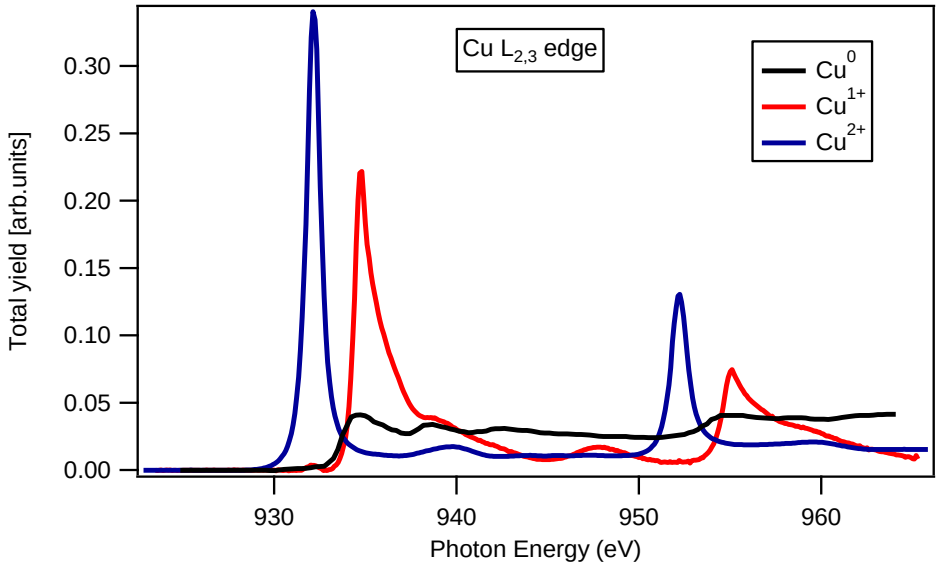

Figure 13: Cu $L_{2,3}$ edge measured from Cu oxide powders at APE-HE.

As can be seen in figure 14(a), a combination of two peaks is present in the Cu L_3-edge at around 936 eV and 932 eV respectively for 5% Cu:CeO_2 film at lower temperatures, corresponding to Cu^{1+} and Cu^{2+} in reference spectra (figure 13). The peak corresponding to Cu^{2+} ions is more intense than Cu^{1+} peak at lower temperatures. As the annealing temperature is raised, the Cu^{2+} peak starts to decrease in intensity and a slight increase in Cu^{1+} component increases. When the temperature reaches the maximum (620 K), the Cu atoms are mostly reduced to Cu^{1+} state with only a small fraction of Cu^{2+} ions left in the film. Additionally, a new component appears at low photon energy, about 1 eV below the Cu^{2+} component (A). This new component could be ascribed to a change in the coordination of a small fraction of Cu^{2+} ions, changing from an ionic to a more covalent environment [6]. This could be ascribed to the migration of a small fraction of Cu atoms forming small CuO_x clusters at particular sites inside the matrix. In contrast, as shown in figure 14 (b), the 14% Cu:CeO_2 film spectrum consists of a sharp peak corresponding to Cu^{2+} at lower temperatures with only a tiny Cu^{1+} peak. The evolution of Cu^{1+} while increasing the temperature is visible.

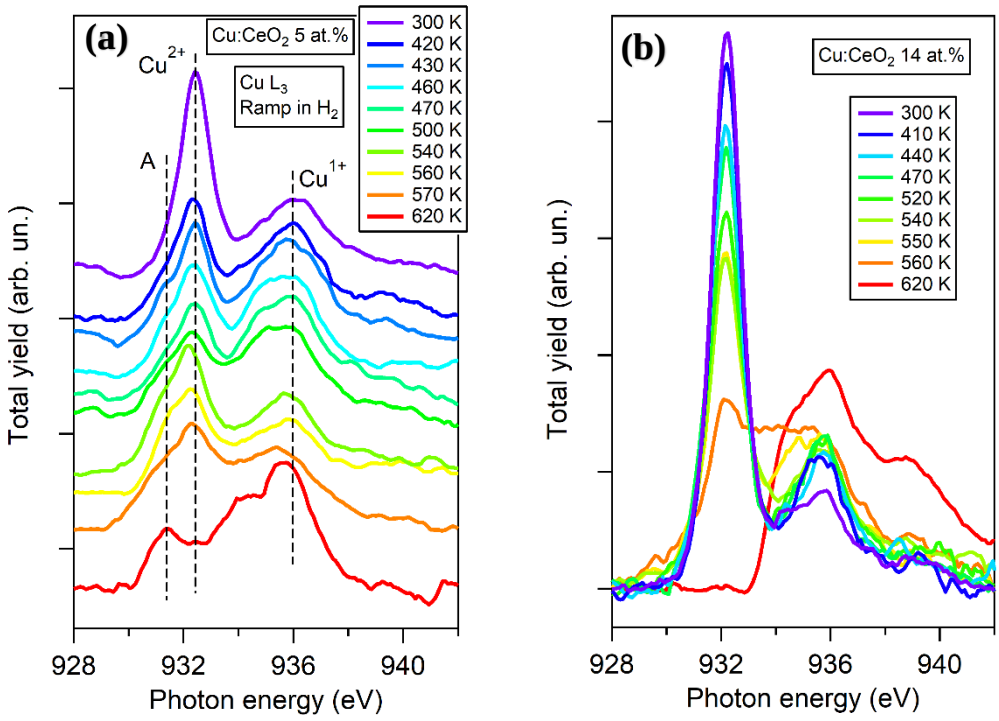

Figure 14: XAS of Cu L₃-edge showing the evolution of Cu oxidation (1+, 2+) states during thermal treatments in H_2 for 5% Cu: CeO_2 (a) and 14% Cu: CeO_2 (b).

For temperature increasing up to 550 K, the Cu^{2+} peak decreases and the contribution of Cu^{1+} increases. In this case the A component is not visible, probably because at such low temperatures the small fraction of Cu atoms migrating and clustering is negligible compared to the total amount of Cu. Increasing further, a metal component appears at about 934 eV, characterized by the post edge oscillations typical of the metal edge (ref figure 13). However, due to the proximity in the binding energies of Cu metal and Cu^{1+} states, it is difficult to properly deconvolve the two components. The increase in the Cu metal component in 14% Cu:CeO_2 can be attributed a strong migration of Cu atoms from the surface layers into the bulk/interface. Probably the Cu atoms migrated at the interface are in metallic state compared to Cu atoms in the oxide that remain oxidized. The effect of temperature treatments on migration of Cu atoms was also observed in the case of Cu:CeO_2/Pt samples in UHV conditions, while for Cu:CeO2/MgO this is evident only in ambient pressure conditions. Probably the increased H_2 pressure induces a stronger reducibility and therefore a higher mobility in the oxide as compared to UHV conditions.

Cu L_3 XAS spectra was fitted with 3 gaussian peaks corresponding to Cu^{1+}, Cu^{2+} and A component respectively. A spline background was subtracted from the spectra before the fitting. The fitting procedure was aimed at finding the evolution of the three species during the temperature treatments in H_2, while a

quantitative conclusion is more delicate due to different cross sections for atoms in different oxidation states. An example of the fitting is shown in the figure 15.

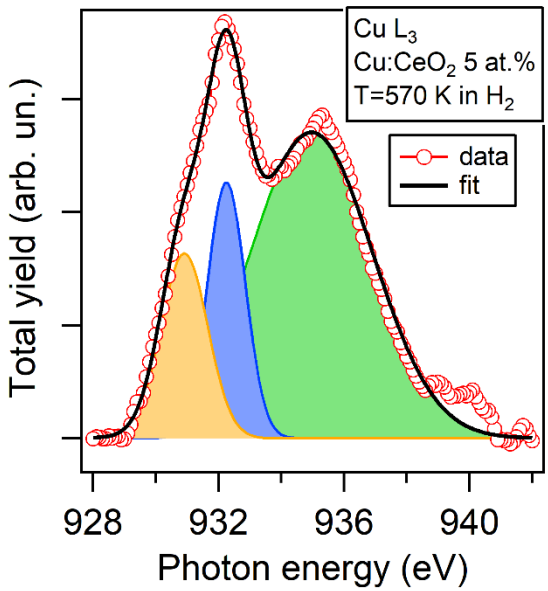

Figure 15: XAS Cu L_3-edge of the 5% Cu:CeO_2 film in H_2 at 570 K and its fitting components. The three gaussian peaks correspond to A (yellow), Cu^{2+} (blue) and Cu^{1+} (green) components.

The evolution of Cu species in 5% Cu:CeO_2 and 14% Cu:CeO_2 films during the thermal treatments in H_2, obtained from the fit, is presented in figure 16. As seen in the Cu L_3 XAS spectra, the relative weight of Cu^{1+} and Cu^{2+} areas are nearly equal at the lower temperatures in 5% Cu:CeO_2 film. As the temperature is increased, the Cu^{1+} relative weight increases while the Cu^{2+} weight decreases gradually as shown in figure 16 (a). Whereas the 14% Cu:CeO_2 (figure16(b)) shows a higher Cu^{2+} area at the lower temperatures and the relative weight of Cu^{2+} starts to decline with an increase in the Cu^{1+} relative weight.

After the H_2 thermal treatment a re-oxidation process in O_2(10 sccm)/He(40 sccm) at 620 K was performed for all the samples. The XAS spectra of the Ce M_5-edge for 14% Cu:CeO_2 (a) and the Cu L_3 for 5% (b) and 14% (c) doped Cu:CeO_2 films are shown in figure 17. After annealing in O_2, the Ce ions in all films were re-oxidized completely to 4+ state as shown in Figure 17a. Also, we observed that Cu atoms are fully reversible to the initial oxidation state in 6% Cu:CeO_2 as shown in the figure 17 (b). While the XAS Cu L_3 measured showed incomplete reoxidation of the Cu atoms in 14% doped Cu:CeO_2 film. This behavior can be attributed to the resistance of the migrated metallic Cu atoms to the interface to re-oxidation.

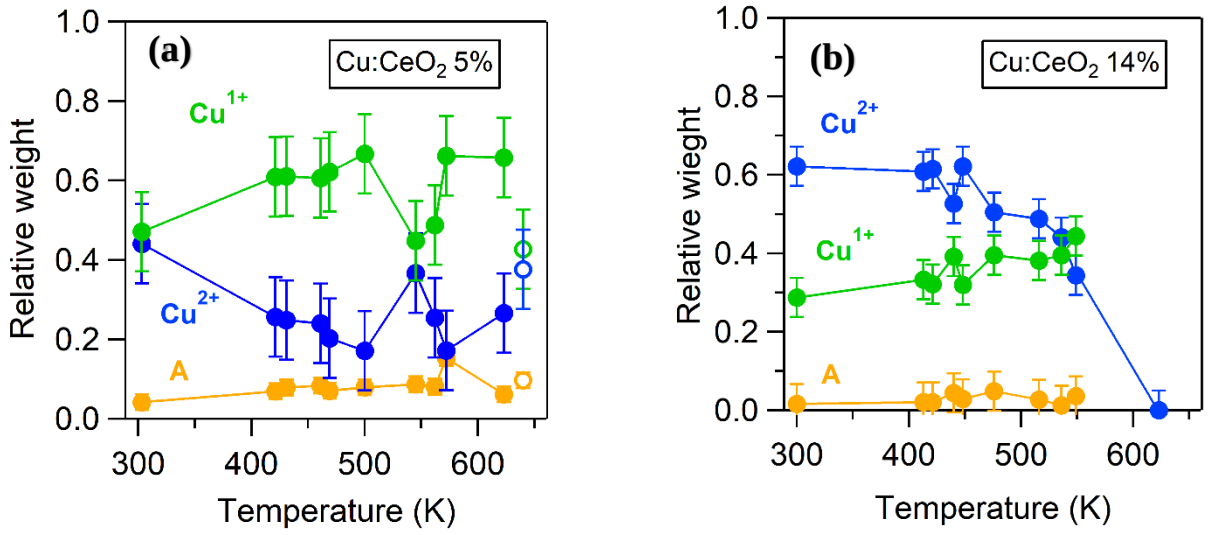

Figure 16: The evolution of the relative weight of Cu^{1+}, Cu^{2+} and A components during temperature treatments in H_2 in (a) 5% $Cu:CeO_2$ and (b) 14% $Cu:CeO_2$.

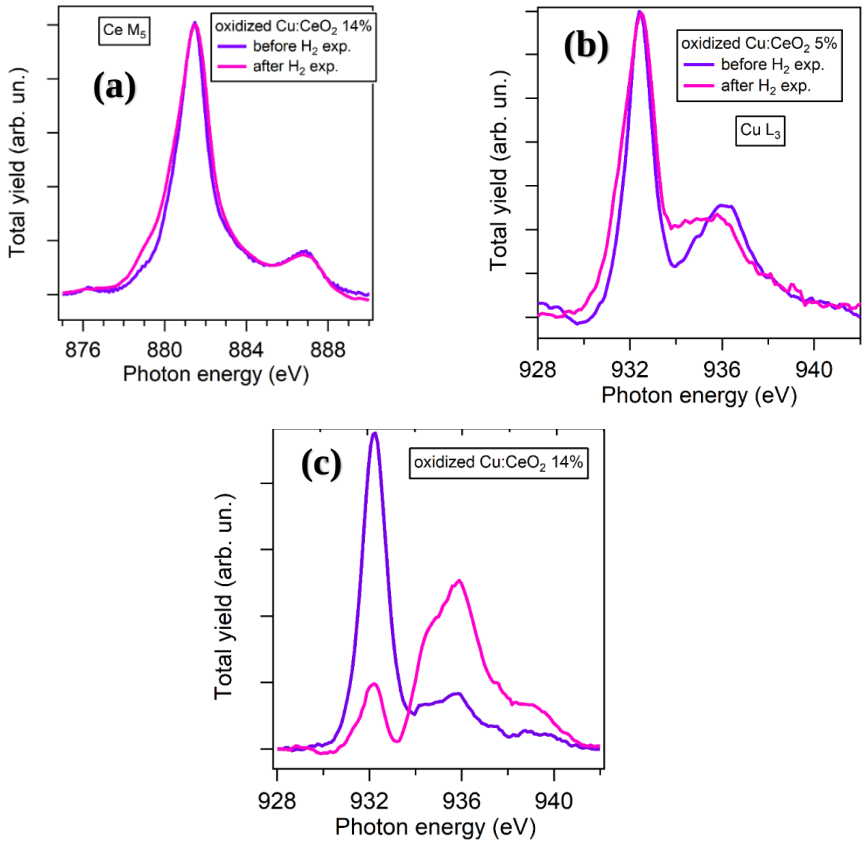

Figure 17: XAS spectra of (a) Ce M_5 in 14% $Cu:CeO_2$, (b) Cu L_3 in 5% $Cu:CeO_2$ and (c) Cu L_3 in 14% $Cu:CeO_2$ acquired after re-oxidation of the samples after H_2 ramp.

6.2.3 Ambient pressure NEXAFS of 6% Fe:CeO_2

We have investigated for comparison a CeO_2 film modified with 6% of Fe atoms in analogy with the Cu:CeO_2 films. We measured XAS of the Ce M_5 and Fe L_3 -edges to understand the effect of dopant on the Ce reduction as well as the evolution of Fe ions during thermal treatments in H_2. Ce M_5 edge and Fe L_3 XAS are shown in the figure 18.

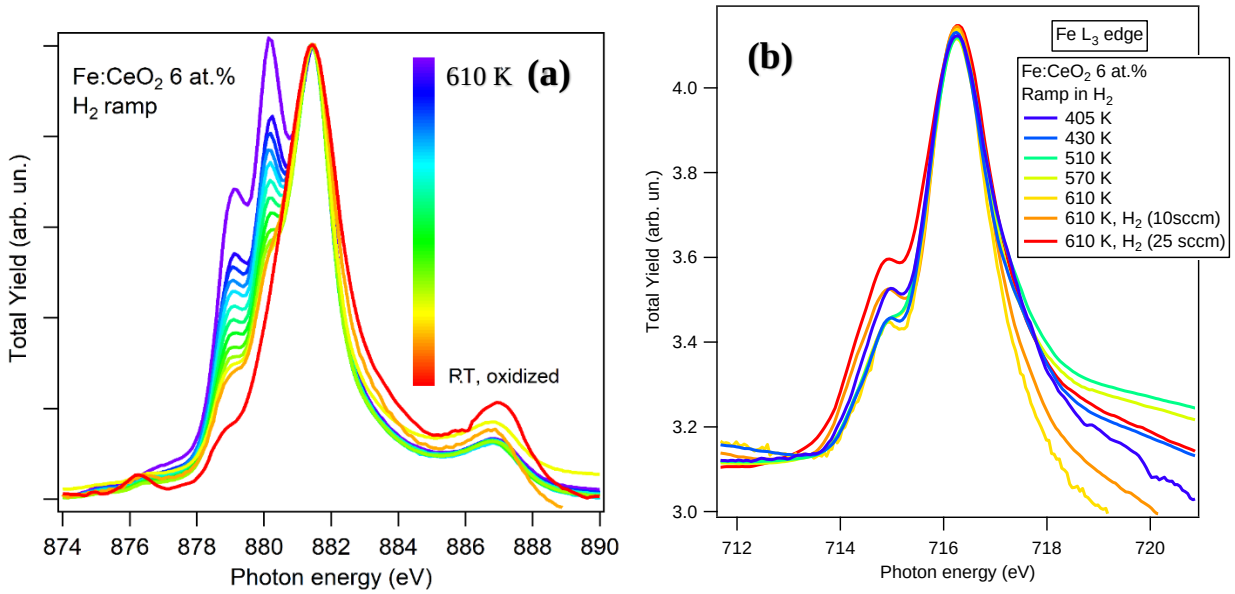

Figure 18: X-ray absorption spectra of Ce M_5 (a) and Fe L_3-edges (b) acquired during the thermal treatments in H_2 for Fe:CeO_2.

The Ce M_5-edge spectra shown in figure 18 (a) indicate the evolution of the Ce^{3+} ions during thermal treatments in H_2. The peaks corresponding to the Ce^{3+} component starts to evolve gradually with the increase in temperature. In figure 18 (b), the XAS spectra of Fe L_3-edge are shown during the temperature treatments in H_2. The temperature treatments in H_2 did not modify the Fe L_3 spectra. So, Fe prefers to be in a stable oxidation state (Fe^{3+}) in these conditions [7], which makes it less reactive compared to Cu^{1+}. Evolution of Ce^{3+} concentration during thermal treatments in H_2 are compared in figure 19 for undoped CeO_2, 5% Cu:CeO_2 and 6% Fe:CeO_2. The evolution of the Ce^{3+} ions in the Fe-doped CeO_2 follows a similar trend of the undoped CeO_2. In contrast to the Cu:CeO_2 films, Fe:CeO_2 film shows a lower Ce^{3+} increase as the Fe atoms are inactive. At higher temperatures, Fe:CeO_2 film reduces but only reaches up to around 48% of Ce^{3+}, which is comparable to the undoped film.

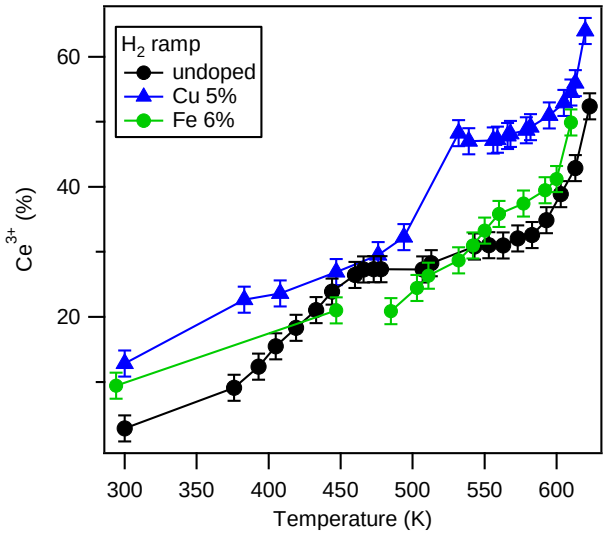

Figure 19: A comparison on the evolution of Ce^{3+} concentration during H_2 ramps for undoped, 5% Cu-doped and 6% Fe-doped CeO_2.

6.3 Gas chromatography

Gas chromatography (GC) measurements were also acquired in parallel to XAS measurements during thermal treatments to understand the formation of water (H_2O) on the surface of the films. The quantitative results obtained from the analysis of GC spectra for all the samples are shown in figure 20. The figure reports the area of the peak assigned to water as a function of the annealing temperature.

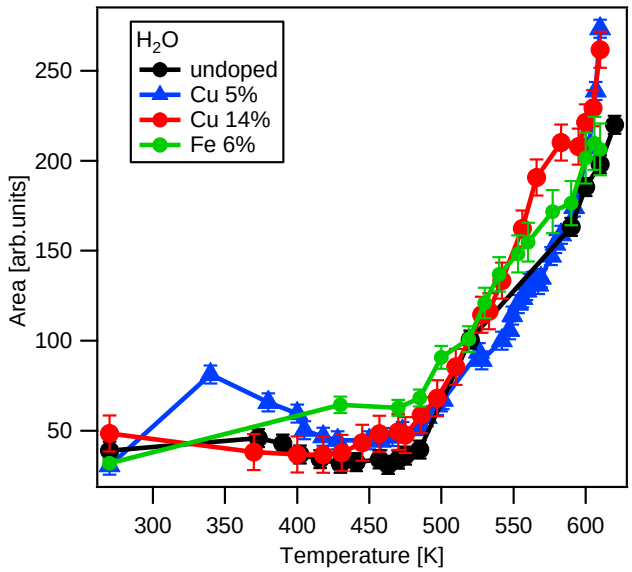

Figure 20: Area of water peak from gas chromatography spectra acquired during the thermal treatments in H_2.

All the films showed a similar behavior as can be seen in figure 20. An initial production of water is present already at low temperature, due to a degas from the system, together with some amount of carbon-containing molecules. As the temperature was increased, a rise in the water peak starting around 470 K was observed. But increasing further the temperature, the Cu:CeO_2 (both 5 and 14%) films showed higher water formation compared to the undoped and Fe-doped CeO_2. This behavior is related to the corresponding higher H_2 dissociation on the Cu-doped samples and subsequent higher oxide reduction, Ce^{3+} formation and increase of reactive Cu^{1+} species.

The whole cell including internal structure and the sample holder are made up of Ti, exposing a Ti oxide surface to the gas environment. It is reported that no reduction of TiO_2 was observed during temperature programmed reduction treatments in H_2 from 50 until 750°C [8]. So, the contribution of the reaction cell chamber and the sample holder on the evolution of water during thermal treatments in H_2 are discarded.

We have also performed the GC measurements of the undoped CeO_2 film in He to verify the amount of water formation due to degassing of the entire system. A comparison between H_2 and He ramps for pure CeO_2 is shown in figure 21. The amount of water formation on the surface of the CeO_2 film is constant at about 50 in He even at higher temperatures, which confirms that the degassing is negligible and that the observed evolution of the water formation on the surface during the thermal treatments in H_2 is related to dissociation on the film. For these reasons, the GC here reported is sensitive to few ppm of water produced, therefore compatible with reaction products from a 5 nm film.

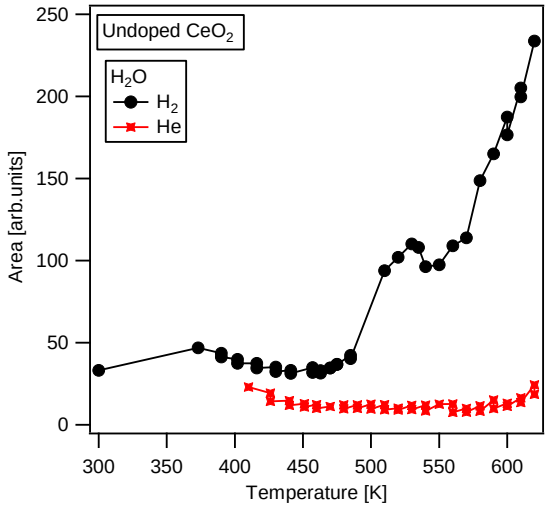

Figure 21: A comparison between area of water peak from gas chromatography spectra acquired during the thermal treatments in He and H_2 for undoped CeO_2.

6.4 Bibliography:

1. Skála, T., Šutara, F., Prince, K. C., & Matolín, V. (2009). Cerium oxide stoichiometry alteration via Sn deposition: Influence of temperature. *Journal of Electron Spectroscopy and Related Phenomena*, *169*(1), 20-25.
2. Benedetti, S., Righi, G., Luches, P., D'Addato, S., Magri, R., & Selloni, A. (2020). Surface reactivity of Ag-modified ceria to hydrogen: a combined experimental and theoretical investigation. *ACS Applied Materials & interfaces*, *12*(24), 27682-27690.
3. Vikatakavi, A., Benedetti, S., Righi, G., Magri, R., D'Addato, S., Luches, P., & Selloni, A. (2022). Interaction of Hydrogen with Cu-Modified Cerium Oxide Surfaces. *The Journal of Physical Chemistry C*.
4. Sharma, A., Varshney, M., Shin, H. J., Park, Y. J., Kim, M. G., Ha, T. K., ... & Gautam, S. (2014). Electronic structure study of Ce 1− x A x O 2 (A= Zr & Hf) nanoparticles: NEXAFS and EXAFS investigations. *Physical Chemistry Chemical Physics*, *16*(37), 19909-19916.
5. Shi, Y., Wang, L., Wang, Z., Vinai, G., Braglia, L., Torelli, P., ... & Yang, N. (2020). Defect engineering for tuning the photoresponse of ceria-based solid oxide photoelectrochemical cells. *ACS Applied Materials & Interfaces*, *13*(1), 541-551.
6. Mitra, C., Hu, Z., Raychaudhuri, P., Wirth, S., Csiszar, S. I., Hsieh, H. H., ... & Tjeng, L. H. (2003). Direct observation of electron doping in La 0.7 Ce 0.3 MnO 3 using x-ray absorption spectroscopy. *Physical Review B*, *67*(9), 092404.
7. Regan, T.J., Ohldag, H., Stamm, C., Nolting, F., Lünning, J., Stöhr, J., White, R.L. (2001). Chemical effects at metal oxide interfaces studied by x-ray-absorption spectroscopy. *Physical Review B* 64, 214422.
8. Watanabe, S., Ma, X., & Song, C. (2009). Characterization of structural and surface properties of nanocrystalline TiO2− CeO2 mixed oxides by XRD, XPS, TPR, and TPD. *The Journal of Physical Chemistry C*, *113*(32), 14249-14257.

Conclusions

An extensive investigation on the interaction between copper modified CeO_2 ultrathin epitaxial films and H_2 is documented in this thesis. The redox properties of cerium atoms and oxygen vacancy formation in the presence of Cu atoms as dopants in various concentration during temperature treatments in both UHV and in H_2 have been studied. In particular, emphasis is given to the study the effect of Cu in CeO_2 on the H_2 dissociation process under thermal reduction cycles. Our main goal was to also find a correlation between the evolution of Ce^{3+}, oxygen vacancy formation, Cu chemical state and the H_2 dissociation process on the surface of the Cu-modified films. We have also investigated the effect of Cu NPs supported on CeO_2 (111) towards the H_2 dissociation process.

Cu-modified CeO_2 ultrathin films were grown epitaxially on Pt (111) substrates in well-controlled O_2 partial pressure (1×10^{-7} mbar), using reactive MBE. The chemical properties have been thoroughly investigated using in-situ X-ray photoelectron spectroscopy (XPS) and surface morphology of the films were studied using scanning tunneling microscopy (STM) at RT. XPS results showed a higher Ce^{3+} concentration on the surface during thermal treatments in H_2 compared to Ag: CeO_2(111) and pristine CeO_2/Pt. A higher activity towards H_2 dissociation under the influence of the Cu atoms was confirmed by the increased hydroxyl groups concentration on the oxide surface, as the Cu atoms are found to reduce the activation barrier for H_2 dissociation. Density functional theory (DFT) calculations, performed by a group of collaborators, allowed to obtain deeper insights into the experimental results acquired on the reactivity of the Cu-modified CeO_2 surfaces. The model indicated the effect of highly reactive Cu atoms in +1 oxidation state on the promotion of dissociative adsorption of H_2 on the surface of the Cu-modified films. The presence of Cu dopant ions decreases the energy barrier from +0.99 eV (pristine CeO_2) to +0.8 eV. Cu^{1+} species, produced due to the removal of oxygen bonded to Cu, are found to be more active and to further significantly decrease the activation energy barrier to 0.33 eV. The surface morphology of the Cu: CeO_2 films was investigated by STM at RT. STM images taken before the thermal treatments revealed a rough surface topography with different contrast levels. After the treatments in H_2, the STM measurements were instable possibly due to the presence of OH groups on the surface. However, further re-oxidation treatments allowed to demonstrate that the surface morphology was not significantly affected by the cycles.

In the case of films with relatively high dopant concentration, some migration of copper from the surface to the interface is evidenced by the variation of the XPS Cu 2p intensity at different emission angles. The limited residual copper concentration on the surface is active towards the hydrogen dissociation process. When a buffer of pure ceria is introduced between the doped CeO_2 and the Pt support, the Cu atoms are more stable and the reactivity to H_2 slightly increases.

Cu NPs/ CeO_2 films were also highly reactive towards H_2 dissociation. XPS and STM measurements acquired after reducing treatment revealed the dilution of nanoparticles from the surface into the bulk of the oxide support. In H_2 environment the NPs start to partially be incorporated into the support at higher temperatures as compared to the NPs thermally treated in vacuum.

Furthermore, I focused on understanding the evolution of cerium ions (Ce^{4+}/Ce^{3+}) and the activation of hydrogen dissociation on Cu: CeO_2 ultrathin films grown on MgO as an inert substrate. Surprisingly, Cu:CeO_2/ MgO (100) films showed a different behavior compared to Cu:CeO_2/Pt (111). Cu:CeO_2/ MgO exhibited negligible activity towards the of dissociation H_2 at pressures compatible with UHV conditions, possibly because of the nature of the bond at the Cu:CeO_2 oxide film and MgO interface. Probably the mobility of the Ce and O cations on the surface are hindered by the strong bonds at the interface, thus affecting the properties of the film.

Near edge x-absorption spectroscopy (NEXAFS) in the soft X-ray regime was performed on 5 nm thick Cu: CeO_2 films with different dopant concentrations at ambient pressure of H_2. Ce $M_{4,5}$-edge spectra acquired during the thermal treatments in H_2, reflected the surge in Ce^{3+} concentration in the Cu-doped films. Higher dopant concentrations induced a higher Ce^{3+} concentration. Cu $L_{2,3}$-edge spectra taken during the thermal treatments revealed the presence and evolution of Cu^{1+} from the more abundant Cu^{2+} species with increase in the annealing temperature, as predicted by DFT. In ambient pressure conditions at high Cu concentration a temperature of 620 K is sufficient to induce Cu migration and metal cluster formation on Cu:CeO_2/MgO, inert at UHV conditions. We also studied CeO_2 modified with 6% Fe atoms. In contrast with the case of Cu, Fe atoms were found to give no additional contribution in H_2 activation and in the subsequent Ce reduction with respect to pure CeO_2. No significant modifications in Fe L_3-edge spectra were found, and the properties of the films remained similar to those of undoped CeO_2 films. Reaction products were also detected simultaneously by gas chromatography, confirming the formation of water in close correspondence to the behavior of Ce and Cu reduction with temperature.

Since the Cu-modified films at low concentrations exhibited a better catalytic activity compared to pristine and Ag: CeO_2 ultrathin films, this study on a model system can serve as a support in designing a suitable catalyst with high activity and selectivity for the hydrogen oxidation reaction (HOR) process in PEMFCs.

Appendix A

Conferences, Seminars and Workshops:

1. **Title: "*A study on the surface reactivity of modified CeO2 ultra-thin films towards H2 dissociation*"**
   Nano colloquia2021, S3 seminar, 2nd December 2021, by **Avinash Vikatakavi (oral presentation)**

2. **Title: "Surface reactivity of Cu-modified CeO_2 towards H_2 dissociation"**
   E-MRS fall meeting, 20-23rd September 2021 (online), by **Avinash Vikatakavi (oral presentation).**

3. **Title: "Interaction between hydrogen and doped cerium oxide surfaces"**
   IWOX-XIII International Workshop on Oxide Surfaces, Phoenix Pyeongchang, Republic of Korea 9-14th January 2022, by Dr. Paola Luches **(Co-author)**

4. **Title: "Surface reactivity to hydrogen of Ag-and Cu-modified CeO2"**
   Virtual DPG Spring Meeting "SurfaceScience21", 1-4th March 2021, by Dr. Stefania Benedetti **(contribution to poster presentation)**.

5. **Title: "Studies of charge transfer processes in functional oxides"**
   Italy@EuXFEL workshop, 10-11th December 2020 (Online), by Paola Luches **(Co-author)**

6. **Title: "Dynamics of photo-induced charge excitations in functional oxides"**
   European XFEL seminar, 18th May 2021, by Paola Luches(online), **(Participation)**

7. **Title: "Coherent Manipulation and Readout of Molecular Spins through Microwave Planar Superconducting Resonators"**
   Nano colloquia 2021, S3 seminar, by Claudio Bonizzoni, online **(Participation)**

8. **Title: "Tunable Frictional Response of Induced Strained Graphene"**
   Nano colloquia 2021, S3 seminar**,** by Andrea Mescola, online, **(Participation)**

9. **Title: "Synthesis of nanoparticles: applications and new perspectives"**
   CMD2020GEFES (Online conference) from 1&2nd September, **(Participation)**

10. **"Surfaces were invented by the devil"**

    Modena (Italy) from 16-17th Nov 2020, **(Participation)**

11. **"Fuel cell Day"**

    Modena (Italy) on 12th December 2019, **(Participation)**

Experience in other laboratories

1. NFFA Trieste (08/03/2022-13/03/2022)

Proposal Title: *"In operando NEXAFS study of the correlation between dopant oxidation state and structure in Cu- and Fe- modified CeO_2 during H_2 dissociation"*

I performed In-operando NEXAFS at APE-HE beamline on CeO_2, Cu:CeO_2, Fe:CeO_2 films grown on MgO (001) in soft X-ray regime at ambient pressure in a reaction cell. TEY mode was employed to detect XAS by probing the drain current from membrane. Main goal was to investigate the possible changes in the dopant oxidation state (Cu and Fe) as well as Ce during thermal treatments in H_2 at ambient pressure and to correlate the electronic modifications of the films through the measurement of the Ce M_{45}, Cu and Fe $L_{2,3}$ absorption edges to the reaction products in the gas.

Appendix B

Publications

1. **Title: "Interaction of Hydrogen with Cu-Modified Cerium Oxide Surfaces"**

Avinash Vikatakavi, Stefania Benedetti, Giulia Righi, Rita Magri, Sergio D'Addato, Paola Luches, and Annabella Selloni *The Journal of Physical Chemistry C* **2022** *126* (44), 18652-18660

Abstract: We investigate the interaction between molecular hydrogen and ultrathin epitaxial CeO_2 films modified with a 2% concentration of Cu atoms using X-ray photoemission spectroscopy (XPS) during thermal reduction cycles in H_2. The XPS measurements are combined with density functional theory calculations to obtain further insight into the observed modifications of the film surface. Our results show that the presence of Cu atoms decreases the barrier for H_2 dissociation in comparison to that on pure ceria surfaces, leading to the formation of surface OH groups after exposure to H_2. Moreover, surface oxygen vacancies are generated already at mild temperatures (470 K), most likely via water formation and desorption. The presence of surface oxygen vacancies and hydroxyls contributes to the observed large increase in surface Ce^{3+} concentration with increasing reduction temperature. In spite of these atomic scale modifications, the surface morphology observed by scanning tunneling microscopy remains substantially unchanged on the length scale of tens of nm.

Role: Designed and carried out the experiments in SESAMo laboratory to prepare Cu-modified CeO_2 films on Pt (111) using a reactive MBE source. XPS, STM tools were used for characterization purpose. Analyzed the XPS, STM data and wrote the manuscript.

2. **Title: "Ultrafast Dynamics of Plasmon-Mediated Charge Transfer in Ag@CeO_2 Studied by Free Electron Laser Time-Resolved X-ray Absorption Spectroscopy"**

Jacopo Stefano Pelli Cresi, Emiliano Principi, Eleonora Spurio, Daniele Catone, Patrick O'Keeffe, Stefano Turchini, Stefania Benedetti, **Avinash Vikatakavi**, Sergio D'Addato, Riccardo Mincigrucci, Laura Foglia, Gabor Kurdi, Ivaylo P. Nikolov, Giovanni De Ninno, Claudio Masciovecchio, Stefano Nannarone, Jagadesh Kopula Kesavan, Federico Boscherini, and Paola Luches *Nano Letters* **2021** *21* (4), 1729-1734

Abstract: Expanding the activity of wide bandgap semiconductors from the UV into the visible range has become a central goal for their application in green solar photocatalysis. The hybrid plasmonic/semiconductor system, based on silver nanoparticles (Ag NPs) embedded in a film of CeO_2, is an example of a functional material developed with this aim. In this work, we take advantage of the chemical sensitivity of free electron laser (FEL) time-resolved soft X-ray absorption spectroscopy (TRXAS) to investigate the electron transfer process from the Ag NPs to the CeO_2 film generated by the NPs plasmonic resonance photoexcitation. Ultrafast changes (<200 fs) of the Ce $N_{4,5}$ absorption edge allowed us to conclude that the excited Ag NPs transfer electrons to the Ce atoms of the CeO_2 film through a highly efficient electron-based mechanism. These results demonstrate the potential of FEL-based TRXAS measurements for the characterization of energy transfer in novel hybrid plasmonic/semiconductor materials.

Role: Prepared Ag NPs/CeO_2 samples on ultrathin parylene-N self-standing foils using DC-Magnetron cluster source. XPS was used to investigate the surface composition. Supported in assembling the manuscript.

Future publications:

3. **Title: "Interaction of Cu dopant and Cu nanoparticles with cerium oxide in hydrogen environment"**
   Avinash Vikatakavi, Stefania Benedetti, Paola Luches, (in preparation).

4. **Title: "Role of Cu dopant in hydrogen dissociation on Cu:CeO_2 surfaces studied by near ambient pressure X-ray absorption spectroscopy"**
   Avinash Vikatakavi, Silvia Mauri, Samuele Pelatti, Mario Rivera, Sergio D'Addato, Paola Luches, Piero Torelli, Stefania Benedetti, (in preparation)

Courses attended

1. "Physics of the single electron in the transmission electron microscope" Prof. Giulio Pozzi,

   Ernst Ruska-Centre for Microscopy and Spectroscopy with Electrons, Forschungszentrum Juelich, Germany.

2. "Ultrafast spectroscopies applied to functional materials" Dr. Paola Luches
   CNR-Nano-S3, Modena.

3. "Synchrotron Radiation: Basics and Applications" Prof. Sergio D'Addato

   University of Modena and Reggio Emilia.

4. "Course on Fuel Cells" Prof. Marcello Romagnoli

   University of Modena and Reggio Emila

5. "Fundamentals of Spintronics" Prof. Marco Affronte
   University of Modena and Reggio Emilia.
6. "Elements of Quantum Technologies" Prof. Marco Affronte
   University of Modena and Reggio Emilia.
7. "Scientific communication in English" Mr. Adrian Wallwork
   English for Academics (e4ac), Pisa.
8. "Chromatography Made Easy by Chemometrics" Prof. Rasmus Bro
   University of Copenhagen